UAB

Universitat Autònoma de Barcelona

2

UAB

Universitat Autònoma de Barcelona

Modeling of RuO$_2$ Surfaces and Nanoparticles

Their potential use as catalysts for the oxygen evolution reaction

Javier Heras Domingo

Supervised by

Dr. Mariona Sodupe

Dr. Xavier Solans Monfort

A thesis submitted in fulfillment of the requirements

for the degree of Doctor of Philosophy

Chemistry Department

Universitat Autònoma de Barcelona

-2019-

UAB
Universitat Autònoma
de Barcelona

Memòria presentada per aspirar al **Grau de Doctor en Química** per Javier Heras Domingo.

Donen el seu vist i plau,

Dr. Mariona Sodupe Roure

Departament de Química

Facultat de Ciències

Universitat Autònoma de Barcelona

Dr. Xavier Solans-Monfort

Departament de Química

Facultat de Ciències

Universitat Autònoma de Barcelona

Bellaterra, 2019

A Joaquín y María

Abstract

Nowadays, the world energy supply comes mainly from carbon-based fuels, which is highly involved with environmental issues. Several decades ago, scientific studies about photosynthesis stated the ability of plants to oxidize water into oxygen powered by sunlight, storing energy as chemical bonds. Taking nature as inspiration, *water splitting* appears to be the most suitable process to produce clean energy from water, with the water oxidation reaction as the critical step.

In this thesis, state-of-the-art periodic DFT methods are used to understand the key factors that control water adsorption and the catalytic performance of RuO_2 on the oxygen evolution reaction (OER). For the first time, not only the most stable surface, but also all the surfaces that constitute the Wulff shape were taken into account for both the water interface and their catalytic activity. Wulff theorem was employed to build atomistic models of RuO_2 nanoparticles of different sizes. The OER performance of RuO_2 has been explored through the water nucleophilic attack (WNA) and oxo-coupling (I2M) mechanisms for both surfaces and nanoparticle models. Finally, two OER mechanisms have been proposed for an Iridium single site catalyst grafted on an Indium Tin Oxide (ITO) support as the work done during a predoctoral stay in ETH-Zürich (Switzerland).

Results show that water dissociation onto the RuO_2 main surfaces is controlled by the intrinsic Ru site acidity, the basicity of the O_{br} groups coming from the surface and cooperative effects between adsorbed water molecules. Concerning the OER mechanism, the WNA is the applying mechanism for both the main surfaces and nanoparticles. However, the I2M mechanism on nanoparticles seems to be significantly more favorable, because of the higher flexibility of the nanoparticle surface. Consequently, the I2M mechanism could be competitive on small clusters. Furthermore, results for the Iridium supported catalyst indicate that the highly oxidized Ir^{VI} bis-oxo is a key intermediate in the OER mechanism.

Index

Chapter 1

Introduction

> "Available energy is the main object at stake in the struggle for existence and the evolution of the world"
>
> *Ludwig Eduard Boltzmann*

One of most challenging both scientific and technical problem of the 21st century that is facing the humanity is the development of suitable devices to produce *clean energy.*[1] The world, as nowadays is known, relies in energy as the lifeblood of technological and economic development, which has a huge impact in the countries economic growth and into their internacional relationships.

Energy needs in 2015 arrive to the 575 quadrillion British thermal units (Btu) per year, and the projected energy demand is expected to be 663 QBtu·year^{-1} in 2030 or 736 QBtu·year^{-1} in 2040. This means that the global power consumption will increase from 16.6 to 24.7 terawatts (TW) per year. Unfortunately, the $\simeq 95\%$ of this energy comes from fossil fuels such as petroleum, natural gas or coal (Figure 1.1), which is directly connected to environmental issues, such as *air pollution* and *greenhouse effect.*[2]
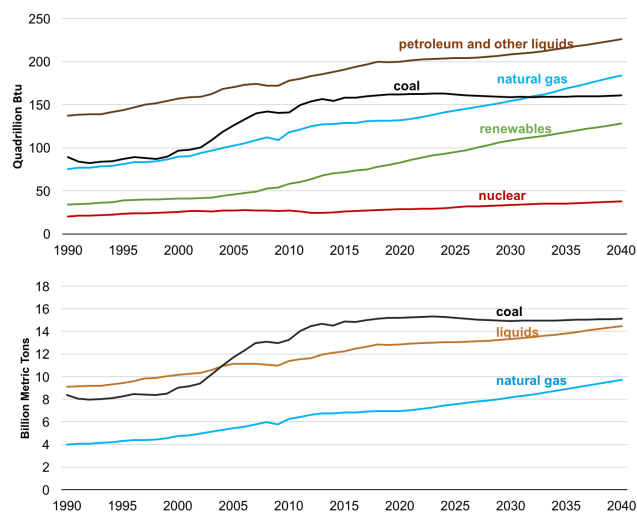
Figure 1.1: World energy consumption by energy source (top) and CO_2 emissions (bottom).

Although renewable energy and nuclear power are the world's fastest growing forms of energy, fossil fuels are expected to continue to meet much of world's energy demand.[3] Petroleum and other liquids remain the largest source of energy, sharing the world marketed energy fall from 33% in 2015 to 31% in 2040. From a worldwide point of view, liquids consumption increases in the industrial sector to power equipments, chemical feedstock and to provide industrial heat. However, it is decreasing in the electric power sector. On the other hand, natural gas is the world's fastest growing fossil fuel, increasing by 1.4 % per year, compared with liquid with a 0.7% growth and the stabilized growing of coal of 0.1% per year. It accounts for around 75% of the projected increase in total consumption between 2015 and 2040. However, the worldwide coal consumption will remain, the same between 2015 and 2040 (about 160 QBtu), being increasingly replaced by natural gas, renewable sources and nuclear power for electricity generation concerning coal consumption among different countries. China, remain the largest single consumer of coal in 2040 (about 73 QBtu), despite a steady decrease in the country's consumption over time, and in India, coal demand

is expected to increase by 90% between 2015 and 2040, as new electricity generating capacity.[4]

The atmosphere composition is changing due to human activities, and greenhouse gases have a huge influence on *global warming*[5] (Figure 1.1). Because of that in 2016 a huge number of countries around the world signed the Paris agreement to mitigate global warming and to maintain the temperature increase below 2 celsius grades above pre-industrial levels.[6] Despite technical difficulties, committed countries with the climate change are implementing measures to fulfill this agreement, increasing the amount of renewable energies, replacing common vehicles to electric ones and, in general, replacing coal by natural gas.

Human economy is highly related to the planet's natural capital such as oxygen, water and biodiversity.[7] Part of this reserve is regenerated spontaneously by the action of sunlight on the biosphere, but the ratio between the natural capital and regenerative power, results in a general depletion of the capital stock. The humanity load reached the 70% of the regenerative capacity of the global biosphere in 1961, reached a new top mark in 1980 with 100% and overpassed it in 1999 with a 120%.

Renewable energy sources, for instance wind, tides, sunlight and geothermal are good candidates for replacing fossil fuels as unlimited primary energy sources, despite being intermittent.[8] Furthermore, nuclear energy could be an alternative due to the low CO_2 emissions. Fission process is largely used for electrical energy supply, while fusion is still in its preliminary stages. Although, modern reactors are safer, a weak point in nuclear energy is the management of the nuclear waste, which leaves nuclear deposits being radioactive for thousand of years.

Consequently, there is a huge demand for environmental friendly, cost-effective and domestic alternatives that meets the energetic needs of nowadays and future generations. In fact, the sun strikes our planet by providing, in one hour, more energy than what is consumed during a whole year.[9,10]

On average, the energy from the sun received at the top of the Earth's atmosphere is about 175 petawatts (PW), of which 31% is reflected by clouds and from the surface. The rest 120 PW is absorbed by the atmosphere, land, ocean and finally emitted back to space as infrared radiation. Photovoltaic cells harvest energy from the sun and transform it into electricity. Although the amount of energy harvested only represents the 6% of the global energy consumption it is expected to be increased on the future.[11,12]

1.1   Photosynthesis

Harvest energy from sunlight is an attractive option due to the amount of energy per hour that is provided to our planet. Because of that, huge scientific effort is being done to convert solar energy into fuel and electricity. Through billion years of evolution, nature has evolved toward systems with the capacity to use the energy provided by sun. The photosynthetic system[13,14] is able to catch solar energy and reduce CO_2 to sugars and starches (carbohydrates) (Eq. 1.1), which constitutes a source of inspiration to design chemical systems that can transform solar energy to fuel and store energy as chemical bonds.

$$6\,CO_2 + 12\,H_2O \rightarrow C_6H_{12}O_6 + 6\,O_2 + 6\,H_2O \tag{1.1}$$
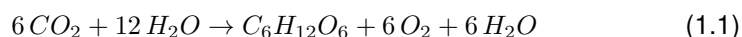
Photosystem II (PS-II)[15–17] is a large protein, whose molecular weight is around 650 kDa as a homodimer. It can be found embedded in the thylakoidal membrane of cloroplasts in green plants and in the internal membranes of cyanobacteria (Figure 1.2). The catalytic site, called *Oxygen Evolution Complex* (OEC)[18] placed in a protein subunit is a oxomanganase cubane-like cluster consisting on earth-abundant elements such as Ca^{2+}, (Mn^{3+}/Mn^{4+}) and $\mu-$oxo bridges (Figure 1.2). The reaction starts by harvesting light through an antenna complex to oxidize the chlorophyll species P680 to lead a radical cation P680$^{\cdot+}$. This radical cation oxidizes tyrosine Tyr_Z which is located close to the Mn_4Ca cluster. This photocatalytic process is repeated multiple times while evolving the OEC through five oxidation storage states (S_0 - S_4) along the Kok cycle.[19]
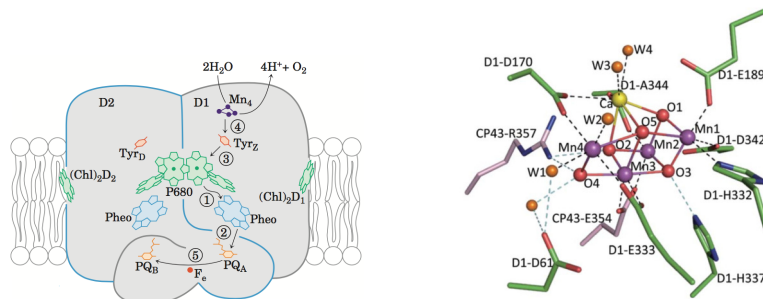
Figure 1.2: [Left] Photosystem II and [Right] Mn_4Ca-cluster structure. Reprinted with the permission from Ref.[20]

In the full oxidized S_4 state, the Mn_4Ca cluster catalyzes the oxygen evolution, completing the four-electron water oxidation that splits water into molecular oxygen, protons and electrons.[21,22] Experimental and computational characterization of the OEC structure and overall structural rearrangement during the stepwise photocatalytic cycle has been crucial to understand the reaction mechanism and for future design of artificial catalytic systems.[23–25]

1.2 Water Splitting Process

Inspired by nature,[26] the water splitting process[27,28] is a two coupled half-reactions, which deals with the splitting of two water molecules to finally produce hydrogen as energy carrier[29,30] (Eq. 1.2). The separate study of both half-reactions allows the rational tuning of specific catalysts for each case, as well as, the design of devices capable to perform the whole water splitting process.

$$2\,H_2O(l) \rightarrow 2\,H_2(g) + O_2(g) \tag{1.2}$$
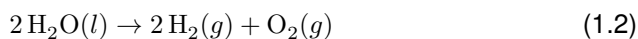
Innovative ideas have been proposed to achieve more efficient energy conversion or storage systems such as alkaline water electrolysis, fuel cells and metal-air batteries. The design of these systems are complicated,[31] but the essential ideas are well-known. All of them are based in two-electrode systems, where the cathode part involves hydrogen evolution reaction (HER) and the anode part

proceeds with oxygen evolution reaction (OER). The key reason that keeps these systems from the practical use to date is the slow kinetics of the oxygen evolution reaction. OER is a four electron-proton coupled reaction while HER is a two electron-transfer reaction, where it is expected that OER requieres higher energy to overcome the kinetic barrier to occur.

Note that the reactions at the cathode and anode parts for the water splitting reaction are different under acidic (Eq. 1.3) or alkaline (Eq. 1.4) conditions, as shown in the following equations. Acidic conditions requires the presence of second to third row precious-metals (Ru, Ir, Pt), while earth-abundant catalysts are only stable in neutral to alkaline conditions.

Acidic conditions:

Cathode reaction:
$$4\,H^+ + 4\,e^- \rightarrow 2\,H_2(g) \quad E_c^0 = 0.00V$$
Anode reaction:
$$2\,H_2O(l) \rightarrow O_2(g) + 4\,H^+ + 4\,e^- \quad E_a^0 = 1.23\,V$$

$$(1.3)$$

Alkaline conditions:

Cathode reaction:
$$4\,H_2O(l) + 4\,e^- \rightarrow 2\,H_2(g) + 4\,OH^- \quad E_c^0 = -0.83V$$
Anode reaction:
$$4\,OH^- \rightarrow O_2(g) + 2\,H_2O(l) + 4\,e^- \quad E_a^0 = -0.40V$$

$$(1.4)$$
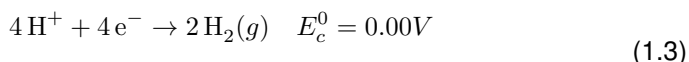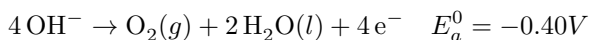
Solar-driven water splitting devices[32–34] mainly require the presence of a light absorber, fuel forming electrocatalysts, an electrolyte and a means to separate the electrochemical cells, which shows its optimal performance in acidic media as proton exchange membrane (PEM). The main proposed devices designs are the commercial photovoltaic electrolyzer cells (PV-Electrolyzer), photoelectrochemical cells (PECs) and mixed colloidal devices[35] (Figure 1.3).
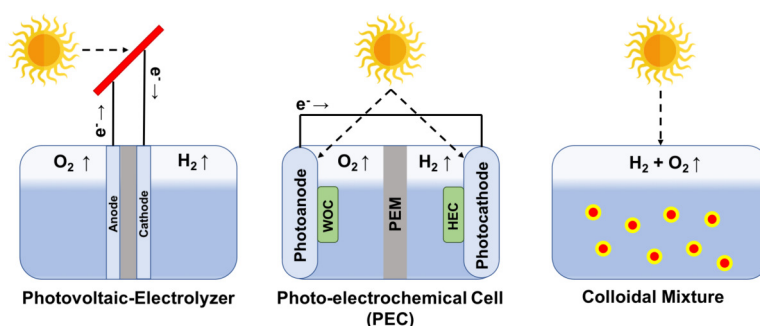
Figure 1.3: Schematic draw of three electrochemical devices for the light driven water splitting process.

The Photovoltaic electrolyzer cells (PV-Electrolyzer)[36,37] design use a commercial PV cell as light absorber, which is connected to a catalyst located in both anode and cathode electrodes. Main advantage is the large availability of PV cells and heterogeneous catalysts. However, the main drawback of such design is the high cost of the PV cells in a large-scale application. On the other hand, in mixed colloidal cells, the light harvester and catalyst are full integrated in discrete nanoparticles and suspended in the electrolyte, being a low-cost alternative to the PV-Electrolyzer cell. However, such design is not competitive enough needing enhancements in terms of stability and efficiency. Finally, photoelectrochemical cells[38] are in between in terms of efficiency and feasibility of PV-electrolyzer and the mixed colloidal cells.

Photoelectrochemical cells (PECs)[39–41] are a developing technology that has shown significant promise in providing a solution for hydrogen production and further reaching applications as the technology matures. There is still much research required before PECs are a viable technology. The benefits for success are worthwhile and compelling as fully developed PEC technology offers a limitless energy source while having a very little impact on the environment. This technique is somewhat similar to the process of electrolysis used in Proton Exchange Membrane fuel cells (PEMs), but instead of using electricity for the water splitting process, light from the sun is used as the energy source to obtain

hydrogen. PECs usually consist in a working and counter electrode, one or both being photoactive. An n or p-type semiconductor is generally used as working electrode with a platinum counter electrode. Electron-hole pairs are generated on the working electrode by photon absorption with an energy level equal or higher than the band-gap of the photoanode semiconductor. If an n-type semiconductor is used, electrons are collected in the photoanode being transported to the counter electrode through an external circuit. The photogenerated electrons are consumed to reduce protons into hydrogen (H_2) at the cathode, while holes take part in the oxidation of water into (O_2) and protons at the anode cell. In contrast, p-type semiconductors employed as working electrode photogenerate electrons able to reduce protons into (H_2), while in the counter electrode water is oxidized into (O_2) and protons. The overall reaction is the cleavage of water by sunlight. For instance, titanium oxide (TiO_2) has been extensively studied, but because of its large band gap (3-3.2 eV), TiO_2 absorbs only the ultraviolet part of the solar emission and so has low conversion efficiencies. Numerous attempts to shift the spectral response of TiO_2 into the visible, or to develop alternative oxides affording water cleavage by visible light, have so far failed. As a consequence, a catalyst is often proposed to improve their performance such as a water oxidation (WOC) or hydrogen evolving (HEC) catalyst. The water oxidation catalyst (WOC) is able to regenerate the electron-hole pair by subtracting electrons from the oxidation of water, while the hydrogen evolving catalyst (HEC) is able to speed up the reduction of protons to H_2.

1.3   Water Oxidation

The critical step for the water splitting process is the water oxidation reaction. It is definitely not easy to accomplish because, in contrast to the majority of redox reactions are single or two-electron processes,[42] H_2O oxidation involves the transfer of four electrons, bond rearrangements and the formation of a $O-O$ bond.[43] Thermodynamics associate a Gibbs free energy (ΔG) of 237 $kJ \cdot mol^{-1}$ and a minimum potential of $+1.229V$ vs NHE. Because the high oxidation potential

to oxidize H_2O this half-reaction is considered the bottleneck in the development of artificial solar fuel systems. A well performing water oxidation catalyst (WOC) should overcome easily such a hard process.

The reactions at the cathode and anode parts for the water oxidation reaction are different under acidic (red line) and alkaline (blue line) conditions, shown in Figure 1.4. Many research groups have proposed possible mechanisms for oxygen evolution reaction at the anode electrode for either acid or alkaline conditions, and some disparities and similarities among these proposed mechanisms are present. Most of the proposed mechanisms include the same intermediates such as $M-OH$ and $M=O$, while the major difference is probably featured around the reaction that forms oxygen (O_2). There are two different routes starting from the $M=O$ intermediate. One is the green route as depicted in Figure 1.4, through the direct combination of two $M=O$ to produce O_2, known as (I2M) mechanism. In contrast, water nucleophilic attack (WNA) involves the formation of the $M-OOH$ intermediate which subsequently decomposes to O_2. Despite this difference, the common consensus is that in oxygen evolution reaction (OER) the bonding interactions ($M-O$) within the intermediates ($M-OH$, $M-O$ and $M-OOH$) are crucial for the overall electrocatalytic ability.

The OER mechanism in acid conditions (Eq. 1.5) starts in a open position on the metal active site by adsorbing a first solvent coming water molecule and the subsequent oxidation to $M-OH$ as a proton coupled electron transfer (PCET) reaction. Secondly, the $M-OH$ intermediate is oxidized to the high-valent metal-oxo $M=O$ intermediate. Since $M=O$ intermediate is generated, two different routes could be possible. One is the (I2M) mechanism where two $M=O$ species interact between them to produce the desired O_2 molecule. In contrast, the (WNA) mechanism follows with a second water molecule that acts as nucleophile by attacking the $M=O$ species with a subsequent electron arrangement to cleave the metal-oxo π system and form the ($O-O$) bond.
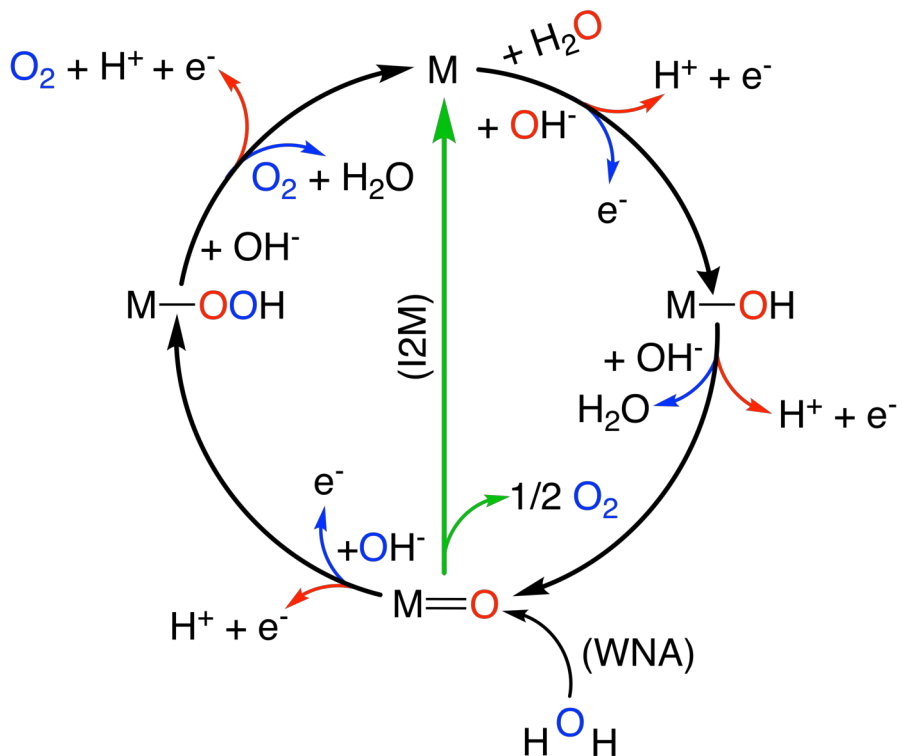
Figure 1.4: OER mechanism for acid (red line) and alkaline (Blue line) conditions. The black line indicates that the oxygen evolution involves the formation of a hydroperoxide (M-OOH) intermediate (WNA), while another route coupling two adjacent oxo (M=O) intermediates (I2M) is possible as well (green line), to produce oxygen.

Proposed mechanism under acidic conditions

$$M + H_2O_{(l)} \rightarrow M{-}OH + H^+ + e^-$$

$$M{-}OH \rightarrow M{=}O + H^+ + e^-$$

(Water Nucleophilic Attack)

$$M{=}O + H_2O_{(l)} \rightarrow M{-}OOH + H^+ + e^-$$

$$M{-}OOH \rightarrow M + O_{2\,(g)} + H^+ + e^-$$

(1.5)
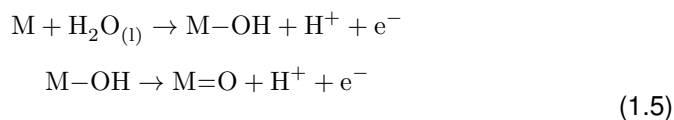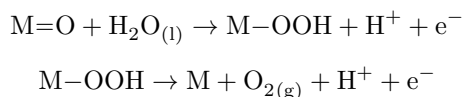
The OER mechanism in alkaline conditions (Eq. 1.6) differs from the acid conditions by adsorbing directly a OH$^-$ species on the metal open site as a one electron oxidation reaction. This M$-$OH species is deprotonated due to the huge concentration of OH$^-$ species to finally get the high-valent metal-oxo M$=$O species and a water molecule as a subproduct. Here again the mechanism can undergoes towards a (I2M) or a nucleophilic attack route. The (I2M) mechanism follows the same route through the direct interaction of two M$=$O species. Alternatively, this M$=$O intermediate can be attacked by a OH$^-$ species reaching the hydroperoxo M$-$OOH intermediate which undergoes to the production of a O$_2$ and water molecule due to a deprotonation process of the starting M$-$OOH species delivering the reducing power to the cathode cell.

Proposed mechanism under alkaline conditions

$$M + OH^- \rightarrow M{-}OH + e^-$$

$$M{-}OH + OH^- \rightarrow M{=}O + H_2O_{(l)}$$

(Nucleophilic Attack)

$$M{=}O + OH^- \rightarrow M{-}OOH + e^-$$

$$M{-}OOH + OH^- \rightarrow M + O_{2\,(g)} + H_2O_{(l)} + 2\,e^-$$

(1.6)
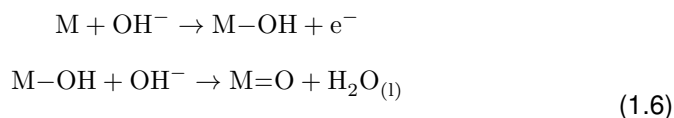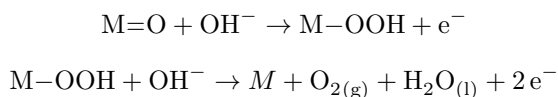
This thesis focuses in the OER mechanism in acid conditions, because noble metal oxides from the second and third row performs better in such conditions.

1.3.1   Electrocatalytic Kinetics

An electrocatalyst is indeed a catalyst that is able to facilitate electrochemical reactions; that is reactions that involve a charge transfer process.[44,45] In general, the main function of the electrocatalyst is to adsorb the reactant on the surface to form the adsorbed intermediate and boost the charge transfer between the electrode and the reactant. In electrocatalytic kinetics there are many useful parameters such as the overpotential (η), the exchange current density (i_0) and the Tafel slope (b), which are used to evaluate the performance of the electro-catalysis. These parameters are crucial, offering information on the mechanism of the electrochemical reaction.

Overpotential (η)

It is one of the most important descriptors to evaluate the performance of the desired electrocatalyst. Ideally, the applied potential to drive a specific reaction should be equal to the potential of the reaction at equilibrium conditions. However, it is always not the case and the applied potential usually is much higher than the ideal potential at equilibrium, to overcome the electrode kinetic barrier of the reaction.

$$E = E^0 + \frac{RT}{nF} \ln \frac{C_O}{C_R} \tag{1.7}$$

Looking to the Nernst equation (Eq. 1.7), E is the applied potential and E^0 is the formal potential of the overall reaction, T is the temperature, R the universal gas constant, F the Faraday constant, n the number of transferred electrons in the reaction, and C_O and C_R are the concentrations of the oxidized and reduced reagents, respectively. The overpotential is defined as the difference between the applied potential E and the potential under equilibrium conditions (Eq. 1.8).

$$\eta = E - E_{eq} \tag{1.8}$$

The overpotential is usually referred to a value that it is applied to achieve a specific current density, which means that a lower overpotential of an electrocatalyst in the system indicates its superior electrocatalytic ability for a studied reaction.

Exchange current density (i_0)

Another important indicator for electrocatalysis kinetics is the exchange current density i_0 (Eq. 1.9). For a target reaction, the global current (j) is the sum of the anodic (j_a) and cathodic (j_c) currents and the contributions from each anode and cathode ends are expressed in (Eq. 1.10) and (Eq. 1.11) respectively.

$$j = j_a + j_c \tag{1.9}$$

$$j_a = nF \cdot k_a [C_R] \exp\left(\frac{\alpha_a nFE}{RT}\right) \tag{1.10}$$

$$j_c = nF \cdot k_c [C_O] \exp\left(\frac{\alpha_c nFE}{RT}\right) \tag{1.11}$$

Where, ka, k_c and α_a, α_c represent the rate constant of the anodic or cathodic half-reaction and transfer coefficient for each, respectively.

At equilibrium conditions ($\eta = 0$; $E = E_{eq}$), both anodic and cathodic currents are equal ($j_a = j_c$), which results in a zero total net current. That magnitude at $\eta = 0$ refers to exchange current (j_0), where it is normally expressed by the total area of the electrode (A) becoming the exchange current density $i_0 = {j_0}/{A}$.

The exchange current density (i_0) reflects the intrinsic bonding/charge transferring interaction between the electrocatalyst and reactant. A high exchange current density is usually a good indication of being a good electrocatalyst for the target reaction.

Tafel slope (b)

Due to practical purposes, a high overpotential (η) needs to be applied to have a significant current density (i). In general, a smaller overpotential with a faster increase in the corresponding current density (i) is desired. The current density (i) and the applied overpotential (E) can be selected according to the Butler-Volmer equation (Eq. 1.12).

$$i = i_0 [\exp\left(\frac{\alpha_a nFE}{RT}\right) + \exp\left(\frac{\alpha_c nFE}{RT}\right)] \tag{1.12}$$

Under high anodic overpotential conditions, the overall current is mainly attributed to the anodic end while the contribution from the cathodic part is negligible. Then, the general Butler-Volmer equation can be simplified as (Eq. 1.13) which is also known as the Tafel equation.

$$i \approx i_0 \exp\left(\frac{\alpha_a n F \eta}{RT}\right) \tag{1.13}$$

The Tafel equation can be converted into a logaritmic function, where the exchange current density (i_0) and Tafel slope (b) can be calculated by representing the line equation (Eq. 1.14). The Tafel slope (b) can be expressed as (Eq. 1.15), where the definition of Tafel slope is how fast the current increases against overpotential, showing a huge dependency on the transfer coefficient (α), which normally is equal to 0.5 for single-electron processes.

$$\log(i) = \log(i_0) + \frac{1}{b} \cdot \eta \tag{1.14}$$

$$b = \frac{\partial \eta}{\partial \log i} = \frac{2.303 RT}{\alpha F} \tag{1.15}$$

A smaller Tafel slope (b) indicates that current density can increase faster with smaller overpotential (η) change, which implies good electrocatalytic kinetics. Tafel slope provides helpful information toward the mechanism of the reaction, especially to elucidate the rate-determinant step. From Eq. 1.15 usually refers to the symmetry factor β which is equal to 0.5 when the overpotential is smaller than the re-organization energy resulting in a tafel slope of 120mv dec^{-1}. This implies that the rate-determinant step in the electrochemical system is controlled by a single-electron transfer step. In more complex situations systems often consist of a series of consecutive reaction steps and the transfer coefficient can be derived from the Bockris and Reddy equation.

$$\alpha = \frac{n_b}{\nu} + n_r \beta \tag{1.16}$$

Where n_b is the number of electrons that transfer back to the electrode before the rate-determinant step, ν is the number of rate-determinant steps that have taken place the overall process, and n_r is the number of electrons that participate in the rate-determining step. It is unlikely to have more than one electron transferred simultaneously, and hence n_b is either 1 or 0. Once the rate-determining step is an electron transfer reaction, n_b is equal to 1 while the value of n_b is 0 in the case of a chemical step. The power of Eq. 1.16 is the prediction of the rate-determinant step, for instance, if the first electron transfer reaction is the rate-determinant step, the values both n_b and ν are equal to 0 while n_r and β are 1 and 0.5 respectively, resulting in a transfer coefficient of 0.5 and a Tafel slope of 120 mV dec^{-1}. If the rate-determinant step is the a chemical process after one-electron transfer reaction, the values of n_b and ν are equal to 1 while n_r is 0. Consequently, the transfer coefficient is 1 and the Tafel slope becomes 60 mV dec^{-1}. Typically for OER systems, if the rate-determinant step is the third electron transfer, n_b and ν are equal to 2 and 1 (n_r and β are 0) yielding a transfer coefficient of 2 and a Tafel slope of 30mV dec^{-1}.

1.4   Water Oxidation Catalysts (WOC)

Water oxidation catalysis has been proved with many different kinds of systems: from organometallic complexes as homogeneous catalyst,[46] metals to metal oxide surfaces as heterogeneous catalyst and nanocatalysts to provide fundamental understanding of the reaction onto different materials. The electrocatalytic capacity of such materials is determined both experimentally and theoretically, to evaluate the reaction mechanism.

In the following subsections different kinds of catalysts in the field of water oxidation process will be presented, and their advantages and disadvantages as a function of their ability to catalyze the water oxidation reaction and their applicability in electrochemical devices will be compared. The recurring question that often arises is whether the true catalytic species is homogeneous, consisting of a well-defined molecular complex, or an heterogeneous active site. Resolving the

homogeneity-heterogeneity problem is critical to know the catalytic mechanism by which the reaction is mediated. For colloidal nanocatalysts the differenciation between homogeneous and heterogeneous catalysis is unclear.

1.4.1   Homogeneous Catalysts

In this section, ruthenium and iridium both single-metal and dinuclear complex will be described since most of the mechanistic knowledge for water oxidation catalysis comes from studies carried out with these metal complexes. However, this information can be extensible to the rest of catalysts based on other transition metals.[47,48]

Ruthenium Molecular Complexes

Ruthenium is located in the second transition metal series of the *periodic table*. With an electronic configuration [Kr] $4d^7$ $5s^1$, it gives access to the widest variety of oxidation states, from Ru^{8+} to Ru^{2-}, which correspond respectively to d^0 and d^{10} electronic configurations. Coordinated with polypyridyl ligands, ruthenium complexes are usually stable at high oxidation states, showing an octahedral geometry, and their redox properties can be tuned. In general, organometallic complexes offer the possibility to analyze their activity as a function of their ligand coordination.[49,50]

In 1982, the first complex capable of mediating the four proton-coupled electron transfer (PCET)[51] process to oxidize H_2O, was reported as the dinuclear μ-oxo-bridged ruthenium complex *cis,cis*-[(bpy)$_2$(H$_2$O)Ru(μ-O)Ru(H$_2$O)(bpy)$_2$]$^{4+}$ more commonly known as the "blue dimer" due to its characteristic blue color (Figure 1.5 [a]).[52,53] This study proved that the hard multielectron oxidation of H_2O to O_2 was possible. First studies revealed a limited catalytic activity, with 13.2 turnover number (TON) and a $4.2 \cdot 10^{-3}$ seg^{-1} of turnover frequency (TOF). The presence of the μ-oxo bridge allows a strong electronic coupling between the two metallic centers, that stabilizes high oxidation states by electronic delocalization. The mechanism proposed by Meyer group involved four stepwise PCET that give rise

to high-valent Ru^V-Ru^V intermediate.[54] The main reason of its low activity is related to the instability of the μ-oxo bridge, which is cleaved into two nonactive monomeric ruthenium complexes. Different studies have achieved stable blue dimer derivatives by tunning organic ligand structures capable to connect strongly the two ruthenium centers in a close proximity.

Another well studied ruthenium complex $[Ru_2(OH_2)_2(bpp)(tpy)_2]^{2+}$ were Hbpp corresponds to 2,2'-(1H-pyrazole-3,5-diyl)dipyridine ligand, was also reported (Figure 1.5 [b]),[55,56] being the first dinuclear ruthenium complex lacking a $[Ru-O-Ru]$ scaffold capable to oxidize H_2O to O_2. In this complex, the two ruthenium centers are placed at a close distance, in a *cis* orientation to one another, by the addition of a rigid pyrazole scaffold as a conjugated bridge between the two metal atoms. Extensive both experimental and theoretical studies have demonstrated that $[O-O]$ bond formation proceeds only through the (I2M) pathway. Compared to the blue dimer it is more than 3 times faster in similar conditions, but still shows a moderate catalytic performance, the maximum TON being 17.5 and the overall efficiency 70%. The absence of the μ-bridge avoids decomposition pathways, which was a limitation of the blue dimer complex. Nevertheless, the efficiency is still low due to the oxidation of the $C-H$ group of the pyrazole scaffold in the bridging ligand. Further modifications adding an extra methyl group in the pyrazole moiety increases its performance.

(a) Blue-dimer complex.

(b) Ru(Hbbp) complex.

R = NMe2
R = CH3
R = CF3

(c) Meyer's Ru complex.

R = H
R = CH$_3$
R = Ph-NH$_2$
R = Ph-N$_2$$^+$

(d) Ru(bda) type complex.
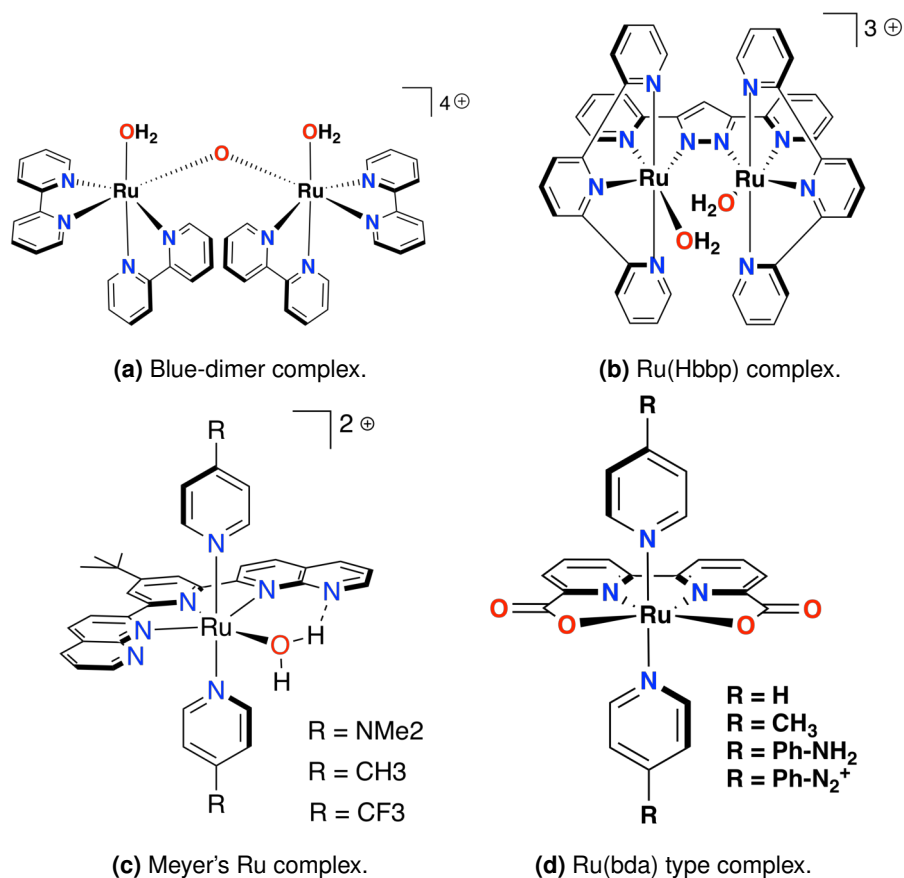
Figure 1.5: Ruthenium complexes, from dinuclear to single-site catalysts.

Artificial molecular water oxidation catalysts (WOCs) were designed with the idea that accommodating multiple metal centers was fully required to achieve the 4 stepwise PCET process. It was only in 2005, that Thummel group reported[57,58] a proof that four electron oxidation from H$_2$O could be possible on a single-site metal complex. The ruthenium metal center was coordinated with the tridentate 2,6-di(1,8-naphthyridin-2-yl)pyridine polypiridil ligand exhibiting uncoordinated nitrogen atoms. Those nitrogen atoms interact with aqua ligands through hydrogen bonds stabilizing the aquo complex (Figure 1.5 [c]). In 2008 Meyer and co-workers reported[59] a complete mechanistic study that demonstrated the mononuclear nature as a catalyst. The suggested catalytic cycle follows a WNA

mechanism. The reaction starts with a Ru^{II}-OH_2 species and oxidizes to Ru^V=O in acidic conditions, containing a high electrophilic oxo-group able to react with a water molecule coming from the solvent, generating the corresponding hydroperoxide species Ru^{III}-OOH. In addition, another oxidation is required to activate the catalyst and form Ru^{III}-OO, as rate-determinant step (RDS) to finally evolve O_2 and restart the catalytic cycle.

Interestingly Ru complexes containing the equatorial bda^{2-} ([2,2'-bipyridine]-6,6'-dicarboxylate) ligand are the fastest molecular water oxidation catalysts described so far in the literature[60–62] (Figure 1.5[d]). Two crucial features of Ru−(bda) is the capacity of the carboxylate moieties present in the ligand to form intramolecular hydrogen bonds with the active Ru−OH group at different oxidation states, which is beneficial for the catalysis in terms of both thermodynamics and kinetics. Other key feature is the ligand capacity to stabilize Ru at high oxidation states via the anionic character of the carboxylate groups and also via the formation of seven-coordinated beyond oxidation state IV. This stabilization reduces the overpotential for the catalytic reaction up to 740 mV in comparison to other mononuclear Ru complexes with the classical octahedral coordination.

Many works have been devoted to molecular mononuclear metal complexes, not only with ruthenium, but also with iridium based complexes, as well as earth abundant metals such as cobalt,[63–66] copper[67,68] or iron.[69,70]

Iridium Molecular Complexes

A significant discovery on the field of H_2O oxidation catalysis occurred when the first iridium mononuclear cyclometalated complex was able to accomplish H_2O oxidation[71,72] (Figure 1.6-*left*). This complex employs a cyclometalated phenylpyridine (ppy) as bidentate ligand, and takes advantage of the strong iridium-carbon bond to afford the oxidative hard conditions required for H_2O oxidation (TON 2490 n_{O_2}/n_{cat} and TOF 0.0041 S^{-1}).
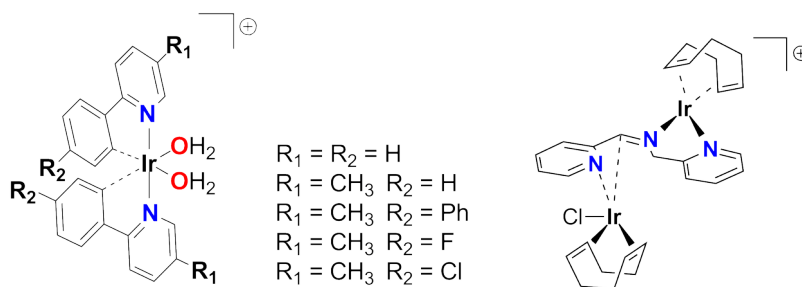
Figure 1.6: Ir complexes, [Left] mononuclear and [Right] dinuclear catalysts.

Theoretical studies of the iridium mononuclear complex were performed, with the aim to bring out a feasible mechanism through the (WNA) of H_2O on the generated iridium-oxo species to form the desired $O-O$ bond.[73] The reaction follows an acid/base mechanism, in which the $O-O$ bond is generated by the attack of water to the electrophilic $Ir=O$ moiety. The proton released by water is transferred to different acceptors, depending on the nature of the ancillary ligand. Such ligand depends on the pH conditions and can range from OH_2, OH or O^{-2}. With the OH_2 aquo ligand, the $Ir=O$ plays a double role by both making the $O-O$ bond and accepting the proton in the WNA. In contrast, with OH^- ligand, the $Ir=O$ makes the $O-O$ bond and the hydroxo ligand takes the proton. Finally, with the O^{-2} oxo ligand one, makes the $O-O$ bond whereas the other accepts the proton. Such ligand cooperates to facilitate the reaction by generating the nucleophilic hydroxide anion. As the basicity of the ligand increases from OH_2 to O^{-2}, the energy barrier decreases. This feature suggests that water oxidation catalysts may be improved with ligands able to act as internal bases.

In general, dinuclear metal complexes (Figure 1.6-*right*) can be more stable than mononuclear ones, because it capacity to distribute the oxidizing equivalents over several metal centers. The synthesis of dinuclear iridium complexes such as $[(cod)(Cl)Ir(\mu\text{-bpi})Ir(cod)]^+$, where (bpi) is a (pyridin-2-ylmethyl)(pyridin-2-ylmethylene)-amine was achieved. The first Ir center is coordinated to the imine nitrogen through σ-coordination, which activates the imine scaffold towards η^2 coordination to the other Ir center.

Although the extensive amount of metal complex able to perform the H_2O oxidation, the main structures and their performance have been discussed. This acquired knowledge can be extrapolated to the rest of molecular catalyst being useful to understand heterogeneous and colloidal catalysts.

1.4.2   Heterogeneous Catalysts

As explained in the previous section, significant progress has been made along the last century in terms of the design of new organometallic complexes for water oxidation.[74] Heterogeneous catalysts are, however, more advantageous due to their huge surface area, which leads to improved efficiency. Furthermore, high temperatures and hard conditions are often applied in industrial catalytic processes, which makes heterogeneous catalysts more convenient, since homogeneous catalyst are often decomposed, losing their catalytic activity at these conditions.[75]

The heterogeneous catalysts may facilitate the adsorption of the reactants and their subsequent conversion into products. However, the product must be rapidly removed from the surface to regenerate the active sites from the surface. This leads to the concept that the catalytic reaction is a cycle which is made up of elementary phisicochemical processes such as, chemisorption, dissociation or activation, diffusion, recombination and finally desorption.

Chemisorption is defined as the adsorption of reactants or intermediates on the catalyst surface with an interaction energy which is strong enough to form chemical bonds between the adsorbate and the surface and to weaken internal bonds within the adsorbate. This leads to the activation or dissociation of the adsorbate molecule. When the interaction between product molecules and the catalyst becomes too strong the desorption of product molecules becomes rate-limiting, decreasing the overall speed of the reaction. This leads to a balance between a sufficient catalyst-adsorbate bond strength to activate the adsorbate and surface poisoning, which should be avoided.

As a result, a volcano-type plot[76] (Figure 1.7) of the catalyst activity against reactant-interaction strength can be drawn, the catalytic activity increasing up to a particular interaction strength known as the *sabatier maximum*. This shape of the plot is a consequence of the *Sabatier principle*[77] which states that the rate of a catalytic reaction is maximized at an optimum interaction strength of the reactants with the catalyst, providing a rational strategy to optimize the catalyst features.
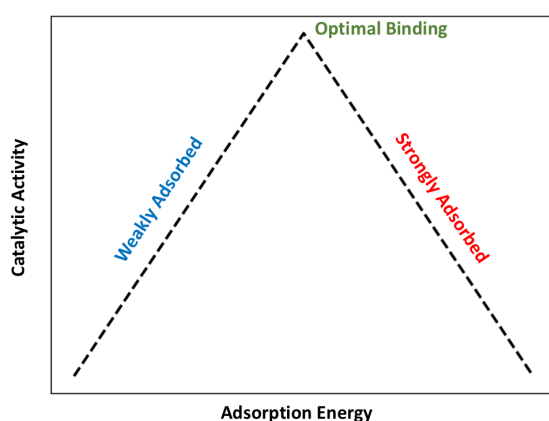
Figure 1.7: Sabatier volcano plot as Catalytic activity vs. Adsorption Energy.

Since OER is a surface reaction, the surface morphology also plays a significant role in the electrochemical performance. Thus, the problem is not limited only to find the best material but also the best morphological structure. The surface architecture should be characterized and designed according to the electrocatalytic mechanism. This becomes even more complicated for multi-component electrocatalysts, where each component and also the position of each active site may have a different role in the overall mechanism.

In this section conventional materials such as metal oxides and mixtures of different metals with practical potential use are described. Since the OER performance is highly dependent on the material and structure, it is difficult to simply classify the performance in accordance with the electrocatalyst material.

Metal Oxides

Unfortunately, water oxidation is constrained by the kinetically sluggish oxygen evolution reaction (OER) because it is thermodynamically and kinetically unfavorable for removing four electrons to form oxygen. Consequently, a huge amount of effort has been devoted to develop catalysts for more effective water electrolysis. Metal oxides, including RuO_2 and IrO_2-based electrodes, first-row metals (Mn, Co, Ni, Cu) oxides, hydroxide layers, spinels and perovskites have been intensively studied.

First-row Metal Oxides

Due to the similarities with the Mn_4Ca cluster present in the OEC (Figure 1.2), the performance of MnO_2 in OER has been studied. However, it's poor conductivity keeps it behind its counterparts.[78] Adding metallic catalysts contributes to the electrocatalytic activity enhancing significantly the electrical conductivity. Indeed, grafting Au^0 nanoparticles on α-MnO_2 improves the electrocatalytic activity about 6 times.[79] Electronic interaction provided by gold promotes the formation of the most active Mn^{3+} sites for OER. α-MnO_2 is a promising structure for the OER performance, while β-MnO_2 has a poor activity due to the absence of di-μ-oxo bridged Mn centers.[80,81]

Co_3O_4 has a significant good performance as an OER electrocatalyst, although only $^1/_{1000}$ of the exposed sites are responsible for the electrocatalytic activity.[82–84] As proposed in the literature, these minority sites are Co^{4+} cations connected through bridging oxo species, which can effectively interact with water molecules.

The significant point is that the active sites are subject to change by varying their overpotential. This suggest that the overall system is quite dynamic, and can not be simply predicted based on the initial material or structure. In addition, the presence of Co^{3+} and Co^{4+} provides a good environment for the creation of active sites depending on the ratio. Since OER is firstly based on the adsorption on the catalyst surface, the electronic states play an essential role in its electrocatalytic activity and structure doping, facet growth control and oxygen vacancies have

been used to enhance the electro-performance of Co_3O_4 for OER.

For crystalline electrocatalyst, the crystal orientation plays an important role in the OER performance due to the different number of active sites on each surface.[85] Since the active sites in Co_3O_4 involves a Co^{3+} rather than Co^{2+}, the OER kinetics can be faster on a Co^{3+} rich facet.

Following with first row transition metal oxide derivatives, Cu is cheaper than Co and has a well-defined coordination chemistry and a wide redox capability. Copper oxide[86,87] has a moderate activity for the OER performance, and this activity can be tuned by the surface morphology. However, the electrocatalytic activity of copper oxides is significantly lower than cobalt.

Perovskites

Perovskites[88–90] with structure ABO_3 is a metal oxide class of OER catalysts that has been intensively studied. Their physicochemical and catalytic properties can be tunned up by substituting ions of the same or different oxidation states in the A or B structural sites. The OER electrocatalytic activities of substituted perovskites $(A_{1-x}A^{'}_xBO_3)$, where A is a lanthanide usually (La), A$^{'}$ is an alkaline earth metal such as Sr, and B is a first-row transition metal, are reported.

Recently, the e_g filling of the surface transition metal cation has been shown to greatly influence the binding of OER intermediates on the perovskites surface and their OER activity. The intrinsic OER activities exhibit a volcano type dependence on the occupancy of e_g orbitals of surface transition metal cation in an oxide. Indeed, the highest OER activity among all oxides studied as predicted by the e_g activity descriptor is $Ba_{0.5}Sr_{0.5}Co_{0.8}Fe_{0.2}O_{3-\delta}$ (BSCF).[91]

Spinels

The general formula is $A^{'}B^{'}_2O_4$ where A$^{'}$ and B$^{'}$ atoms are usually made up of group 2, group 13 and first-row transition metal elements. This structure shows two crystallographic octahedral (O_h) and tetrahedral (T_d) sites. That leads to two types of spinel. The normal spinel has a configuration of $(A^{2+}_{Td})(B^{3+}_{Oh})O_4$ and

the other is the inverse spinel $(A_{Oh}^{2+})(B_{Td}^{3+})(B_{Oh}^{3+})O_4$, according to the crystal field theory[92] the difference in metal coordination results in a different d-band splitting $e_g t_{2g}$ for T_d and $t_{2g} e_g$) for O_h sites.

Most spinel oxides are iron-based and cobalt-based compounds with other transition or alkaline metals as dopants agents. In the case of iron-based systems (MFe_2O_4) where $M = Co$, Ni, Cu or Mn the OER activity trend is ($CoFe_2O_4$) > ($NiFe_2O_4$) > ($CuFe_2O_4$) > ($MnFe_2O_4$).[93–95] Nevertheless, the situation becomes different for cobalt-based systems ($M_xCo_{3-x}O_4$) where adding $M = Li$, Ni or Cu would be beneficial except for Mn in terms of OER activity.[96,97] The reason why Mn lowers the OER activity in cobalt-based spinels is attributed to the suppression of the Jahn-Teller distortions.[98]

Nobel Metal Oxides

Noble metal oxide catalysts based on RuO_2, IrO_2 are important OER catalysts, in acidic conditions.[99–102] These metal oxides are in the top of the volcano plot (Figure 1.8), which means that the intermediates binding energies correlate in a good compromise for the OER. These two precious metal oxides adopt a rutile structure, where Ru or Ir are located in the center of an octahedral site with oxygen in the corners, being shared between octahedrons, both RuO_2 and IrO_2 are considered as benchmark electrocatalysts owing to their high electrocatalytic activities toward OER. However, the OER performance are highly influenced by the synthesis methodology and catalyst nature.
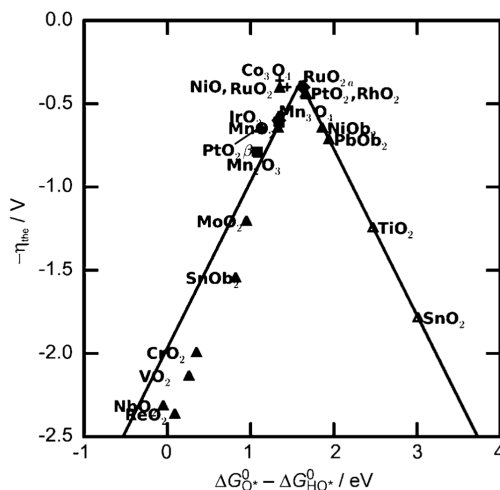
Figure 1.8: Activity trends towards OER for metal oxide materials.

The performance of RuO_2 is better than IrO_2, but it is not stable in conventional electrolytes. Experimentalists have shown that the OER performance of electrochemically deposited RuO_2 is better than that of the chemically synthesized RuO_2, but its stability is worse. Moreover, IrO_2 films exhibits excellent OER activity reaching a higher current density than RuO_2 nanoparticles with the same overpotential conditions $\eta^{OER} = 0.275$ V.

To improve the stability of RuO_2, doped bimetallic oxide systems ($Ru_xIr_{1-x}O_2$) have been proposed. This systems turned out to be very effective and only a small amount of Ir was incorporated into the catalyst, which could significantly suppress the deterioration without sacrificing much performance of OER.[103]

As can be seen, there is a lot of controversy about which is the best option taking into account electrochemical activity and chemical stability of those heterogeneous catalyst, that's why both experimental and theoretical studies are needed to find the optimal candidate.

1.4.3   Nanocatalysts

Over the last decade there has been an increase in the interest on nanochemistry. A variety of nanosized materials such as graphene sheets (2D), carbon nanotubes (1D) and, metal or metal oxide nanoparticles (0D) have been synthesized and proposed as potential building block of optical and electronic devices, as well as catalyst due to their enhanced surface chemistry. As a consequence, there is a necessity to fully understand and characterize from an atomistic point of view their structural and chemical properties.[104–106]

Nanoparticles are used as catalysts in a wide range of chemical reactions. In particular, these systems are of high interest due to the presence of active sites involving shell structural defects or low-coordinated atoms. Furthermore, semiconductor nanoparticles have received great attention due to their unusual electronic and enhanced optical properties compared to bulk materials. Indeed, when the size of the nanocatalyst decreases from bulk size to the nanosize level, new unique both chemical and physical properties emerge. Generally in nanoscience, goals are the full control over the size, shape, optical, electronic, magnetic and structural behaviors. In this context, theoretical approaches may contribute to elucidate the reactivity of differential sites and these differential properties in comparison with macroscopic ones.

Nanosized electrocatalysts for OER are of considerable interest because their composition, size, shape and crystallinity are crucial and strictly related to macroscopic surface properties, which may lead to huge changes into their chemical reactivity. As known, it is beneficial to reduce the particle size, because the effective surface is increased, forming more active sites for OER. In a similar way, core-shell combinations of two materials have displayed a superior electrocatalytic activity, which is attributed to the formation of uncommon phases at the materials interface and the creation of other interfacing active sites.

Metal Oxide Nanoparticles

Recently a wide number of approaches have been employed for the synthesis of nanoparticle catalysts including thermal evaporation in vacuum, electron-beam lithography and pulsed laser deposition, buffer-layer assisted growth, chemical vapor deposition, gas condensation, ionized cluster beam deposition, electrochemical deposition methods, sol-gel or colloidal techniques, deposition-precipitation and impregnation methods, molecular cluster precursors and many more. The main requisite of these approaches is the production of robust materials that preserve their initial morphologies, or at least their narrow size distribution under reaction conditions with minimum coarsening.

RuO_2 and IrO_2 heterogeneous catalyst are the most active materials for the OER reported to date, in acidic conditions. Nobel metals have a high cost and low earth abundance, making nanoparticle catalysts more interesting because of their enhanced activity requiring lower amount of catalyst. For instance, iridium oxide nanoparticles have been synthesized in aqueous phase[107,108] or using dimethyl sulfoxide (DMSO)-metal adducts,[109] and ruthenium oxide nanoparticles can be made via chemical vapor deposition,[110] electrochemical deposition[111] and polyol methods.[112,113] However, the OER activities of these metal oxide nanoparticles are often not comparable, differences being attributed to different particle sizes, crystal structures (rutile or amorphous), and different degrees of surface hydration.

Interestingly, these metal oxide nanoparticles can be synthesized by first obtaining the corresponding metal nanoparticle in an oleylamine-mediated solution both starting from the $IrCl_4 \cdot xH_2O$ or $RuCl_4 \cdot xH_2O$ as salt reduction approach, followed by thermal oxidation of the nanoparticles in an oxygen atmosphere. This methodology needs the presence of a reducing agent such as $NaBH_4$ or the classical sodium citrate for gold nanoparticles in the Turkevich method[114] which acts both as reducing agent and capping ligand. Capping agents are used in nanoparticle synthesis to stop the particle growth and aggregation. However, nanoparticle catalysts requires a clean surface like the ones obtained with the organometallic

approach.[115,116] This methodology uses an organometallic precursor as metal source, stabilized by the ligand double bonds as in the [Ru(COD)(COD)] complex and 3 bar pressure of H_2 to reduce the ligand double bonds and deliver nude Ru^0 atoms to the reaction media. Metallic nanoparticles start to grow until the stabilizing ligand surrounds the nanoparticle surface avoiding its growth and aggregation.

Characterization by X-ray diffraction (XRD) and high-resolution transmission microscopy (HRTEM) is required to determine the crystallinity of the synthesized materials, size distribution and aggregation.
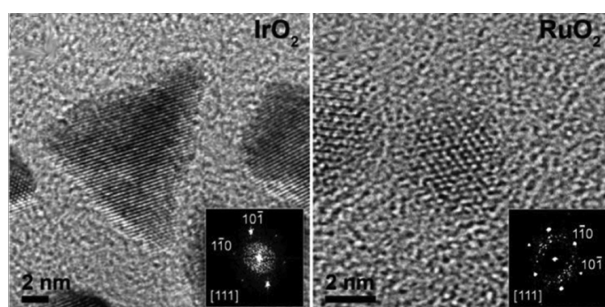
Figure 1.9: HRTEM images of IrO_2(left) and RuO_2(right) with FFTs indexed to the rutile structures showing the corresponding (110) and (101) Miller index.

It is generally observed that the specific OER activities are higher in acid than in basic media for both RuO_2 and IrO_2 nanoparticles. Interestingly, the specific OER activity of IrO_2 nanoparticles dispersion is slightly lower than that of RuO_2 at low overpotentials in both acidic and alkaline reaction conditions. This tendency is in agreement with the computational study reported by Rossmeisl et al., that describes the optimum bonding strength to the OER intermediate species following the Sabatier principle statements discussed above. Another way to enhance their electrocatalytic stability is to synthesize a core-shell structure ($IrO_2 @ RuO_2$) and once subjected to OER electrocatalysis. It has been elucidated that this core-shell conformation can not only lower the overpotential but also increases the whole stability.[117]

1.4.4   Hybrid Catalysts

There is an extensive library of available WO catalysts, as metal complexes or nanoparticles showing promising OER performance because of their high activity and tunability, as well as their capacity to be integrated into complex assemblies. The major drawback is their limited stability, with the best homogeneous or colloidal systems providing huge turnover numbers. Such problem is particularly significant for electrode driven water oxidation catalyst (WOC), which often decompose to less active species under hard oxidative conditions.

The fundamental idea behind the *hybrid catalyst*[118–120] is that they might benefit from the individual properties of their homogeneous and heterogeneous constituents, as the limitations of ones are usually the main advantages of the others, working in a synergistic manner. Different heterogenization strategies for homogeneous catalyst in organometallic, inorganic and surface chemistry have been developed to immobilize such molecular water oxidation catalyst (WOC) onto the electrode surface.

In the case of an electrode driven water oxidation catalyst (WOC) the ligand anchoring the active specie to the electrode surface must display a huge degree of oxidative stability, which is probably the most difficult achievement. However, to date, there are many ways to combine high efficient and tunable one well-defined active site (single-site) complexes or dinuclear derivatives with the durability and stability of a macroscopic material in a heterogeneous electrocatalyst for water oxidation. The surface organometallic chemistry (SOMC)[121–124] approach treats the surface of the catalyst support as a ligand to control its reactivity toward molecular precursors, such as organometallic or coordination complexes. The grafted molecular complexes can be used directly in catalysis or transformed after grafting by a thermal post-treatment under vacuum, inert or reactive gas, or modified by a post-reaction to incorporate new ancillary ligands. This approach permits well-defined surface species to be prepared and fully characterized with techniques complementary to those of solution chemistry. Surface organometallic

chemistry (SOMC) approach has been employed since the 1970s to generate single-site catalysts, supported metal nanoparticle catalysts, and even extended structures from grafted species. The main advantage of SOMC lies in its ability to obtain surface sites with a known coordination sphere, thus facilitating structure-activity relationship studies and rational design of heterogeneous catalysts.

Heterogeneous catalysts with atomically dispersed metal atoms is usually referred to as a single-atom catalyst (SAC), terminology that was first introduced in 2011 describing the high CO oxidation activity of single Pt atoms dispersed on FeO_x,[125] shown in Figure 1.10. Single-atom catalysts (SACs) are free of organic ligands, and the controlled conversion of immobilized metallic complexes to SACs by removal of organic ligands has yet to be realized. SACs can exhibit distinct and often outstanding performance in many industrially important reaction including thermochemical, electrochemical and photochemical conversions. The SAC motif not only enables 100% atom utilization but has unique geometric and electronic properties coming from the absence of metal-metal bonds and the cationic nature of the isolated catalytic sites. Furthermore, SACs exhibit superior stability relative to their nanoparticle counterparts due to the formation of strong covalent bonds between the single metal site and the support.
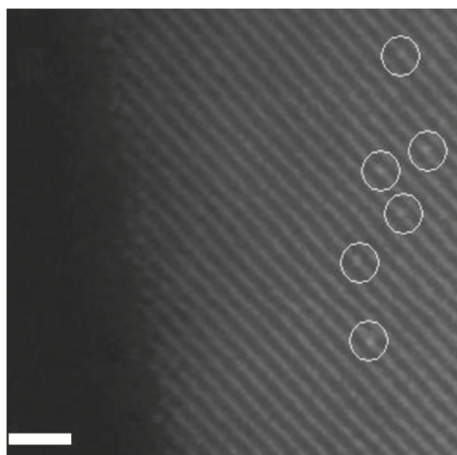
Figure 1.10: HAADF-STEM image of a 0.08% Pt╱FeO_x. Scale bar, 1nm.

Inspired by the nearly 100% utilization of metals in SACs and driven by the practical requirement for low-cost electrocatalysts, the application of SACs in electrochemical reactions is becoming an active research area. Although the thermocatalytic activity depends only on the nature and number of active sites, electrocatalytic and photocatalytic reaction additionally require a catalyst with high electrical conductivity or light absorbance, respectively. Rational design of these materials and investigation of their feasibility as OER catalysts is desirable for an intensive understanding of the more complex OER reaction mechanism. Well dispersed single atom Ir and Ir clusters on $Co(OH)_2$ nanosheets has been reported exhibiting good OER activity with rapid catalytic kinetics with an overpotential of 373 mV (10 mAcm^{-2}) significantly outperforming the commercial IrO_2 catalysts.[126]

Industrial applications demand a high coverage of single atoms on robust supports. If each metal atom is highly active, we then have desirable product yields per volume or mass of catalyst. Single atom catalyst can also be considered as the smallest building block to construct catalysts with structurally well-defined low nuclearity metal active centers, which may take the form of a so-called single-cluster catalyst (SCC)[127–129] such as dimer, trimer or larger metal cluster. These well defined SCC catalysts will likely contribute to sustainable chemical processes in the near future. The rapid development of single-atom catalysts in recent years suggest that it is not unreasonable to expect rapid access to robust SACs with higher stability, selectivity and activity for industrially important reactions.

1.5   State of the Art: RuO_2 for OER

RuO_2 is a conducting transition metal oxide that presents a rutile type structure as exclusively stable solid phase.[130,131] It has unique redox properties to be used as heterogeneous catalyst for oxidation reactions.[132–138] Moreover, it is an excellent material for eletrocatalysis due to its high conductivity.[139–143] A selected list of the oxidation reactions that RuO_2 is able to catalyze includes CO, NH_3 and methanol oxidations, water formation and the Deacon process in which Cl_2 is formed from

the oxidation of HCl.[144–146] In electrocatalysis, RuO_2 is used as anode in the chlor-alkali industrial process which forms Cl_2 and NaOH.[139,147] More recently, it has been shown to catalyze the hydrogen and the oxygen evolution reactions, which are key processes in the design of sustainable energy sources alternative to fossil fuels.[140–143]

The electrochemical processes involve solid-liquid (water) interfaces, which determines the nature of the active species.[130] The study of RuO_2-H_2O interaction is also relevant to understand the catalytic activity of hydrous RuO_2 (RuO_2-xH_2O)[148,149] as well as the origin of poisoning induced by water in the oxidation of CO.[150] Indeed, in the last decades, considerable efforts have been devoted to study water metal interfaces,[138,151–155] due to their relevance in many scientific fields such as catalysis, electrochemistry, corrosion, geology or atmospheric science.[156–159] For the particular case of RuO_2, the existing studies focus on the most stable (110) surfaces, which is characterized by the presence of unsaturated pentacoordinated ruthenium atoms Ru_{5C} and bridged oxygens O_{br}.

The water - oxide interface has been studied by using several spectroscopic techniques such as X-ray scattering measurements, High-resolution electron energy loss spectroscopy (HREELS) and thermal desorption (TDS). It has also been studied by means of scanning tunneling microscopy (STM)[160–164] and DFT calculations.[165–167] It is found that the interface nature highly depends on the experimental conditions, particularly on the applied voltage. Regarding studies without the addition of other species or external voltages Lobo and Conrad concluded, from HRELLS and TDS spectroscopies, that adsorption mainly involves non-dissociated water molecules.[160] These molecules are located at Ru_{5C} centers and establish hydrogen bond interactions with O_{br} oxygens.

Furthermore, water molecules desorb at around 400 K, which is consistent with a water adsorption energy of about -96 $kJ \cdot mol^{-1}$. Similar adsorption energies were obtained by means of DFT by Siahrostami and Vojvodic, although they suggested that H_2O on RuO_2 is prone to dissociate.[166] More recently, Dohnálek and co-workers combined STM microscopy and DFT calculations and analyzed

the effect of water coverage on the (110) surface.[155,163,164,168] They showed that at very low coverages, single water adsorbs on Ru_{5C} centers and that the Ru_{5C}-H_2O is in equilibrium with the deprotonated Ru_{5C}-OH$\cdots$H$-O_{br}$ species, as a result of the Lewis acidity of the ruthenium atoms. This study also shows that increasing the water coverage allows the formation of water dimers. The two water molecules of these dimers are adsorbed in contiguous Ru_{5C} centers and one of them is deprotonated, which leads to the formation of the $H_3O_2{}^-$ motif. At even higher water coverages, hydrogen bonded chains of water molecules are formed. These chains are characterized by the presence of the same $(H_3O_2{}^-)_n$ motif, which constitutes the fundamental building block. Computed adsorption energies per water molecule vary from -121 to -146 $kJ \cdot mol^{-1}$, depending on the amount of water and the degree of deprotonation.[162–164,166,167]

At this point it is worth noting that, to the best of our knowledge, the adsorption of water molecules at different surfaces, besides the most stable (110) one, has not been addressed. In this work, ambient pressure X-ray photoelectron spectroscopy and in situ surface diffraction measurements as well as density functional calculations are used to study different facets of RuO_2 interaction with water under humid and electrochemical conditions. This study identifies that crystallographic orientation is an important factor for water dissociation.[169]

1.5.1 Computational Oxygen Evolution Reaction

In an explicit thermochemical description of the OER, the overall rate depends on the free energy of the reaction steps involving catalyst bound intermediates. Since energies of the reaction steps depend on the nature of the catalyst, it is important to develop a fundamental understanding of these reactions on different materials.[170] Different surface structures, types of adsorbate and solvent effect can have a strong influence on the relative stability of the reaction intermediates. Then, the potential-determining steps and viable reaction paths can vary from one surface to another.

DFT calculations have allowed an explicit description of OER activity in terms of calculated adsorption energies. Through the *Sabatier principle*, it has been shown that OER activity is to a large extent determined by the binding strength of the reaction intermediates to the electrocatalyst surface. Depending on the number of different important surface intermediates many descriptors may be identified. For the OER at metal oxides surfaces the suggested intermediates are HO*, O* and HOO*.[171,172] In the literature, it has been shown that the binding energies of these three intermediates are strongly correlated. In general, the binding energies of the intermediates which bind to a surface through the same kind of atoms are found to scale linearly with each other as the electrocatalyst material is varied. To this point, schematic scaling relations between the binding energies of the OER intermediates and ΔG_{HO*} are presented. The slopes of these scaling relations are related to the number of bonds with the surface of each intermediate. For instance, the HO* and HOO* species both present a single oxygen bond to the surfaces and so, the slope of their scaling relation is one, while the slope of the scaling relation between the OH* and O* binding energies is two, as the O* intermediate is bonded by a double bond to the surface. Significantly, it has been found that ΔG_{OH*} and ΔG_{OOH*} are both related to each other by a constant of about 3.2 eV, Eq. 1.17.[173]

$$\Delta G_{HOO*} = \Delta G_{HO*} + 3.2\,eV \qquad (1.17)$$

This relationship[173,174] has been reported both for metals and for a wide range of oxide surfaces, which means that there is a general scaling relation between the HO* and HOO* intermediates regardless of the binding site. Taking this relationship in consideration, the energy of the second reaction step in the reaction pathway ΔG_2, has been proposed as a general chemical descriptor of oxygen evolving catalytic activity. It has been reported that the potential determining step (PDS) for the OER is the hydro-peroxide specie formation or the O-O bond formation step. Noting that the O* specie is enrolled in both steps, and taking into account the general scaling relation the equation (Eq. 1.18).

$$\Delta G_2 = \Delta G_{O^*} - \Delta G_{HO^*} - qV \tag{1.18}$$

It clearly contains the required chemical information on the binding energies for all three important OER intermediates. Indeed this chemical descriptor has been shown to be a good general parameter of the overpotential trends for a huge variety of oxides. In particular, allows for a comparison between different families of oxides using a single parameter.

Implications of these electrocatalyst optimization are significant. The ideal catalyst is defined by a free energy reaction diagram in which the four charge transfer steps have identical reaction free energies of 1.23 eV. This can only be achieved at a specific binding of all intermediates. However, due to scaling relations it is not possible to independently tune up the binding energy of each intermediate on a surface to get this optimal situation. Because, altering the binding energy of one intermediate will also change the binding energies of all other intermediates. Regardless of the binding energy of the O*, there is a constant difference between the binding energies of these species of 3.2 eV. This is considerably higher than the optimal separation of 2.46 eV, which would be expected for the transfer of two electrons and two protons.

While the identification of descriptors has been widely used by the calculation of adsorption energies, it is important to understand the relationship between this adsorption behavior and the fundamental properties of the catalytic material. Since the activation energies for elementary surface reaction are strongly correlated with adsorption energies, a good knowledge of the catalyst ability to form bonds is essential. In principle, the catalytic properties of a material are completely determined by its electronic structure. In the case of pure transition metals, the d-band approach provides a useful account of the ability of surface atoms to form bonds to an adsorbate, the higher in energy the d-state are relative to the metal Fermi level, the stronger the interaction with the adsorbate.[175–178] Arising from this, the d-band center is widely used as a descriptor for the activity of transition metals and their alloys. In the case of transition metal oxides, how-

ever, it is unclear whether such an interpretation can be realistically applied. The complexities of the oxide surface such as the configuration of the metal atoms and their ligands, the oxidation state of the metal and the nature of the interaction between the active site and the adsorbates, can all influence the adsorption energies. This success of d-band theory, motivates a molecular understanding of OER activity using the concepts of orbital occupancy and electron counting.[179]

The present thesis provides an exhaustive electronic study on the interaction of water molecules based on periodic boundary DFT calculations. We start from one molecule to a full monolayer coverage, on the main crystallographic orientations (110), (100), (011) and (001) of stoichiometric non-polar morphology. Other surfaces arising from the different pH conditions and the application of external voltages could be envisaged.[180] Moreover, Wulff construction approach has been used to build up RuO$_2$ stoichiometric nanoparticles to analyze how water adsorption is influenced by the nanoparticle shape and size. Results show that water coverage, surface morphology and temperature play an important role in the degree of water dissociation on the surface and nanoparticle shell, which is characterized by the formation of H$_3$O$_2{}^-$ "water dimer" units. Finally, their performance in the oxygen evolution reaction (OER) will be discussed, both surface and nanoparticles as a function of water coverage, facet orientation and nanoparticle size.

1.6   Objectives

In view of the difficulties that experimental characterization of such materials can face, not only by the requirement of expensive and sophisticated equipments, but also due to the ubiquity of water in our atmosphere, computational approaches can give significant insights.

With the ultimate goal to understand new efficient and durable water oxidation catalysts, the general objective of this thesis is to rationalize the nature of the most reactive heterogeneous catalyst RuO_2 through the interaction of the main crystallographic orientations with water. Furthermore, due to the high cost of the "noble metals" oxides and the significant increase of the reactivity, nanosized catalysts have gained more popularity than typical macroscopic heterogeneous catalysts. A comparison between the interaction of water with surfaces and nanoparticles as a function of structure, size and composition will be also discussed. In addition, the performance of such catalysts will be evaluated to identify the most reactive locations and conditions both in surfaces and nanoparticles.

The following specific goals have been established:

(i) Model and study the interaction between main crystallographic orientations of RuO_2 as a function of surface structure and water coverage.

(ii) Build realistic models of RuO_2 crystalline and stoichiometric metal oxide nanoparticles of different sizes and study their interaction with water as a function of topology, size, composition and thermal effects.

(iii) Identify the key factors on the interaction between the nanoparticle shell and water as solvent and reagent for the water oxidation reaction.

(iv) Analyze the catalytic and electrocatalytic capacity of both surface and nanoparticles in the performance of oxygen evolution reaction (OER).

(v) Analyze the structure of hybrid catalysts based on iridium single site species supported on a Indium Oxide (IO) surface and its performance in (OER).

Chapter 2

Theoretical Background

"The electron is a **theory** we use; it is so useful in understanding the way nature works that we can almost call it real"

Richard Feynman

Since physical properties of chemical systems arise from their electronic structure, there is no alternative but to employ quantum methodologies.

The ultimate goal of the quantum chemical approach is to approximate a solution to the time-independent, non-relativistic Schrödinger equation $\hat{H}\Psi = E\Psi$, where $\hat{H}$ is the Hamiltonian operator, Ψ the wave function which contains all the quantum information and E is the system energy as an eigenvalue.[181]

The Schrödinger equation can be simplified considering the significant difference between the masses of the nuclei and electrons. That is, it is possible to separate the electronic and nuclei motion, which is known as the *Born-Oppenheimer Approximation*.[182] This allows to solve the electronic Schrödinger equation for a given set of nuclear coordinates. The so-called electronic Hamiltonian of *N*

electrons and *m* nuclei is given by:

$$\hat{H}_{elec} = -\frac{1}{2}\sum_i^N \nabla_i^2 - \sum_A^m \sum_i^N \frac{Z_A}{r_{A,i}} + \sum_i^N \sum_{j>i}^N \frac{1}{r_{i,j}} + \sum_A^m \sum_{B>A}^m \frac{Z_A Z_B}{R_{A,B}} = \tag{2.1}$$

$$= \hat{T}_e + \hat{V}_{ne} + \hat{V}_{ee} + \hat{V}_{nn}$$

where $\hat{T}_e$ represents the electronic kinetic energy, $\hat{V}_{ne}$ the attractive potential between nuclei and electrons, $\hat{V}_{ee}$ the repulsive potential of the electron-electron interaction and finally $\hat{V}_{nn}$ the nuclei-nuclei potential. Redefining the general Schrödinger equation to the electronic expression for a given nuclear configuration, we get $\hat{H}_{elec}\Psi = E_{elec}\Psi$, where $\Psi(\vec{x_1}, \vec{x_2}, \cdots, \vec{x_N})$ is the N electrons wave function which depends on the electrons coordinates and E_{elec} is the energy value.

Electrons are indistinguishable *Fermi* particles with half-integral spin number $(S = \pm\frac{1}{2})$ that force Ψ to be *antisymmetric* with respect to the exchange of any electron pairs spin-orbitals. A direct consequence of this antisymmetry is the *Pauli exclusion principle* which states that two electrons can not have identical quantum numbers.

2.1   Wave Function Based Methods

The simplest method to obtain an approximate solution wavefunction is the Hartree-Fock method. In this case, the multielectronic wavefunction, which must be antisymmetric regarding the exchange of two electrons coordinates, is the *Slater Determinant* Φ_{SD}.

$$\Phi_{SD} = \frac{1}{\sqrt{N!}} \begin{vmatrix} \chi_1(1) & \chi_2(1) & \cdots & \chi_N(1) \\ \chi_1(2) & \chi_2(2) & \cdots & \chi_N(2) \\ \vdots & \vdots & \ddots & \vdots \\ \chi_1(N) & \chi_2(N) & \cdots & \chi_N(N) \end{vmatrix} \tag{2.2}$$

where χ_i are the single-electron wavefunctions composed by the product of a spatial orbital (ϕ) and a spin function (α or β), known as spin-orbitals.

According to the *variational principle*, which states that any approximate wave function will lead to an energy that is above the exact one, the methodology consists on minimizing the energy with respect to spin-orbitals.

Details on Hartree-Fock method are omitted, as a complete description of such technique can be found in literature.[183,184]

One of the most important limitations of the Hartree-Fock method is the fact that it does not describe the instantaneous electron-electron repulsion, introducing it as an average effect.

The addition of the electron correlation is accomplished by post Hartree-Fock methods,[185] based on expanding the wavefunction. Among these methods, the most relevant ones are the Configuration Interaction, the Many Body Perturbation Theory and the Coupled Cluster method. The principal advantage of these methods is that they allow a systematic improvement of the accuracy of the computational results. However, they are, generally, highly computational demanding and this makes them not suitable for large systems. Because we have not used these methods in this thesis, we will not discuss their formalism any further. Instead, in the next sections, we will describe density functional based methods, which also account for electron correlation, and are the ones used in the present work.

2.2 Density Function Theory (DFT)

The *Density Functional Theory* was born in 1964 when Kohn and Hohenberg provided the needed foundations of (DFT).[186] These foundations are related with the *probe of existence*, that the *ground state* electronic energy of our system can be completely determined by the *electron density* $\rho(\vec{r})$. The second theorem of Hohenberg-Kohn is the variational principle that provides an approach to achieve the exact density by minimizing the energy of the functional $E[\rho]$, reducing the problem to find its form.

For that, the Kohn-Sham (KS)[187] foundations, introduced in 1965, has been particularly successful. The idea was to redefine the kinetic energy functional, considering a non-interacting particles model, where the (KS) approach becomes similar to the (HF) method.

Within this orbital formulation, the *ground state* of a system is described as:

$$E[\rho(\vec{r})] = T_{ni}[\rho(\vec{r})] + V_{ne} + J_{ee} + [\Delta T + \Delta V_{ee}] \tag{2.3}$$

Where $T_{ni}[\rho(\vec{r})]$ is the kinetic energy calculated for a *non-interacting* electron system using a Slater determinant, V_{ne} is the classical nuclear-electron attraction, J_{ee} is the classical electron-electron repulsion, ΔT is a kinetic correction from the electron interacting nature and ΔV_{ee} includes all non-classical corrections to the electron-electron repulsion energy. The last term, in brackets, is called exchange-correlation functional $E_{xc}[\rho(\vec{r})]$ commonly splitted into two parts, E_x as a pure exchange term and a correlation part E_c, which is related to the different scaling properties of the *exchange and correlation holes*.

$$E_{xc}[\rho] = E_x[\rho] + E_c[\rho] = \int \rho(r)\varepsilon_x[\rho(r)]dr + \int \rho(r)\varepsilon_c[\rho(r)]dr \tag{2.4}$$

The main feature of the Kohn-Sham theory is that it only needs to approximate the exchange-correlation energy functional $E_{xc}[\rho(\vec{r})]$ instead of the Hogenberg-Kohn approach, which needs to approximate the kinetic and exchange functionals including the correlation.

2.2.1 Exchange-Correlation Functionals

As explained before, the exchange-correlation functional $E_{xc}[\rho(\vec{r})]$ is not only the difference between the classical and quantum electron-electron repulsion, it also includes the kinetic energy differences between the imaginary *non-interacting* system and the real one. Besides, in some cases, empirical parameters are necessarily included to add some corrections to the kinetic energy based on experimental data.

Moreover, the quality of the exchange-correlation functionals needs to be validated by experiments or with high-level wave function based methodologies. This kind of calibration only relates the quality of such functional for the chosen system. Finding the best functional depends on the system and properties, for example, molecular or periodic systems (solids), and also electronic excitations or NMR chemical shifts properties.

Local Density Approximations

The *Local Density Approximation* (LDA) assumes that the functional depends only on local values of the density, based in the uniform electron gas. The exchange-correlation $E_{xc}[\rho] = E_x[\rho] + E_c[\rho]$ is a simple functional which depends on ρ at a specific point in the space. The LDA approach has a poor performance for discrete systems like molecules, being suitable for systems with low density variations. The extension of the LDA to the spin-polarized case L(S)DA is based on the spin interpolation $E_{xc}^{L(S)DA}[n\uparrow, n\downarrow]$ proposed by Vosko, Wilk and Nusair.[188] It is well known that the LDA tends to overestimate the bond strength in solids providing too small lattice parameters, overestimates cohesive energies and underestimates band gaps in semiconductors and insulators.

Generalized Gradient Approximation

Electron density is typically far from spatially uniform, which is a good reason to believe that the LDA approach will have limitations. One way to improve the correlation function is to make it depend not only on the local value of the density, but on the extent to which the density is locally changing, for instance, the gradient of the density. Including a gradient correction defines the so-called *Generalized Gradient Approximation*.

Most of gradient corrected functionals are constructed with the correction being a term added to the LDA functional, i.e:

$$\epsilon_{XC}^{GGA}[\rho(r)] = \epsilon_{XC}^{LSD}[\rho(r)] + \Delta\epsilon_{XC}[\frac{|\Delta\rho(r)|}{\rho^{4/3}(r)}] \tag{2.5}$$

The first widely popular GGA exchange functional was developed by Becke.[189] This functional adopts a mathematical from that has a correct asymptotic behavior at long range for the energy density, and it further incorporates a single empirical parameter, the value of which was optimized by fitting to the exactly known exchange energies of the six noble gas atoms. Other exchange functionals similar to the Becke's example have appeared, such as CAM, FT97, O, PW, *m*PW, and X, where X is a particular combination of B and PW found to give improved performance over either.

Alternative GGA exchange functionals have been also developed based on rational function expansions of the reduced gradient.[190] These functionals, which contain no empirically optimized parameters, include B86, LG, P, PBE and *m*PBE.

Corrections to the correlation energy density include functionals B88, P86 and PW91 which uses a different expression than for the LDA correlation energy density without empirical parameters. Another popular GGA correlation functional like LYP does not correct the LDA expression but instead computes the correlation energy as a whole. Among all the correlation functionals discussed, LYP is only one that provides and exact cancellation of the self-interaction error in one-electron systems.

meta-GGA

The extension of GGA methods is to allow the exchange and correlation functionals to depend on higher order derivatives of the electron density, with the Laplacian ($\nabla^2 \rho$) being the second-order term. Alternatively, the functional can be taken to depend on the orbital kinetic energy density. Inclusion of the Laplacian or orbital kinetic energy density as a variable leads to the so-called *meta*-GGA functionals. Calculation of the orbital kinetic energy density is numerically more stable than calculation of the Laplacian of the density.[191]

One of the earlies attempts to include kinetic energy functionals was done by Becke and Roussel (BR). Various *meta*-GGA functionals for exchange, correlation or both have been developed including B95, B98, ISM, KCIS, PKZB, τHCTH,

TPSS and VSXC. The cost of an *meta*-GGA calculation is entirely comparable to that for a GGA calculation, and the former is typically more accurate than the latter for a pure density functional. Finally, we must consider at least one additional wrinkle in functional design, namely, the inclusion the HF exchange.

Hybrid Functionals

The Adiabatic Connection Formula (ACF) provides a link between a fictitious reference system with non-interacting electrons and the actual fully interacting system. If it is assumable that the wave function of the non-interacting system is a Slater Determinant composed of Kohn-Sham orbitals, the exchange energy is exactly that given by Hartree-Fock theory calculated by HF wave mechanics methods, which is the exact exchange energy. Within this approximation, some models that includes in the formula the exact exchange are so-called *Hybrid* methods.[192] One of the most popular DFT functionals belongs to this kind: B3LYP.

$$E_{XC}^{B3LYP} = (1-a)E_X^{LSDA} + aE_X^{exact} + b\Delta E_x^{B88} + a_c E_C^{LYP} + (1-c)E_C^{LSDA} \quad (2.6)$$

The a,b and c parameters are determined by fitting to experimental data and depend on the chosen forms for E_x^{GGA} and E_c^{GGA}, with typical values being 0.2, 0.7 and 0.8, respectively.

Likewise, for instance, the PBE0 functional consists in the addition of exact exchange with a mixing that is 25% of exact HF exchange and 75 % of PBE exchange as shown in the following equation.[193]

$$E_{xc}^{PBE0} = 0.25E_x^{HF} + 0.75E_x^{PBE} + E_c^{PBE} \quad (2.7)$$

Inclusion of exact HF exchange is often found to improve the calculated results, although the optimum fraction to include depends on the specific property of interest. The improvement of new functionals by inclusion of a suitable fraction of exact exchange is now a standard feature. At least part of the improvement

may arise from reducing the self-interaction error since HF theory is completely self-interaction free.

2.2.2   Empirical Dispersion (DFT+D)

A general drawback of all common GGA functionals, including hybrids, that replace part of the local by nonlocal HF exchange, is that they can not describe long-range electron correlations that are responsible for van der Waals (vdW) dispersive forces. The vdW interaction between atoms and molecules play an important role in many chemical systems. The most widely applied method to include dispersive forces and very well tested is the DFT-D method.[194]

In DFT-D method introduces the total energy is given by:

$$E_{DFT-D} = E_{DFT} + E_{disp} \tag{2.8}$$

where the E_{DFT} is the usual self-consistent Kohn-Sham energy and E_{disp} is an empirical dispersion correction expressed as follows.

$$E_{disp} = -S_6 \sum_{i=1}^{N_{at}-1} \sum_{j=i+1}^{N_{at}} \frac{C_6^{ij}}{R_6^{ij}} f_{dmp}(R_{ij}) \tag{2.9}$$

Into that expression, N_{at} is the number of atoms, C_6^{ij} is the dispersion coefficient for atom par ij, S_6 is the global scaling factor that depends on the chosen DFT functional used and R_{ij} is the inter-atomic distance. A damping function f_{dmp} is introduced in order to avoid fictitious interactions due to small distances, which is given by

$$f_{dmp}(R_{ij}) = \frac{1}{1 + e^{-d(R_{ij}/R_r - 1)}} \tag{2.10}$$

where R_r is the sum of atom vdW radii. C_6 coefficients are parametrized based on calculations of atomic ionization potentials I_p and static dipole polarizabilities α and derived from the London dispersion formula.

$$C_6 = 0.05 \cdot N \cdot I_p \cdot \alpha \tag{2.11}$$

As a result, the present correction replace part of the non-local electron correlation effect at long and medium range in a conventional gradient corrected density functional by the $C_6 \cdot R^{-6}$ term. In the literature it is shown how the introduction of dispersive forces works in realistic chemical applications reach results in an improved accuracy compared with the standard GGA methods.

2.3 Ab-Initio Simulation of Solids

This section introduces how DFT can be used to predict important physical properties of solids. Crystalline solids may be described as *ordered repetitions* of atoms or group of atoms in three dimensions, with an infinite number of them. Because of that huge amount of atoms, a reliable *ab-initio* DFT treatment of the system seems to be an unaffordable task. However, crystals are structures with translational periodicity governed by the geometry[195,196] of a *repeating motif*.

2.3.1 Lattice Structure

Considering an ideal crystal, all repeating units are identical, which means that they are related by translational symmetry operations, corresponding to the set of vectors:

$$T_{(u,v,w)} = u\vec{a} + v\vec{b} + w\vec{c} \tag{2.12}$$

Where u, v and w are three integers from $-\infty$ to ∞, and $\vec{a}$, $\vec{b}$, $\vec{c}$ are non-coplanar vectors defining the basis of a three dimensional space. The set of points generated through all the translation vectors $T_{(u,v,w)}$ forms a three-dimensional lattice where the points are called *lattice nodes*.

The given integers u, v and w define a given vector, which provides the corresponding coordinates of the node in the reference system already defined by $\vec{a}$, $\vec{b}$ and $\vec{c}$. The final parallelepiped defined by the three basis vectors is called *unit cell*. The lattice constants are the three module a, b, c and three angles α, β, γ between the vectors, as shown in the following figure. Several unit cells can be defined, where the smallest one is the so-called *primitive cell*.
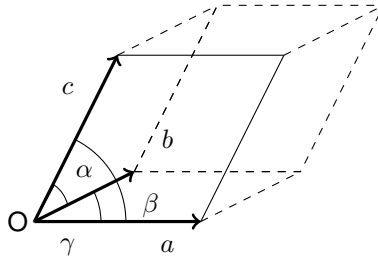
Figure 2.1: Unit cell lattice constants (a,b,c) and (α, β, γ)

The periodic repetition of the "*motif*" inside the unit cell by an infinite set of vectors yields the *crystal structure*, which is set by the lattice constants and the coordinates (x,y,z) of all atoms in the unit cell. These coordinates are the components of the vectors:

$$r_i = x_i a + y_i b + z_i c \quad (i = 1, 2 \cdots N) \tag{2.13}$$

Expressing the atoms coordinates as fractions of the unit cell in each of the three directions (a,b,c) separated by the angles (α,β,γ) we set the so-called *fractional coordinates*.

$$x_{frac} = {x'}/{a} \quad y_{frac} = {y'}/{b} \quad z_{frac} = {z'}/{c} \tag{2.14}$$

The reciprocal lattice is defined by three vectors a', b' and c' derived from the a, b and c vectors of the direct cell.

$$a' = 2\pi \frac{b \times c}{L^3} \quad b' = 2\pi \frac{c \times a}{L^3} \quad c' = 2\pi \frac{a \times b}{L^3} \tag{2.15}$$

The reciprocal cell of a cubic cell with side length L is also a cube, with the side length $2\pi/L$. The equivalent of a unit cell in reciprocal space is called the first *Brillouin Zone*.

2.3.2 Space Groups

In crystals a lot of symmetry operations may coexist, considering only the oper-
ations which do not imply translations we get the so-called *point groups* since
the operator form a mathematical group and leave one point fixed (rotations). In
three dimensions, there are 32 possible crystallographic point groups. Then, it
is convenient to group together the symmetry classes with common lattice fea-
tures which are described by unit cells of the same type, seven different groups
may be identified (triclinic, monoclinic, orthorhombic, tetragonal, rhombohedral,
hexagonal and cubic) known as the *seven crystal systems*.

Each crystal system can be associated with a primitive cell compatible with the
point groups that belong to that system. These primitive cells define a lattice
type, but there are other types of lattices not based on the primitive cells. Overall,
there are 14 possible space lattices, that are called *Bravais lattices* listed in 1850.
For example, the tetragonal crystal system has two bravais lattice, the simple
tetragonal and the body-centered tetragonal lattice, as shown in the following
figure.
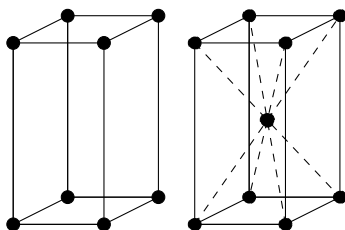
Figure 2.2: Bravais Lattices of the tetragonal crystal system

Space groups in three dimensions are made from the combination of the 32
crystallographic point groups with 14 Bravais lattices, each of them belonging to
one of the 7 lattice systems, as a result the total number of possible combinations
leads to 230 different *crystallographic space groups*. As a consequence of the
presence of symmetry elements, symmetry-equivalent atoms or molecules will
share the unit cell space.

The smallest part of the unit cell is called the *asymmetric unit*, which is able to generate the whole cell contents when the symmetry operations of the space group are applied to them.

2.3.3   Crystallographic Planes

Crystalline solids are anisotropic being necessary to identify in a simple way *planes* in which specific physical properties can be observed. Crystal faces can thus be described by means of three indices that are whole numbers, and these, in fact, are always small whole numbers for naturally growing crystals. These three integers describing the orientation perpendicular to a plane are called *Miller indices*, and the symbols *h*, *k* and *l* are used for them. We will restrict ourselves to planes where the indices of which are relatively prime numbers; that is, the indices have no common factors. Such restriction is logical in classical crystallography, since only the orientation of a crystal face has significance, and not how far it is from some arbitrarily defined origin.

Without loss of generality, the plane (*hkl*) can be described by the equation:

$$hx + ky + lz = 1 \qquad\qquad (2.16)$$

This equation has solutions where x, y and z are integers, e.g., the following equation:

$$21x + 10y + 6z = 1 \qquad\qquad (2.17)$$

It is satisfied by such points as (1,-2,0) or (3,-5,-2); that is, these points lie on the place (21, 10, 6). However, points for which the coordinates are integers are lattice points. Therefore, every plane (*hkl*) passes through a set of lattice points. Since all lattice points are identical, planes identical in all respects, including orientation, must pass through all lattice points.

Crystallographic planes parallel to faces of the unit cell are of type $(h, 0, 0)$, $(0, k, 0)$ and $(0, 0, l)$. Other planes such as the (111) shown in Figure 2.3 can also be defined.
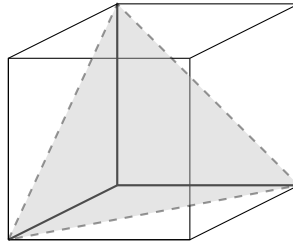
Figure 2.3: Crystallographic plane (1 1 1) into a unit cell

2.3.4 Periodic Boundary Conditions and Bloch's Theorem

It is assumed that a crystalline solid is an infinite system (Figure 2.4), made of macroscopic finite crystals containing $N = N_1 \cdot N_2 \cdot N_3$ cells, whose sides are $N_j a_j$.
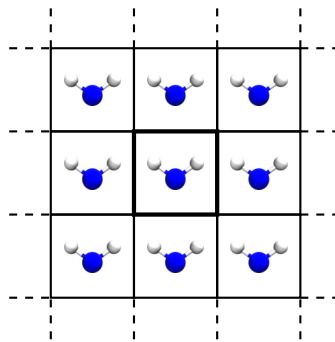
Figure 2.4: Periodic Boundary condion of a water molecule in a cell.

The finite crystal is part of an infinite system, which is delimited in a formal way, where the wavefunction obeys the following *Born-Von Karman* periodic boundary conditions.[197]

$$\psi_{i,k}(r + N_j a_j) = \psi_{i,k}(r) \tag{2.18}$$

where $\psi_{i,k}$ must satisfy the Bloch theorem:

$$\psi_{i,k}(r + N_j a_j) = \psi_{i,k}(r) = e^{(iN_j k \cdot a_j)} = 1 \tag{2.19}$$

The previous expression can be rewritten with the reciprocal lattice vector (a', b', c'), which results directly from the direct lattice and satisfy the relation $a_i \cdot b_j = 2\pi \cdot \delta_{ik}$:

$$e^{(2\pi i N_j k_j)} = 1 \tag{2.20}$$

Where $k_j = n_j/N_j$, and n_j is any integer $0 \leq n_j \leq N_j$. In periodic boundary conditions the general k vector inside the *Brillouin Zone* is defined as:

$$k = \frac{n_1}{N_1}a' + \frac{n_2}{N_2}b' + \frac{n_3}{N_3}c' \tag{2.21}$$

Each k point can be associated with a parallelepiped of volume v_k

$$v_k = (\frac{a'}{N_1}) \times (\frac{b'}{N_2}) \times (\frac{c'}{N_3}) = \frac{V_{BZ}}{N} \tag{2.22}$$

where V_{BZ} is the volume of the *Brillouin Zone* and N is the number of unit cells in the macroscopic finite crystal. For increasing values of N, the volume v_k progressively decreases, which means that the k-points get progressively closer until they cover the entire *Brillouin Zone* volume as a continuous variable, for N approaching infinite.

The correlated nature of the electrons within a solid is not the only obstacle to solving the Schrödinger equation for condensed matter systems: for solids, one must also bear in mind the effectively infinite number of electrons within the solid. One may appeal to *Bloch's Theorem*[198] in order to solve this problem. Instead of being required to consider an infinite number of electrons, it is only necessary to consider the number of electrons within the *unit cell*

2.4   Basis Sets

One of the essential approximations of all *ab initio* methods is the introduction of a *basis set*. Expanding the molecular orbitals in a set of known functions is not an approximation if the basis set is *complete*. A complete basis set means using an *infinite* number of functions, which is impossible. Then a *finite* basis set must

be used, but taking into account that the smaller basis set will provide a poorer electronic representation. The type of basis functions used also influences the accuracy.

Modern electronic structure methods can be classified into two classes, depending on the choice of the basis set: localized basis functions with Gaussian-type orbitals (GTOs) and plane wave methods.

2.4.1 Gaussian-Type Orbitals

For non-periodic systems, such as molecules, Gaussian type functions are the natural choice, because they give a reasonable description of the physics of the system and their integration is computationally easy. The generic molecular orbital can thus be expressed as $\phi_i = \sum_\alpha^M c_{\alpha,i} \chi_\alpha$, where χ_α is an *atomic orbital*. There are two types of atom-centered basis functions commonly used in electronic structure calculations: Slater Type Orbitals (STO)[199] and Gaussian Type Orbitals (GTO).[200] Slater type orbitals have the functional form as:

$$\chi(r, \theta, \varphi) = NY_{l,m}(\theta, \varphi)r^{n-1}e^{-\zeta r} \tag{2.23}$$

However, resolution of the bielectronic integrals is easier using Gaussian functions (GTOs):

$$\chi(r, \theta, \varphi) = NY_{l,m}(\theta, \varphi)r^{2n-2-l}e^{-\zeta r^2} \tag{2.24}$$

Where, N is a numerical factor to *normalize* the function to unity and l, m, n are integers that characterize the type and order of the Gaussian function.

2.4.2 Plane waves

Plane waves[201] represent another common choice of basis functions, particularly in solid-state simulations. They are periodic functions that can be written in

terms of complex exponentials or sine-cosine functions. For instance, for the free electron in one dimension:

$$\phi(x) = Ae^{ikx} + Be^{-ikx}$$
$$\phi(x) = A\cos(kx) + B\sin(kx)$$

(2.25)

For infinite systems, the molecular orbitals coalesce into *bands*. The electrons in a band can be described by orbitals expanded in a basis set of *plane waves*, which in three dimensions can be written as a complex function:

$$\chi_k(\vec{r}) = e^{ik\cdot r}$$

(2.26)

Regarding Bloch's theorem[198] with plane waves basis functions the wavefunction of an electron within a perfectly periodic potential may be written as:

$$\psi_{i,k}(r) = u_i(r)e^{ik\cdot r}$$

(2.27)

where $u_i(r)$ is a function that adds the periodicity of the potential as $u_i(r+l) = u_i(r)$, where l is the length of the unit cell; k is a wavevector confined to the first *Brillouin Zone*. Since $u_j(r)$ is a periodic function, we may expand it in terms of a Fourier series:

$$u_i = \sum_G c_{i,G} e^{iG\cdot r}$$

(2.28)

where G are the *reciprocal lattice* vectors defined through $G\cdot R = 2\pi m$, where m is an integer; R is a real space lattice vector and the $c_{i,G}$ are the plane wave expansion coefficients. The electron wavefunctions may therefore be written as a linear combination of plane waves so-called *Bloch functions*.

$$\psi_{i,k}(r) = \sum_G c_{i,k+G} e^{i(k+G)\cdot r}$$

(2.29)

In principle, the series in the previous equation should be infinite, but in practice the series should be truncated in order that it may be handled computationally. The coefficient for the plane waves have a kinetic energy $\frac{\hbar^2}{2m} \mid k+G \mid^2$, and plane waves with high kinetic energy are less important than those of low kinetic energy.

Then, a kinetic *energy cut-off* E_{cut} has to be introduced in order to achieve a finite basis set. The kinetic energy cut-off is defined through:

$$E_{cut} = \frac{\hbar^2}{2m} \mid k + G \mid^2 \tag{2.30}$$

fixing the highest reciprocal lattice vector G used in the plane wave expansion, resulting in a finite basis set. A typical energy cutoff of 200 eV on a cubic unit cell of $a = 15\text{Å}$ corresponds to a basis set with $20.0 \cdot 10^3$ functions. Plane wave basis sets tend to be significantly larger than the typical Gaussian-type basis sets. Furthermore, basis-set superposition errors that have to be carefully controlled in calculations based on local basis sets are avoided with plane wave functions.

They are the best choice for describing delocalized slowly varying electron densities, such as the valence and conduction bands in metals. The core electrons are strongly localized around the nuclei, which means that to describe them adequately a large number of plane wave basis is needed. The nuclei-electron potential is furthermore impossible to be described in a plane wave basis, and this type of basis set is often used in connection with *pseudopotentials* for smearing the nuclear charge and model the effect of the core electrons.

2.4.3 Pseudopotentials

Chemical systems involving atoms from the lower part of the periodic table present a large number of core electrons. Moreover, the discussion above points to the fact that large energy cutoffs must be used. The most important approach to reduce the computational cost due to core electrons is to use *pseudopotentials*.

Conceptually, a pseudopotential replaces the electron density from a chosen set of core electrons with a smoothed density that matches various important physical and mathematical properties of the true ion core. Ideally, a pseudopotential is developed by considering an isolated atom of one element, but the resulting pseudopotential can then be used reliably for calculations that place this atom in any chemical environment without further adjustment of the pseudopotential.[202]

Projector Augmented Wave (PAW) Method

The *projector-augmented wave* (PAW)[203] was introduced by Blöchl to achieve simultaneously the efficiency of *pseudopotentials* method and the accuracy of the full-potential linearized augmented-plane-wave (FLAPW) method, commonly used as benchmark for DFT calculations on solids. The (PAW) method accounts for the nodal features of the valence orbitals and ensures the orthogonality between valence and core wave functions instead of the pure pseudo-potential approach.

The (PAW) wave function is represented as a valence term expanded in a plane-wave basis adding the contribution from the region within the core radius of each nucleus, evaluated on a grid. The contribution from a core region is expanded as a difference between two sets of densities, one arising from the all-electron atomic orbitals, the other from a set of nodeless pseudo-atomic orbitals, allowing the wave function within the core region to adjust for different environments.

2.5   Potential Energy Surface Exploration

The main part of this thesis is based on calculations to explore the *Potential Energy Surface* (PES)[184] of the specific paths related to the reactivity of water oxidation reaction onto metal oxide surfaces and nanoparticles. An exploration of a PES is based on the concept of the Born-Oppenheimer approximation, discussed at the beginning of this chapter, which states that nuclei are fixed and the Schrödinger equation is solved for that particular configuration. Different arrangements of the nuclei may be adopted so that the set of solutions obtained composes the Potential Surface Energy of a polyatomic systems. The PES is a hypersurface defined by the potential energy of a collection of atoms over all possible atomic arrangements.
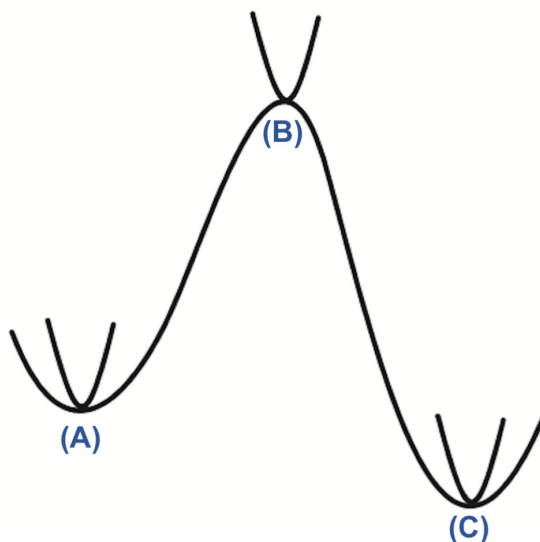
Figure 2.5: Schematic illustration of a Potential Energy Surface (PES).

Interestingly, stationary points in a PES are those points where all the forces vanish. In Figure 2.5 the points labeled with A,B and C are stationary, but they are not of the same kind. To distinguish the types of stationary points, it is necessary to consider the second derivatives of the energy with respect to the nuclear coordinates.

Second derivatives quantities comprise the Hessian matrix. For a minimum of the potential energy surface **(A)** all the eigenvalues of the Hessian matrix are positive. In contrast, a maximum of a potential energy surface is characterized by the eigenvalues of the Hessian matrix all being negative. First order saddle points (**B**) are characterized by one negative eigenvalue, whereas all the other are positive. They are associated with the chemical concept of transition state; that is, the minimum energy that has to be overcome in order to go from one minimum to another. The minima of the PES can represent, for instance, reactants, products or intermediates of a given reaction.

2.5.1   Optimization Algorithm

DFT minimizations look for a chemical system fully relaxed both in electronic and structure terms. Then, after each electronic relaxation, the forces acting on each atom are calculated and used to determine a new geometry. This outer loop, the ionic minimization, includes relaxation of the atomic positions and/ or the unit cell shape in solid computational chemistry.

The system will reach the minimum-energy configuration at which the forces at each atom vanish close to zero (0.01 - 0.05 $eV/\text{\AA}$) as stated by the Hellmann-Feynman theorem.[204]

A common implemented ionic minimization algorithm is the *conjugate gradient* (CG).[205,206] The conjugate gradient (CG) method is an improved approach of the previous developed *step descent* methodology. The step descent method uses a gradient vector g with points in the direction where the function increases the most; that is, the function that can always be lowered by *stepping* in the opposite direction $d = -g$. Unfortunately, as the minimum is approached, the rate of convergence slows down, actually will never reach the minimum crawling toward it at an ever decreasing speed. The *Conjugate Gradient* method tries to improve on this by performing each line search no along the current gradient but along a line that is constructed such that is *conjugate* to the previous search directions. The first step is equivalent to a steepest descent step, but subsequent searches are performed along a line formed as a mixture of the current negative gradient and the previous search direction:

$$d_i = -g_i + \beta_i d_{i-1} \tag{2.31}$$

The Conjugate Gradient method has a much better convergence behavior than the steepest descent one, but it requires more storage because two current gradients and previous directions vectors must be stored.

2.5.2   Transition State Searching

Locating minimal energy geometries is fairly easy, but finding first order saddle points *Transition States* (TS) is much more difficult. Many different strategies have been proposed, which can be divided into two general categories, those based on *Interpolation* between two minima and those using only *local* information. Interpolation methods assume that the reactant and product geometries are known and that a TS is located somewhere between these two end-points. On the contrary, local methods propagate the geometry using only information about the function and its first and also second derivate at the current point, where previous knowledge of reactants and product geometries are no required.

Nudged Elastic Band (NEB) Method

Nudged Elastic Band (NEB)[207] Method is classified as *Multistructure Interpolation* method, which operates with multiple structures or *images* connecting the reactant and product minima geometries. The relaxation of the images will, in favorable cases, not only lead to the saddle point but also the approximation of the whole reaction path. The initial path "guess" of structures is typically build along a straight line connecting the reactants and products, but may also involve one or more intermediate geometries to guide the search in a certain direction.

NEB method defines a target function so-called *"elastic band"* (T_{NEB}) Eq.(2.32) as the sum of energies of all images. T_{NEB} attempts to distribute all the interpolated images along the path by adding a penalty term as spring constant k. Once defined, T_{NEB} it is minimized in order to reach the minimum energy path (MEP).

$$T_{NEB}(R, x_1, x_2, x_3, \cdots, x_M, P) = \sum_{i=1}^{M} E(x_i) + \sum_{i=1}^{M-1} \frac{1}{2}k(x_{i+1} - x_i)^2 \qquad (2.32)$$

An improved feature is to allow on the images move along the elastic band to became the exact saddle point, called *Climbing-Image* (CI-NEB).[208]

2.6 Solvation Models

An important aspect of computational chemistry is to evaluate the effect of environment, such as a solvent. Methods for evaluating the solvent effect may broadly be divided into two types: those describing the individual solvent molecules and those that treat the solvent as continuous medium.[209]

Continuum solvation models consider the solvent as a uniform polarizable medium with a dielectric constant of ϵ, and with the solute placed in a suitable shaped hole in the medium. Create the hole in the medium costs energy, while dispersion interactions between the solvent and solute add a stabilization contribution. The electric charge distribution of the solute polarizes the medium, which in turn acts back on the system, thereby producing an electrostatic stabilization. The solvation free energy may be written as follows:

$$\Delta G_{solvation} = \Delta G_{cavity} + \Delta G_{dispersion} + \Delta G_{elec} \qquad (2.33)$$

The energy required to create a cavity, and the stabilization due to vdW interactions between the solute and solvent is usually assumed to be proportional to the surface area. The corresponding energy terms may be taken simply as being proportional to the total *Solvent Accessible Surface* (SAS) area.

$$\Delta G_{cavity} + \Delta G_{dispersion} = \alpha SAS + \beta \qquad (2.34)$$

The electrostatic component can be described at several different levels of approximation. In our case, the *Poisson* equation[210] is used as a second-order differential equation describing the connection between the electrostatic potential ϕ, the charge distribution ρ and the dielectric constant ϵ.

$$\nabla \cdot (\epsilon(r)\nabla\phi(r)) = -4\pi\rho(r) \qquad (2.35)$$

2.7 Thermochemical Corrections

The majority of chemical research does not concern discrete systems, but instead macroscopic quantities of matter governed by laws of thermodynamics.[211] The connection between the microscopic energy obtained from electronic calculations and the macroscopic values that can be measured in the laboratory is provided by *Statistical thermodynamics*, by formulations used to obtain zero-point energy, entropy, free energy, enthalpy and so on. The fundamental function that characterizes statistical thermodynamics is the *partition function*. Using the canonical ensemble which is for a constant number of particles N, volume V and temperature T is written as:

$$Q(N, V, T) = \sum_i e^{-E_i(N,V)/k_b T} \tag{2.36}$$

where i runs over all possible energy states of the system with energy E_i and k_B is the Boltzmann's constant. For the canonical ensemble and using established thermodynamic definitions, the following is true:

$$U = k_B T^2 \left(\frac{\partial lnQ}{\partial T}\right)_{N,V}$$
$$H = U + PV$$
$$S = k_B lnQ + k_B T \left(\frac{\partial lnQ}{\partial T}\right)_{N,V} \tag{2.37}$$
$$G = H - TS$$

The determination of the energy of the different states of the system is obtained through two main approximations. First, it is assumed that the ensemble is an ideal gas in which molecules do not interact and E_i is the summation of the energies of each molecule of the system. Moreover, it is assumed that the molecule energy can be expressed as the sum of translation, rotational, electronic and vibrational energy. Assuming the ideal gas and rigid-rotor approximation it is possible to determine the two first terms. Electronic energy is obtained with regular

electronic calculations. Finally, the vibrational energy can be provided through a vibrational frequency calculation using the harmonic oscillator approximation.

2.8   Ab Initio Molecular Dynamics (AIMD)

The molecular dynamics method[212,213] can be classified into two main general forms: one for systems at equilibrium, and another one for systems away from equilibrium. Equilibrium molecular dynamics is typically applied to an isolated system containing a fixed number of molecules N, in a fixed volume V and, because of the isolated feature of the system, the total energy E is also constant. Here the total energy E is the sum of the molecular kinetic and potential energies. Then, the variables N, V and E determine the thermodynamic state.

An NVE-molecular dynamics, the atom positions r^N are obtained by solving Newton's equations of motion:

$$F_i(t) = m\ddot{r}_i(t) = -\frac{\partial U(r^N)}{\partial r_i} \tag{2.38}$$

Where F_i is the force on i caused by the $N-1$ other molecules, the dots indicate total time derivatives, and m is the molecular mass. The previous equation relates the force with the intermolecular potential energy. Integration once yields the atomic momenta, and twice gives the atomic positions.

Integration for several thousand times produces individual atomic trajectories from which time average $\langle A \rangle$ can be computed to set macroscopic properties.

$$\langle A \rangle = \lim_{t \to \infty} \frac{1}{t} \int_{t_0}^{t_0+t} A(\tau) d\tau = \lim_{M \to \infty} \frac{1}{M} \sum_{i=1}^{M} A_i \tag{2.39}$$

At equilibrium this average cannot depend on the initial time t_0. Since positions and momenta are obtained, the time average represents both static properties, such as thermodynamics and dynamics properties, such as transport coefficients. This is based on the *ergodic hypothesis*, which makes the assumption that the average obtained by following a small number of particles over a long time is equivalent to averaging over a large number of particles for a short time. This

implies that a time average over a single particle is equivalent to an average of a large number of particles at any given time snapshot.

The motion's equation is usually calculated with the *Verlet algorithm*, which gives accurate approximation of the atomic trajectories if the Δt is small. Another way to approach the dynamical problem is by means of the *Lagrangian*, where the equation of motion for each coordinate can be expressed in terms of:

$$\frac{d}{dt}\left(\frac{\partial L}{\partial v_i}\right) = \frac{\partial L}{\partial r_i} \tag{2.40}$$

The atomic motions in *Microcanonical* environment are related to the temperature, which means that in a system in equilibrium at temperature T, the velocities follow a Maxwell-Boltzmann distribution. In the NVE-type simulations, the temperature and pressure will fluctuate. The total energy can be calculated from the positions and velocities, as follows.

$$E_{tot} = \sum_{i=1}^{N} \frac{1}{2}m_i v_i^2 + V(r) \tag{2.41}$$

The temperature of the system is proportional to the average kinetic energy:

$$\langle E_K \rangle = \frac{1}{2}(3N_{atoms} - N_{constraints})kT \tag{2.42}$$

Since the kinetic energy is the difference between the total energy and the potential energy, E_k will vary significantly, and the temperature will be calculated as an average value with an associated fluctuation.

On the other hand, it is possible also to generate NVT or NPT ensembles by MD techniques by modifying the velocities or positions in each time step. The instant value of the temperature is given by the average of the kinetic energy, as indicated above. If this is different from the desired temperature, all velocities can be scaled by a factor of $(T_{desired}/T_{actual})^{1/2}$ in each time step to achieve the desired temperature. The system may be coupled to a *heat bath*, which gradually adds or removes energy to the system with a suitable time constant, this procedure is called *thermostat*. The kinetic energy of the system is again modified by scaling the velocities, but the rate of heat transfer is controlled by a coupling parameter τ.

$$\frac{dT}{dt} = \frac{1}{\tau}(T_{desired} - T_{actual}) \tag{2.43}$$

The most common *heat bath*, considered as a true *canonical ensemble*, is the so-called Nosé-Hoover method, where the heat bath is considered an integral part of the system and assigned dynamic variables, which are evolved on an equal footing with the other variables.

The pressure can similarly be held constant by coupling to a *pressure bath*. Instead of changing the velocities of the particles, the volume of the system is changed by scaling all coordinates according to the following equation.

$$\frac{dP}{dt} = \frac{1}{\tau}(P_{desired} - P_{actual}) \tag{2.44}$$

These *barostat* methods are again widely used in molecular dynamics, but do not produce strictly correct ensembles. The pressure may alternatively be maintained by a Nosé-Hoover approach in order to produce correct ensembles.

The idea proposed by Nosé was to reduce the effect of an external system, acting as a heat reservoir, to an additional degree of freedom. This heat reservoir controls temperature or pressure of the given system, where it fluctuates around a target value. The thermal interaction between the heat reservoir and the system results in the exchange of the kinetic term between them.

Molecular dynamics (MD) simulations generate trajectories in phase-space by treating the nuclei classically and integrating Newton's or Hamilton's equations of motion numerically. Conventionally, the forces in the system are derived from a potential energy function which is ideally a good approximation to the true potential energy of the system. It is often the case, though, that an accurate potential function is not available, especially when it is not even clear physically what the form of that potential function should be; metal clusters are a good example of such a case. In order to perform MD simulations for such system, we need an alternate means of calculating internuclear forces. In ab initio molecular dynamics (AIMD) the potential energy of the system is calculated using quantum mechanics. The main drawback of AIMD is its computational cost.

2.9   Computational Details

Along this thesis calculations were carried out using density functional theory (DFT) with periodic boundary conditions as implemented in the *Vienna Ab Initio Simulation Package* (VASP)[214,215] code. All calculations were performed considering the projector augmented wave (PAW)[203,216] pseudopotentials. The external electrons were expanded in plane waves with kinetic energy cutoff equal to 500 eV. The chosen functional was the PBE exchange correlation GGA functional.[217] This functional is the most commonly used for studying RuO_2 and correctly describes its conducting nature. The D2 Grimme's dispersion correction was included in all slab calculations since it is essential to properly describe water adsorption and hydrogen bonding.[194] Test calculations with the most recent D3 correction for dispersion were also performed with the aim of analyzing the influence of the Grimme's parametrization in the adsorption energies and relative stabilities between H_2O and the OH^-/H^+ dissociated structures. Results are summarized in the appendix of chapter 4 (Table B.1) and show that D3 parametrization marginally reduces the adsorption energy by less than 2.6 kJ mol^{-1}. Furthermore, this diminution of the adsorption energy is very similar for both kind of structures thereby leading to essentially the same relative stability between the two forms.

Bulk calculations were performed considering a K-point mesh for the Brillouin zone of (15,15,15) employing the Monkhorst-Pack grid (MP),[218] while slab calculations were performed considering a Monkhorst-Pack K-point mesh of (6,6,1). The cutoff and K-point mesh were calibrated by ensuring the convergence of both cell parameters and cell energies in the appendix of Chapter 3 (Table A.1 and A.2). The energy convergence criteria were fixed to 10^{-5} and 10^{-4} eV for electronic and geometry relaxations, respectively.

Surface models of the main crystallographic orientations were built by cutting out the slab from the optimized bulk structure, with the MOLDRAW graphic program.[219] Slabs were constructed considering a (2 × 1) supercell and a 4-layer

thickness, the minimum slab thickness for a surface energy convergence (chapter 3, Table 3.4). The c value was set to 35 Å ensuring an interlayer distance of at least 21 Å to minimize the interaction between replicas at the (hkl) perpendicular direction. The size of the models was large enough to represent the main properties and atoms positions were fully relaxed.

Surface energies of the different facets were computed through the following equation in gas phase:

$$\gamma_{(hkl)} = \frac{E_{slab} - (NE_{bulk})}{2A} \tag{2.45}$$

where E_{slab} is the energy corresponding to the relaxed surface without optimizing the bulk cell parameters; E_{bulk} is the fully relaxed bulk energy; N is the number of formula units in the slab per units in the bulk unit cell, and $2A$ the corresponding two cross-section area of the slab. We also computed the surface energies considering the adsorption of a water monolayer as:

$$\gamma_{int\,(hkl)} = \gamma_{clean\,(hkl)} + \Theta \frac{E_{ads}}{A/n_{\mathrm{Ru}}} \tag{2.46}$$

where θ is the water coverage (H_2O molecules per Ru center); E_{ads} is the adsorption energy per water molecule and n_{Ru} is the number of defective ruthenium centers per surface unit cell.

Water adsorption on the surfaces at different coverages was studied by varying the number of water molecules per unit cell from on to four for surfaces (110), (100) and (001) and from one to eight for the (011) facet. In both cases, the largest number of water molecules corresponds to a water monolayer on the surface. Two type of water adsorption energies are reported along this thesis: (i) the adsorption energy per water molecule, which is calculated through:

$$E_{ads} = \frac{E_{(hkl)+\mathrm{H_2O}} - E_{(hkl)} - (n_{\mathrm{H_2O}} \cdot E_{\mathrm{H_2O}})}{n_{\mathrm{H_2O}}} \tag{2.47}$$

where the $E_{(hkl+\mathrm{H_2O})}$ is the total energy of the slab with th adsorbed water; $E_{(hkl)}$ is the total energy of the slab model; E_{H2O} is the total energy of an isolated water inside a (15 × 15 × 15) Å^3 cubic box, and $n_{\mathrm{H_2O}}$ is the number of adsorbed waters onto the surface; and (ii) the adsorption energy per surface, which is calculated through:

$$E_{ads/A} = \frac{E_{(hkl)+\mathrm{H_2O}} - E_{(hkl)} - (n_{\mathrm{H_2O}} \cdot E_{\mathrm{H_2O}})}{A} \tag{2.48}$$

where all the terms are equal to those of (eq 2.47) except A, which stands for the surface area of the supercell.

Transition state geometries (TS) and energy barriers (ΔE) were studied through the climbing image nudged elastic band (CI-NEB) method, as implemented in the VASP transition state tools (VTST) code.[220,221] The climbing image variation was used in order to converge onto the saddle point and explore the minimum energy path (MEP). For that, we use four images between reagents and products and the Quick-Min algorithm as optimizer.[222] As a convergence criteria, the maximum force at any atom in every image was required to be below the 0.05 $eV/\text{Å}$ threshold. Transition states were finally verified by the presence of a single imaginary frequency through harmonic vibrational analysis shown in the appendix from Chapter 4 (Table B.2).

Ab Initio Molecular Dynamics (AIMD) were carried out on the most stable water monolayer structures for both (110) and (011) surface. The energy convergence criteria were fixed to 10^{-4} eV. AIMDs were carried out considering an equilibration period of 1 ps (1000 steps of 1 ft) and a production period of 7 ps (7000 steps of 1 ft) in the NVT ensemble. During both the equilibration and the production periods, only the water monolayer and the first layer of the surface were allowed to move according to the motion's equations, while atoms of the remaining surface later were maintained at fixed positions. This option was chosen in order to avoid unrealistic deformations of the structure and to simulate the actual rigidity of the material.

Chapter 3

From Surfaces to Nanoparticles

"I miss the old days, when nearly every problem in X-ray crystallography was a puzzle that could be solved only by much thinking."

Linus Pauling

RuO_2 is a conducting transition metal oxide that has unique redox properties to be used as heterogeneous catalyst for oxidation reactions[132–138] as well as in electrocatalysis.[139–143] In this context, a detailed knowledge of the RuO_2 unit cell (3D), surfaces (2D) and nanoparticles (0D) is important for a better understanding of the catalytic properties. This chapter is organized as follows: (i) the RuO_2 bulk electronic structure is analyzed and compared with experimental data, defining the general methodology used in this thesis, (ii) main crystallographic orientations of RuO_2 are analyzed in terms of electronic structure and surface energy and (iii) the main procedure to build nanoparticle models of different sizes is discussed, as well as their structure, electronic and magnetic properties.

3.1 RuO$_2$ Bulk Material

RuO$_2$ crystallizes in a rutile-like structure with space group $P4_2/mnm$. The tetragonal unit cell of utile presents Ru positions, two per cell, which are fixed at the corner (0, 0, 0) and at the body center (0.5, 0.5, 0.5). The O positions, four per cell, have general coordinates (x, x, 0), $(1 - x, 1 - x, 0)$, (0.5+x, 0.5−x, 0.5) and (0.5−x, 0.5+x, 0.5), with a variable parameter, x, whose value must be determined experimentally. The body center Ru atom is coordinated octahedrally to six oxygens with four long Ru-O bonds in the basal plane and two short distances in the apical position i.e it exhibits a tetragonal compression as octahedral distortion. The oxygens are coordinated trigonally to three Ru atoms with two long and one short Ru-O distances. The RuO$_6$ octahedra links by sharing edges and corners to form a 3D framework, where the unit cell is shown in Figure 3.1.
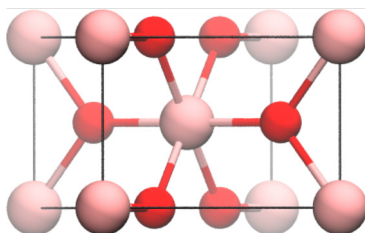
Figure 3.1: Ruthenium oxide RuO$_2$ unit cell.

Because of it has been suggested that RuO$_2$ has magnetic properties, we decided to consider both closed d shell and spin-polarized (open-shell) solutions, where the electronic structure and magnetic properties of the bulk material will be analyzed at different levels of theory. Ru atom has a [Kr]5s^{2}4d^6 electronic configuration, although the metal cation can be formally considered as Ru^{+4} with four d electrons.[223–225]

3.1.1 Functional Calibration

A wide range of DFT functionals have been employed to analyze their performance in reproducing the structural and electronic behaviors of RuO$_2$, shown

in Table 3.1. Two different sets of DFT calculations (GGA and hybrids) have been performed with atom-centered Gaussian-type functions as implemented in Crystal14 code,[226] which allows efficient calculations with hybrid functionals.

Table 3.1: Cell parameters of RuO$_2$ unit cell at different levels of theory with Crystal14.

DFT Functional	a=b	c	Cell Volume	Band Gap
GGA				
PBE	4.543	3.159	65.20	–
PBE-D2	4.488	3.170	63.86	–
BLYP	4.506	3.202	65.02	–
M06L	4.534	3.191	65.59	–
Hybrids				
B3LYP	4.459	3.178	63.18	–
PBE0	4.427	3.148	61.71	–
HSE06	4.426	3.149	61.72	–
M06	4.514	3.163	64.45	–
BHLYP	4.410	3.183	61.91	3.39
M062X	4.482	3.212	64.52	3.42
Experimental	4.491	3.130	62.68	–

Cell parameters in (Å), cell volume in (Å^3) and Band gap in (eV)

Regarding the electronic structure, it can be observed that GGA functionals and hybrid functionals with low percentage of exact exchange describe RuO$_2$ as a conductive material. In contrast, a band gap of about 3.4 eV is determined with hybrid functionals with a high percentage (50 %) of exact exchange, such as BHLYP or M062X, which does not corresponds with the conductive nature of RuO$_2$.

Cell parameters with GGA functionals are, however, too large compared to experiments, but this seems to be corrected by introducing the Grimme's corrections for dispersion. Indeed, PBE-D2 results are very close to experiments. Because of that, we decided to analyze if equivalent results can be obtained with plane-

wave basis sets as implemented in the VASP code.[215] Two different Grimme's corrections (D2 and D3) were considered to account for the dispersion forces (Table 3.2). Energy cut-off and k-points calibration are summarized in (Table A.1 and A.2).

Table 3.2: RuO_2 main structural parameters with VASP code.

DFT Level	a=b	c	d(Ru-O)$_{ax}$	d(Ru-O)$_{eq}$	d(Ru-Ru)	q(M)	q(O)
PBE	4.545	3.136	1.965	2.004	3.576	+1.71	-0.854
PBE-D2	4.487	3.150	1.945	1.997	3.543	+1.60	-0.750
PBE-D3	4.529	3.129	1.957	1.999	3.564	+1.00	-1.000
Experimental	4.491	3.130	1.942	1.984	3.536	-	-

All values in Å

As shown in Table 3.2, empirical dispersion correction is required in order to reproduce the experimental values of the RuO_2 cell parameters. As expected, accounting for dispersion corrections decreases the Ru$-$O distances, where comparisons between D2 and D3 corrections shows that PBE-D2 method is the one that better compares to experimental values. Because of this we have considered PBE-D2 as the level of theory all along this thesis.

3.1.2 Magnetism

Spin-polarized calculations within the framework of density functional theory (DFT) are a powerful tool to describe magnetism properties in solid state materials. Such calculations are not only the basis for a quantitative theoretical determination of spin magnetic moments, they can also be used to understand the basic mechanisms that lead to the occurrence of magnetism in solid state materials.

RuO_2 have a formally charged Ru^{+4} atom with four electrons distributed in d orbitals. Since Ru atom exhibit an octahedral environment, the (t_{2g}) electronic configuration has 4 electrons consisting on one electron pair and two unpaired electrons. Unoccupied e_g orbitals are higher in energy with respect to the t_{2g}

ones. RuO$_2$ has two formula units per cell, which means that two magnetic configurations are possible: Ferromagnetic or Antiferromagnetic configurations. Ferromagnetism is described at the atomic level, as caused by unpaired electron spins lined up parallel with each other presenting a net magnetic moment in the absence of an external magnetic field. In contrast, antiferromagnetism have the magnetic moments aligned in a regular pattern with neighboring spins pointing in opposite directions, resulting in a net magnetic moment equal to zero as can be seen in Figure 3.2.
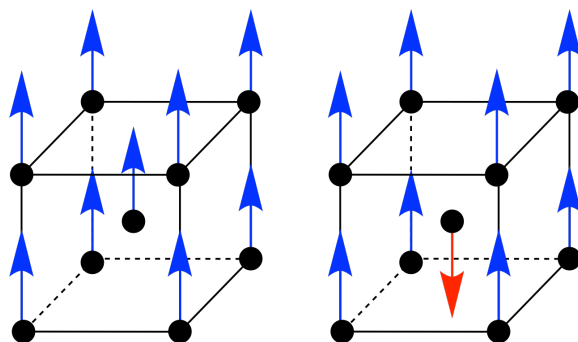
Figure 3.2: (Left) Ferromagnetic and (Right) Antiferromagnetic unit cell.

DFT calculations of both magnetic configurations have been performed in order to determine which is the most stable electronic configuration. Furthermore, the influence of non-covalent interactions accounted for by D2 and D3 Grimme's corrections has also been analyzed. Such empirical correction can distort the octahedral environment around the Ru atom leading to different structural and magnetic behaviors (Table 3.3).

Table 3.3: Cell parameters from Spin-polarized RuO_2 unit cell optimizations in (Å), magnetization in (Bohr magnetons) and relative energies (in eV).

DFT Level	Magnetism μ_B	a=b	c	d(Ru-O)$_{ax}$	d(Ru-O)$_{eq}$	d(Ru-Ru)	μ_B(Ru)	μ_B(O)	ΔE
PBE	FM (4.00)	4.722	2.990	1.997	2.009	3.659	1.440	1.430	0.00
	AFM^a (0.00)	4.545	3.136	1.966	2.004	3.576	0.000	0.000	-78.15
PBE-D2	FM (4.00)	4.661	3.00	1.973	2.001	3.622	1.438	0.221	0.00
	AFM^a (0.00)	4.487	3.15	1.944	1.997	3.542	0.000	0.000	-91.16
PBE-D3	FM (4.00)	4.712	2.97	1.988	2.004	3.648	1.433	0.223	0.00
	AFM^a (0.00)	4.529	3.13	1.958	1.999	3.565	0.000	0.000	-79.73

(a) The AFM configuration collapses to the non-magnetic one.

The antiferromagnetic configuration cell parameters and the Ru−O distance are identical to that of the closed-shell system discussed in the previous section. That is, net magnetic moment at each Ru is equal to zero indicating that the AFM solution collapses to the non-magnetic (NM) solution. D3 Grimme's empirical correction is still mismatching the experimental cell parameters in comparison with D2 correction. Energetic at the PBE-D2 level of theory states that the NM situation is 91.16 $kJ \cdot mol^{-1}$ more favorable than the ferromagnetic one. The energy difference between the two states is smaller 79.73 $kJ \cdot mol^{-1}$ with PBE-D3. The ferromagnetic configuration has a net magnetic moment of $\mu_B = 4.00$ because there are two unpaired electrons aligned in the same direction for each Ru atom. Such magnetic configuration enlarge a and b parameters in comparison to the non-magnetic system. This distortion is produced because of the elongation of the Ru-O axial bond, due to the inner repulsion that the unpaired electrons of the two unit formulas generate. This difference between empirical corrections and magnetic configuration can be understood with the octahedral distortions that are consequence of the non-covalent interactions. Because of the elongation of the Ru−O axial bond with D3 method, here the crystal field is decreased favoring the $[\uparrow\downarrow, \uparrow, \uparrow]$ electronic distribution for the t_{2g} orbitals, stabilizing the ferromagnetic situation. Different solutions for the AFM, FM and NM situations have also been obtained employing the Hubbard Correction at the PBE+U-D

level of theory in Dudarev's formulation. Results show that upon increasing the effective parameter U$_{eff}$ value the AFM solution does not collapses to the non-magnetic one. Furthermore, for U$_{eff}$ values larger than 1.20 the AFM solution is always the most stable solution.

RuO$_2$ unit cell has long been considered a Pauli paramagnet, but Jahn-Teller distortions can be accompanied by antiferromagnetism character.[227,228] Temperature experiments shows that up to at least 300 Kelvin it presents a small magnetic moment of approximately 0.05 μ_B evidenced by polarized neutron diffraction. Such low magnetic moment has been attributed to the rutile structure, which permits an antiferromagnetic interaction.[229,230] In particular, the discovery of AFM in RuO$_2$ and its relatively high Néel temperature is significant because metallic AFM oxides are rare and their ordering temperature are generally low. Finally, it should be mentioned that these calculations are performed without taking into account thermal contribution, which seems to be the responsible of the antiferromagnetic configuration above the Néel temperature.

3.2 RuO$_2$ Crystallographic Orientations

Any bulk crystal structure have many low Miller index faces that could be formed. The surface energy for the various faces may be quite different, however, so that only certain ones will be formed preferentially in experiments. The surfaces that will be considered here are those that have been observed experimentally in RuO$_2$ studies or have been attempted to be prepared. It should be noted that the ideal surface structure presented here have the stoichiometry of the bulk material by definition. The closest that one can expect to come to this type of surface in practice is to cleave a single crystal in ultra-high vacuum (UHV) conditions.
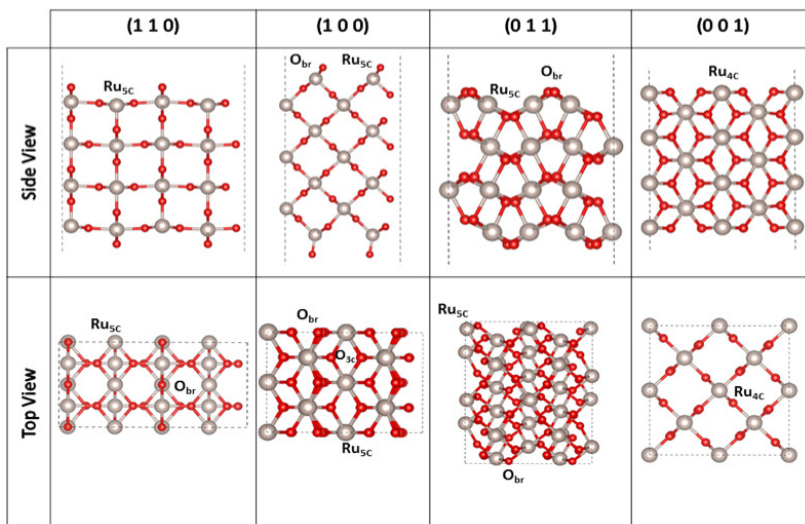
Figure 3.3: Main crystallographic orientations of RuO_2 with top and side view.

Crystalline periodic two-dimensional RuO_2 slab models for the nonpolar (110), (011), (100) and (001) surfaces were derived by cutting out a (2x1) supercell from the optimized RuO_2 bulk along the corresponding directions (Figure 3.3), and optimized keeping the cell parameters fixed. Surface thickness has been calibrated in terms of surface energy through a range from 2 to 8 layers along the z axis in order to represent better the material stiffness and the bulk-like properties of the surface middle part (Table 3.4). It is observed that the surface energy is almost converged with a four layer slab model. Thus, the four layer thickness slab is the one considered from now on.[231,232]

Table 3.4: Surface energy as function of the slab model thickness at PBE level of theory. All values in $eV/\text{Å}^2$.

Layers	$\gamma_{(110)}$	$\gamma_{(100)}$	$\gamma_{(011)}$	$\gamma_{(001)}$
2	0.0671	0.0844	0.0724	0.2334
4	**0.0657**	**0.0823**	**0.0742**	**0.2251**
6	0.0658	0.0821	0.0744	0.2245
8	0.0660	N.A	0.0817	N.A

The (110) and (011) facets have at the outermost layer 2-coordinated bridging oxygen O_{br} and 5-coordinated Ru_{5c} centers, which differ on the nature of the vacant site. The vacant site in the Ru_{5c} center of the (110) surface is axial, while that on the (011) surfaces is equatorial. The (100) surface exhibits a saw morphology, with 2-coordinated oxygen atoms (O_{2c}) and 3-coordinated (O_{3c}) bonded to 5-coordinated Ru_{5c} atoms, with the vacant site in axial position. Finally, the (001) facet displays all Ru atoms as a 4-coordinated Ru_{4c} and all the oxygen atoms as 2-coordinated O_{2c}, the vacant sites of Ru_{4c} centers being both equatorial.

The Ru-O distances of the outermost layer of the different slabs, the Bader charges of the oxygen bridge (O_{br}) and unsaturated ruthenium atoms, as well as the computed surface energies (with and without Grimme's correction) are given in Table 3.5, which also includes the values of the bulk for comparison. The surface energies of all stoichiometric orientations are similar to previous values reported in the literature.[233] It can be observed that, the internal 6-coordinated Ru_{6C} atoms present Ru-O distances (1.90 - 2.05 Å) that are close to the bulk values and are not discussed further. Regarding the surface atoms, the Ru-O distances vary depending on the coordination environment, the strongest bonds corresponding, as expected, to 4-coordinated Ru_{4C} atoms, present at the (001) surface. Indeed, the 5-coordinated Ru_{5C}, present at the (110), (100) and (011) surfaces, show significantly larger bond distances (average values ranging from

1.96 to 1.97 Å compared with 1.89 Å for the (001) surface). Remarkably, the distance between unsaturated surface Ru-centers varies significantly from one surface to another. The shortest distances (3.173 Å) are found for the (110) and (100) surfaces, while the Ru-Ru distances in the (001) surfaces are significantly larger (4.543 Å).

Table 3.5: Computed surface energies $\gamma_{(hkl)}$ and Ru-O distances of the outermost layer of the main crystallographic orientations. Surface energies are in $eV/\text{Å}^2$ and distances in Å.

(h k l)	$\gamma_{(hkl)}$	$\gamma^b_{(hkl)}$	d(Ru-O)$_{eq}$	d(Ru-O)$_{ax}$	d(Ru$\cdots$Ru)	q^a_{Ru}	q^a_{O}
Bulk	–	–	1.996	1.945	3.137	+1.71	-0.85
(1 1 0)	0.066	0.098	1.995	1.880	3.137	+1.60	-0.75
(0 1 1)	0.074	0.105	1.873-2.111	1.948	3.735	+1.64	-0.78
(1 0 0)	0.082	0.119	1.926 - 2.032	1.901	3.137	+1.65	-0.75
(0 0 1)	0.099	0.134	1.923	1.849	4.543	+1.54	-0.81

(a) Bader atomic charges of the Ru and O unsaturated atoms of the surface.

(b) Surface energies taking into account Grimme's dispersion.

3.2.1   Wulff Construction

Surface energies can be used to get the equilibrium shape of a crystal (under vacuum conditions) through the Wulff construction approach (Figure 3.4). That is, the shape of an equilibrium crystal is obtained, according to the Gibbs thermodynamic principle, by minimizing the total surface free energy associated to the crystal-medium interface.

The principle of minimum free energy appeared firstly in the fundamental work of J.W. Gibbs in (1875-8)[234] where, the role of an anisotropic surface tension for the determination of the shape of a crystal in equilibrium was shown and the formation of facets discussed. After that, in (1901) G.Wulff,[235] who made classical experiments on crystal growth stated the Wulff's Theorem:

"The minimum surface energy for a given volume of a polyhedron will be achieved if the distances of its faces from one fixed point are proportional to their capillary constants."

where the term capillary constants can be translated as the surface energy. This way, the surface contribution can be estimated by a vector perpendicular to the surface (hkl) from the center of a crystallite, whose length (l) is proportional to its surface free energy (γ_{hkl}):

$$l_{hkl} = c_{hkl} \cdot \gamma_{hkl} \tag{3.1}$$

At this point it should be noted that due to the complexity of the crystal growth, the ideal equilibrium form will only be achieved for very small crystals. According to the Wulff construction the surfaces presenting the shortest vectors will be predominant. As a result, it is possible to get the so-called *Wulff Construction* as a polyhedron that depends on: (i) the ratios between surface energies, (ii) the symmetry point group of the bulk structure and (iii) the chemical composition of the surrounding media. Therefore, the higher the number of crystallographic facets used to construct the Wulff shape, the higher the difficulty in building it.

In our case, the surface families with lower surface energies are the (110) and (011) ones, which account for the 43.6 % and 49.2 %, respectively, of the total surface area (Figure 3.4). Note that (011) family present a higher contribution than the (110) one despite the higher surface energy of the former. This is associated to the fact that there are eight equivalent orientations of (011) given by symmetry, while the (110) family only has four equivalent planes. Surfaces equivalent to the (100) face slash the edge between the (110) family surface and account for a 7.2%. Finally, the (001) facet, with the highest surface energy has a negligible contribution to the equilibrium shape. Note that this structure should only be related with crystal growth in vacuum. Solvation would lead to a different stabilization of different facets and this will also depend on other variables such as pH. In any case, present results are in good agreement with experimental observations in single crystals grown by deposition from the vapor face through a process in which only the constituents or ruthenium oxides are in the reactor.

The available data show that (011) is the predominant facet followed by the (100) and (110) ones.
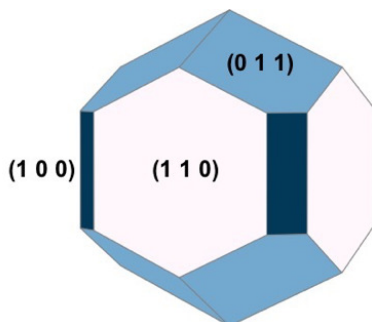
Figure 3.4: Ruthenium oxide Wulff construction obtained with the here computed surface energies in gas phase.

3.3   RuO$_2$ Nanoparticle Models

The first two sections focused on the results for the RuO$_2$ unit cell and main surfaces. Such results have been discussed in terms of structural, electronic and magnetic properties to acquire the necessary knowledge about RuO$_2$ as a macroscopic material being 3D and 2D, respectively. Moreover, the main surfaces have been studied in terms of surface energy which is a key point in order to construct the Wulff shape of a thermodynamically stable nanoparticle in vacuum conditions. The obtained Wulff construction is an empty pattern that will be used to build the atomisc models of stoichiometric and defectless RuO$_2$ nanoparticles of different sizes. It should be noted that the methodology to build atomistic models of metal oxide nanoparticles was in an early stage at the beginning of this thesis with only few models of rutile and anatase TiO$_2$ and CeO$_2$ materials, without any software capable to get stoichiometric Wulff-like nanoparticles. This has been overcome by designing a handmade methodology which will be discussed in a more deep way in the following sections.

3.3.1   Building Metal Oxide Nanoparticles

Wulff theory has been used to build up atomistic models of metal oxide nanoparticles of RuO$_2$ using the knowledge acquired from the slab models of the corresponding main crystallographic orientations. Preliminary information from the unit cell, symmetry group and surface energies of the main orientations is also required to get the Wulff construction and the nanoparticle atomistic model. This procedure can be generalized to any kind of known metal oxide structure. The main steps of the overall workflow are summarized in Figure 3.5.

First of all, the surface energies (Table 3.5) and the material symmetry point group ($P4_2/mnm$) are used to construct the empty Wulff shape (Figure 3.4), by lowering the global surface energy and taking into account the contribution of each facet. The distance between each crystallographic facet and the Wulff center is proportional to the surface energy and defines the size of the resulting nanoparticle. The nanoparticle size can be tunned by modifying the surface energy of all the orientations by a scaling factor. The next step consists in replicating the material unit cell inside the empty Wulff construction and slice each orientation propagated by the material symmetry operations of each facet. This can be done with the VESTA visualization software. In this stage the resulting atomistic model of the metal oxide nanoparticle may not be stoichiometric *dirty nanoparticle* in Figure 3.5. Such non-stoichiometric model normally, but not always, exceeds the number of oxygen atoms present in the nanoparticle shell so that some of them need to be removed to become stoichiometric.

Exceeding atoms were removed by hand, such handmade procedure was accomplished by establishing the following criteria in terms of chemical sense. First, only exceeding oxygen atoms from the nanoparticle shell are candidates to be removed. Secondly, removal of O atoms will lead to under-coordinated metal atoms and only 5 and 4-coordinated metal atoms were allowed. This means that 3-coordinated metal atoms or less were totally avoided, because any slab model present such coordination environment.

Nanoparticle Building Procedure

Optimized Bulk Structure and Main Crystallographic Orientations

Build the Wulff shape
(Using Surface Energies and Symmetry Point Group)

Fill the Empty Wulff Shape with the Optimized Bulk Structure
(Slice each Crystallographic Orientation)

Dirty Nanoparticle (Non-Stochiometric)

Remove atoms by hand, until reach a stochiometric nanoparticle model
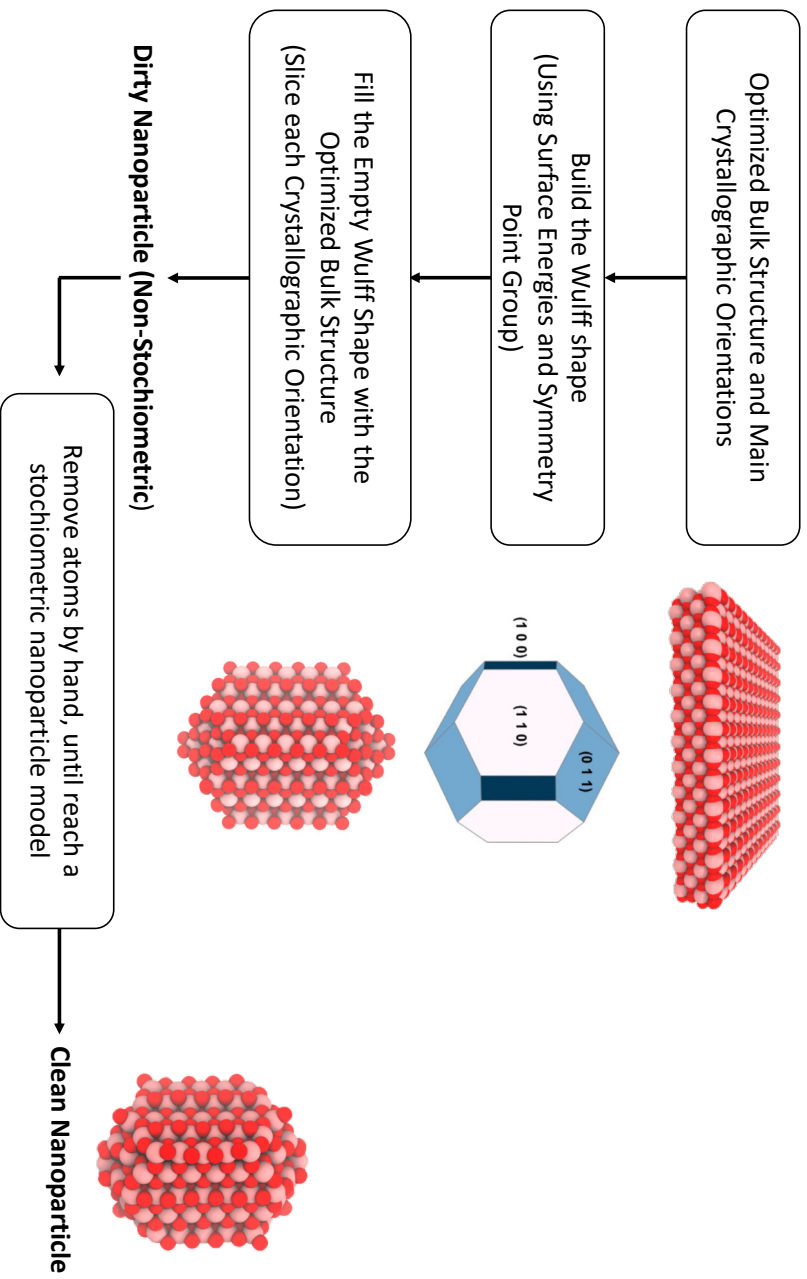
Clean Nanoparticle

Figure 3.5: Hand-Made building procedure for RuO_2 nanoparticles.

Third, the intrinsic symmetry of the modeled material, concerning the Wulff shape, needs to be preserved by removing oxygen atoms equivalents in terms of position and chemical environment. Finally, remaining oxo groups placed in the nanoparticle shell are spread symmetrically around the nanoparticle avoiding interaction between them.

This building procedure has allowed us to construct Wulff-like, defectless and stoichiometric RuO$_2$ nanoparticle atomistic models of different sizes from 0.94 to 3.0 nm. Such models will make accessible the comparison between the macroscopic surfaces and RuO$_2$ nanoparticles in terms of water interaction and their catalytic performance in oxygen evolution reaction (OER). Furthermore, inner comparisons between models are also possible as a function of their size, shape and different kinds of active sites on the nanoparticle's shell.

Structural analysis of the optimized nanoparticle models (Figure 3.6) has also been performed. For that, models were placed in a cubic box of 25Å in each direction in order to avoid lateral interaction between images, because of the periodic boundary conditions, and optimized at the PBE-D2 level of theory. Table 3.6 reports the RuO$_2$ units in the nanoparticle structure, Ru atoms coordination percentages and the available open positions as possible catalytic active sites.

Table 3.6: Metal coordination percentage on nanoparticle models as a function of their size.

Nanoparticle Size	RuO$_2$ Units	Ru$_{4c}$	Ru$_{5c}$	Ru$_{6c}$	Open Sites
0.94 nm	34	47%	35%	17%	44
1.20 nm	33	36%	42%	21%	38
1.80 nm	51	24%	51%	25%	50
2.40 nm	165	12%	41%	47%	108

The predominant metal coordination environment in the 0.94nm nanoparticle is the 4-coordinated Ru_{4c} one, whereas from 1.20 to 1.80 nm the 5-coordinated Ru_{5c} becomes the preferred ruthenium coordination and onto the 2.40 nm nanoparticle the Ru_{6c} turns to be the more prevailing coordination environment. That is, the smaller the nanoparticle the larger is the percentage of undercoordinated metal atoms (Figure 3.6).
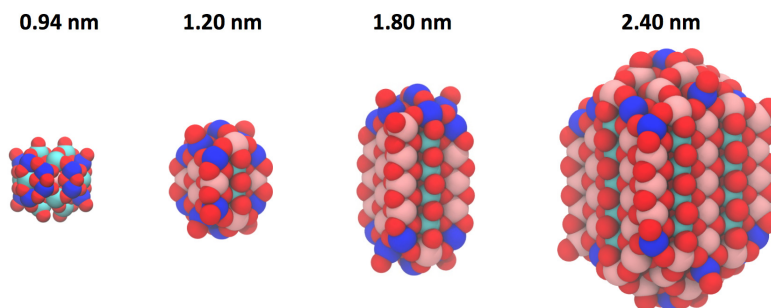

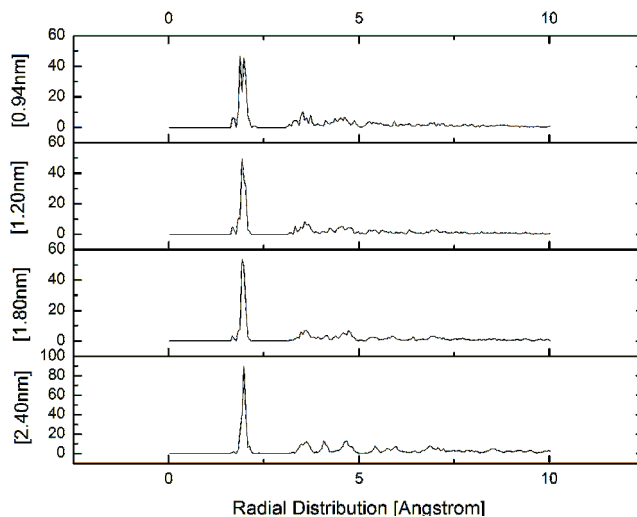**Figure 3.6:** Nanoparticle models of different sizes (Ru coordination labeled).

Figure 3.7: Pair distribution function [Ru−O] of the nanoparticle models.

The pair distribution function (PDF) represents the probability of finding a pair of atoms with a particular interatomic distance and provides information on the crystallinity of the nanoparticle. Figure 3.7 shows the PDF function of our built nanoparticle models.

As can be seen, for the 2.40 and 1.80 nanoparticle models there is a sharp peak with narrow width due to its crystalline structure behavior. The main peak is located at 1.95 Å which corresponds to the Ru$-$O distance located on the RuO$_6$ octahedral positions in the crystalline like rutile structure. However, for smaller nanoparticles this peak is splitted. This is clearly evidenced for the 0.94 nm nanoparticle, due to the higher presence of undercoordinated metal ions.

3.3.2   Nanoparticle energy formation analysis

Nanoparticle formation energy, E_F can be evaluated as defined by Christoph Loschen[236] with respect to the *hcp* Ru^0 metal unit cell and the oxygen O$_2$ structure in the gas phase.

$$E_F = \frac{1}{n} \cdot (E_{\mathrm{Ru_n O_m}}) - (E_{\mathrm{Ru^0}}) - \frac{m}{2n} \cdot (E_{\mathrm{O_2}}) \tag{3.2}$$

Where, n and m are the number of metal and oxygen atoms of the nanoparticle and $E_{\mathrm{Ru_n O_m}}$, $E_{\mathrm{Ru^0}}$ and $E_{\mathrm{O_2}}$ the respective DFT energies of the whole nanoparticle, metal ruthenium bulk and molecular oxygen, respectively. the nanoparticle formation energy and the average coordination number of the Ru atoms shows a lineal relationship across nanoparticles of the same family and converge to the macroscopic bulk material (Figure 3.8). Note that, nanoparticles with size below 1 nm breaks the lineal relationship, because of poor structural symmetry. As a consequence the 0.94 nm nanoparticle does not belong to the same structural family that the other ones, despite it was built with the same approach. This is also in agreement with the fact that this nanoparticle is the one that exhibits lower crystallinity.
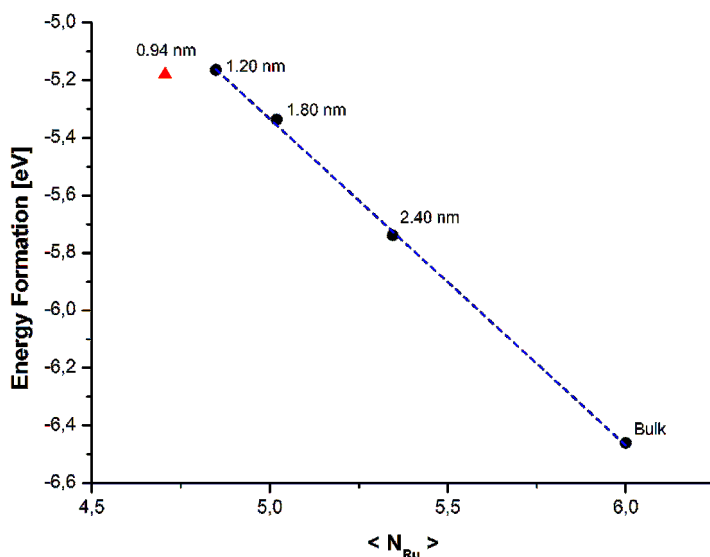
Figure 3.8: Lineal relationship between nanoparticles of the same family to bulk material.

3.3.3   Nanoparticle Magnetism

Magnetism has been analyzed on the 1.20 nm nanoparticle model at the PBE-D2 level of theory both considering spin-polarized and closed-shell approaches. Results indicate that the magnetic solution is more stable by 0.10 eV than the non-magnetic one. The maximum spin density is in all the cases found in the most singular Tip locations, which correspond to the Ru_{4C} coming from the (001) crystallographic orientation as shown in Figure 3.9. This is due to the presence of an odd number of Ru atoms across the nanoparticle core, which leaves one unpaired electron on each Ru_{4C} Tip location; i.e, the nanoparticle can be described as a biradical triplet situation.

Although RuO_2 is often considered as non-magnetic, Ru−Ru antiferromagnetic interactions are observed in the nanoparticle core, which decreases the internal Ru−Ru distances leading to spin densities of almost zero at the internal Ru atoms, while spin densities on the Tip sites are 0.87 and 0.89 per site. Such antiferromagnetic interaction have been also observed experimentally in RuO_2 nanoparticles.[229]
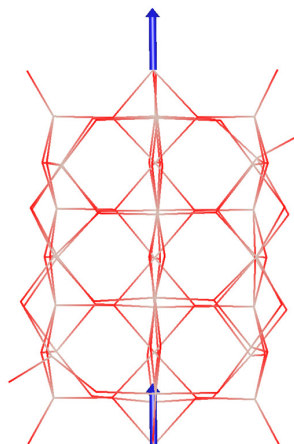
Figure 3.9: 1.20 nm nanoparticle with magnetic moments on Tip locations.

3.4   Conclusions

The present chapter analyzes the RuO_2 material, surfaces and nanoparticles by means of periodic DFT calculations. Results indicate that such material presents interesting conducting and magnetic properties that are sensible to the level of theory used. It has been shown that GGA functional PBE along with the D2 dispersion correction provides excellent results compared to experimental X-ray values for the bulk structure.

The main crystallographic orientations (110), (100), (011) and (001) have been modeled and classified in terms of structural and surface energy from the most stable one (110) to the less stable (001) surface. These (2D) systems presents its own physico-chemical properties usually related with the surface topology, such

as the presence of 5-coordinated or 4-coordinated metallic centers the distance between them or the availability of basic oxygen atoms on top of the surface. Then, thanks to the Wulff Theorem, which depends on the material symmetry and the surface energy of the main facets the thermodynamically more stable nanoparticle shape was able to be represented.

Finally, a hand-made procedure has been developed in order to study the transition from the bulk material (3D) through the (2D) facets to reach faceted Wulff-like, defect-less and stoichiometric RuO_2 nanoparticles of different sizes. Those models, obtained from the hand-made method, have been analyzed in terms of structural such as available coordinations on the nanoparticle shell and open sites as potential reactive points. However, the energetic relationship between nanoparticles sizes shows that the Wulff theorem has a size limitation, where nanoparticles smaller than 1nm are not well represented. Furthermore, in the research group, a free application (BCN-M) has been build from the hand-made method, which automatically slices nanoparticle models depending on the material symmetry and surface energy previously computed.

Chapter 4

RuO_2-H_2O Interface

> "A century ago, Petroleum - what we call oil - was just an obscure commodity; today is almost as vital to human existence as water"
>
> *James Buchan*

The following chapter focuses on the RuO_2-H_2O interface both in surfaces and nanoparticles. First, adsorption of water at the main RuO_2 surfaces, will be addressed to understand the intrinsic interaction between a single water molecule and the different RuO_2 facets. Cooperative effects between different adsorbed water molecules will also be analyzed by increasing the coverage from the half-monolayer to full coverage. Secondly, adsorption of water at RuO_2 nanoparticles of different sizes will be discussed with the aim of analyzing the interaction between an isolated water molecule at different locations present at the nanoparticle surface. Overall, electronic and thermal effects will be used to understand such interactions as a function of the water coverage, surface topology and nanoparticle size.

4.1　Introduction

The study of RuO_2-H_2O interaction is relevant to understand the catalytic activity of hydrous RuO_2 (RuO_2-xH_2O)[148,149] as well as the origin of the poisoning induced by water in the oxidation of CO.[150] Indeed, in the last few decades, considerable efforts have been devoted to study water and metal oxide interfaces,[138,151–155] due to their relevance in many scientific fields such as catalysis, electrocatalysis, corrosion, geology, or atmospheric science.[156–159] For the particular case of RuO_2, most of the existing studies focus on the most stable (110) surface, which is characterized by the presence of unsaturated pentacoordinated ruthenium atoms (Ru_{5C} and bridged oxygens (O_{br}).

The water-oxide interface has been studied by using several spectroscopic techniques such as X-ray scattering measurements, high-resolution electron energy loss spectroscopy (HREELS), and thermal desorption spectroscopy (TDS) as well as by means of scanning tunneling microscopy (STM)[160–164] and DFT calculations.[165–167] It has been found that the interface nature highly depends on the experimental conditions, particularly on the applied voltage. Regarding studies without the addition of other species or external voltages, Lobo and Conrad[160] concluded, from HREELS and TDS spectroscopies, that adsorption mainly involves non-dissociated water molecules. These molecules are located at Ru_{5c} centers and establish hydrogen bond interactions with O_{br} oxygens. Furthermore, water molecules desorb at around 400 K, which is consistent with a water adsorption energy of about -96 $kJ \cdot mol^{-1}$. Similar adsorption energies were obtained by means of DFT by Siahrostami and Vojvodic,[166] although they suggest that H_2O on RuO_2 is prone to dissociate. More recently, Dohnálek and co-workers combined STM microscopy and DFT calculations and analyzed the effect of water coverage on the (110) RuO_2 surface.[155,163,164,168] They showed that at very low coverages, single water adsorbs on Ru_{5C} centers and that the $Ru_{5C}-H_2O$ is in equilibrium with the dissociated $Ru_{5C}-OH\cdots H-O_{br}$ species, as a result of the Lewis acidity of the ruthenium atoms.

This study also shows that increasing the water coverage allows the formation of water dimers. The two water molecules of these dimers are adsorbed in contiguous Ru_{5C} centers and one of them is dissociated, which leads to the formation of the $H_3O_2^-$ motif. At even higher water coverages, hydrogen bonded chains of water molecules are formed. These chains are characterized by the presence of the same $(H_3O_2^-)^n$ motif, which constitutes the fundamental building block.[162–164,166,167]

At this point, is worth noting that at the beginning of this thesis, the adsorption of water molecules at different surfaces, besides the most stable (110) one, had not been addressed before. Only very recently a combined experimental and computational work appeared in the literature. In this work, ambient pressure X-ray photoelectron spectroscopy and in situ surface diffraction measurements as well as density functional calculation are used to study different facets of RuO_2 interaction with water under humid and electrochemical conditions. This study identifies that the crystallographic orientation is an important factor for water dissociation.

4.2   H₂O Interactions at RuO₂ Surfaces

A water molecule was adsorbed on to the clean surface with the aim of studying the intrinsic interactions between water and RuO_2 surfaces as a function of the surface topology. This corresponds to a water coverage of $1/4$ for surfaces (110), (100) and (001) and a coverage of $1/8$ for the (011) facet. We considered the adsorption of the water molecule in both the *molecular* and the *dissociated* (OH^-/H^+) forms. These two situations will be hereafter referred to *wat* and *dis*, respectively. We also located the transition structure connecting both minima through the image climbing nudged elastic band (CI-NEB) method.[220,221] The relative energies, the major structural parameters and the Bader charges[237] of the unsaturated Ru and O atoms are given in Table 4.1. Optimized structures, projected density of states (pDOS) and the potential energy profiles are shown in Figures 4.1 to 4.3.

Table 4.1: Water adsorption energies on the main RuO$_2$ facets ($kJ \cdot mol^{-1}$) at low water coverage $\theta = 1/4$ or $1/8$ and associated main structural parameters (in Å).

(hkl)		E_{ads}	O$_w$-H$_w$	O$_{br}$-H$_w$	Ru-O$_w$	q^a_{Ru}	q^a_O	q_{H_2O}
	wat	-131.3	1.038	1.588	2.172	+1.67	-0.87	+0.10
(1 1 0)	TS	-128.3	1.212	1.252	2.106			
	dis	-139.6	1.754	1.011	1.993	+1.68	-1.08	-0.46/+0.66
	wat	-115.4	1.021	1.615	2.177	+1.73	-0.89	+0.10
(0 1 1)	TS	-104.5	1.317	1.137	2.059			
	dis	-102.8	1.429	1.072	2.031	+1.79	-1.04	-0.49/+0.64
	wat	-129.2	1.013	1.688	2.180	+1.70	-0.87	+0.10
(1 0 0)	TS	-111.6	1.333	1.136	2.074			
	dis	-114.5	1.548	1.044	2.032	+1.76	-1.05	-0.46/ +0.60
(0 0 1)	wat	-133.8	1.018	1.627	2.172	+1.62	-0.93	+0.07

(a) Bader atomic charges of the Ru and O and unsaturated atoms of the surface.

In all considered surfaces, at least two different minima are found. One of these minima corresponds to the adsorption of water, while the other is related with the formation of OH$^-$/H$^+$ pairs through water dissociation. Regardless the surface morphology, the adsorbed water molecule interacts directly through its oxygen with the under-coordinated Ru$_{4C}$ and Ru$_{5C}$ to fill the empty coordination sites. Besides, a quite strong hydrogen bonding between one H atom of the water molecule and the nearest bridged oxygen O$_{br}$ is also formed.

The Ru$\cdots$O$_{wat}$ distances are similar in all surfaces and they range from 2.172 to 2.180 Å. Larger differences are observed for the H$_{wat}\cdots$O$_{br}$ distances, the values varying between 1.588 and 1.688 Å. The H$\cdots$O$_{br}$ distance seems to be related with the surface morphology, particularly to the distance between Ru$_{5C}$ and O$_{br}$. Indeed, the shortest H$\cdots$O$_{br}$ distances tend to be associated with the smaller separation between the Ru$_{5C}$ and O$_{br}$ centers. In the (001) surface, the most stable *wat* configuration is the water molecule with two hydrogen bonds to the

closest O_{br} atoms in a bifurcated manner, because of that the dissociated form was not reached through optimization. Alternatively, when the water molecule only presents one hydrogen bond to a O_{br} coming from the surface the dissociated from was found as shown in Figure 4.1. Even do, the *wat* form is still the most stable situation.
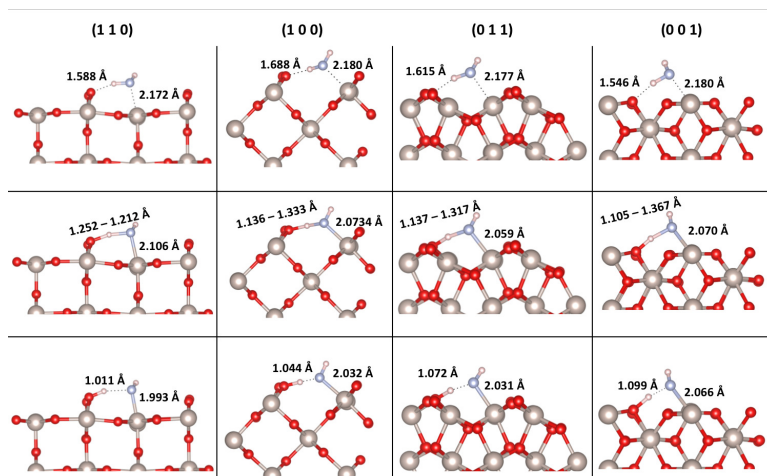

Figure 4.1: Optimized geometries for all considered RuO₂ surfaces of wat and dis structures and the transition states connecting them.

The water adsorption energy at the different surfaces ranges between -115.4 to -133.6 $kJ \cdot mol^{-1}$. The weakest adsorption (E_{ads} =-115.4 $kJ \cdot mol^{-1}$) corresponds to the (011) surface. In the other surfaces the adsorption energy is similar, ranging from -129.2 to -132.8 $kJ \cdot mol^{-1}$. This stronger interaction of water with the (110), (100) and (001) surfaces is related to the number and strength of the H$\cdots$O$_{br}$ hydrogen bonds, and from the nature of the vacant site (axial or equatorial). For instance, the vacant site Ru$_{5c}$ in the (110) surface is axial, whereas the vacant site in the (011) surface is equatorial.

Figure 4.2 shows the contribution to the DOS of the 2p orbitals of the oxygen bridge receiving the proton in the *dis* structure both in the clean surface and *dis* structures. Bader atomic charges show that the interaction between H₂O

and the surface produces some electron transfer from the water molecule to the surface. Interestingly, this electron density does not accumulate at the Ru center (that becomes even more positively charged with respect to the clean surface) but at the oxygen atoms of the surface and, particularly, at the oxygen bridge. This agrees with the DOS which shows that the interaction between water and the RuO$_2$ surface is established within an occupied p orbital of water and an empty d orbital of ruthenium (Figure B.1 and B.2). Remarkably, when comparing the contributions of the oxygen bridge p orbitals in the DOS of the different clean surfaces (Figure 4.2), it is observed that in the (110) surface the p orbital involved in the hydrogen bonding with water is at higher energies, thus suggesting higher basicity. Overall three key factors are identified: (i) the smallest the separation between the Ru$_{5C}$ and the O$_{br}$, the shortest the H$\cdots$O$_{br}$ distance and the strongest the H-bond; (ii) the higher the basicity of the O$_{br}$ sites in the (110) and (100) surfaces, the larger the strength of the H$\cdots$O$_{br}$ H-bond, and (iii) the presence of two hydrogen bonds in the case of the (001) surface also increases the adsorption energy.
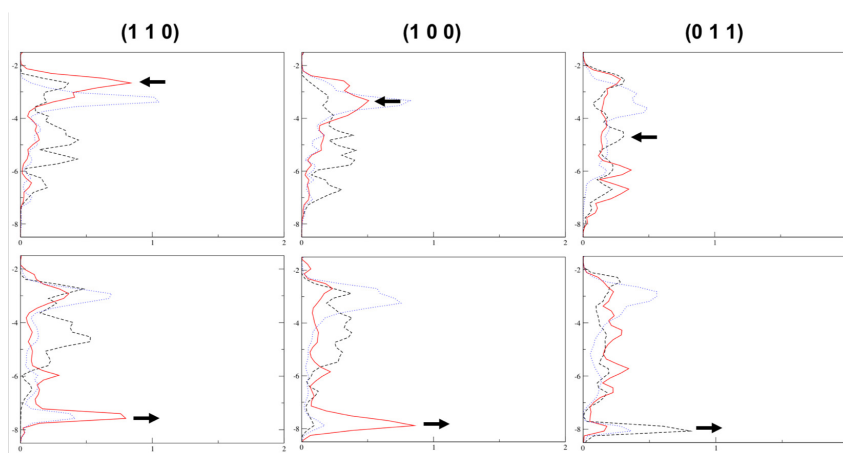

Figure 4.2: Projected density of states (pDOS) associated with the 2p orbitals of O$_{br}$ in the clean surface (top) and in dis structures (bottom). The red solid line is $2p_y$, the blue dotted line $2p_z$, and the dashed black line $2p_x$.

Structures in which water dissociates upon adsorption on RuO_2 show that the proton transfer towards O_{br} decreases the $Ru-O_w$ distance by around 0.1 and 0.2 Å, as a result of the larger OH^- basicity compared to that of H_2O. Similarly, the $Ru-O_{br}$ bond distance of the surface increases due to a decrease of the O_{br} basicity upon protonation (values ranging from 1.982 to 2.090 Å). Besides, the H^+ and OH^- moieties interact through hydrogen bonding. The $H_{br}\cdots O_w$ distance varies from 1.429 to 1.754 Å, indicating that the H-bond is stronger in the *dis* structure than in the *wat* one with the exception of the (110) surface. Regarding the energetics, calculations indicate that water dissociation is a favorable process (ΔE = -8.3 $kJ \cdot mol^{-1}$) only in the case of the (110) surface, reaction energies at the (011) and (100) surface being +12.5 and +14.7 $kJ \cdot mol^{-1}$. Remarkably, the thermodynamics of water dissociation correlates well with the $Ru-O_w$ distance after dissociation. Indeed, the shortest $Ru-O_w$ distance (1.993 Å) is found for the (110) surface and longer values (2.031 - 2.032 Å) are obtained for the (100) and (011) facets. Furthermore, the basicity of O_{br} is expected to be larger in the case of the (110) surface. This can be related to three factors: (i) the p orbital capturing the proton lies at higher energies in the (110) surface than in the other ones (Figure 4.2), (ii) the Bader charge on the O_{br} upon protonation becomes more negative than in the other surfaces, and (iii) the $Ru-O-Ru$ angle is smaller, which is usually associated with an increase of the basicity. Therefore, the energetics of water dissociation does not seem to be related to the strength of the H-bonding formed between the H^+ and OH^- moieties but with the interaction of these two fragments with the surface. That is, surface deformation energy upon proton transfer is small for all facets and the geometry features suggest that both Ru-OH and O_{br}-H interactions are stronger for the (110) surface, the only one in which dissociation is thermodynamically favorable.

The potential energy profiles corresponding to the water dissociation process on the different surfaces are shown in Figure 4.3. In all cases, the energy barrier is low; i.e., computed values range from 9.4 $kJ \cdot mol^{-1}$ for the (110) surface to 18.8 $kJ \cdot mol^{-1}$ for the (100) one. Indeed, the lowest energy barrier is found for the

thermodynamically preferred process (deprotonation on the (110) facet), while
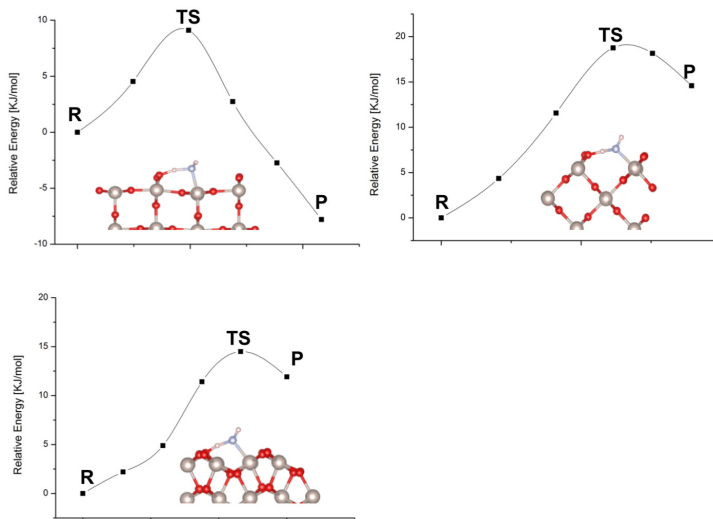the highest one corresponds to the less favorable one (the (001) surface).

Figure 4.3: Energy profiles associated to the water dissociation at low cover-
ages on the different surfaces.

In summary, at low water coverages ($\theta = 1/4$ and $1/8$), only the most stable
(110) surface exhibits dissociation. Differences are related to the surface topology
which influences the basicity of the O$_{br}$ on each surface (see the associated
DOS in Figure 4.2) and the interaction between the OH$^-$ and the unsaturated
ruthenium center. At higher coverages, however, cooperative H-bond interactions
could lower the energy requirements to decompose water on each orientation.

4.2.1   Water Adsorption at the Half Monolayer Coverage

Significant differences are observed upon adsorption of a second water molecule
to the (110), (100) and (001) surfaces or three additional water molecules to the
(011) surface. In all cases, the water coverage is $1/2$; that is, half of the initially
unsaturated ruthenium atoms have a water molecule adsorbed. For each surface
we explored at least three potential situations: i) adsorption of molecular water

molecules (*wat*/*wat*); ii) dissociation of half of the water molecules (*wat*/*dis*); and iii) adsorption of all dissociated water molecules (*dis*/*dis*). Furthermore, with the aim of evaluating the cooperative effects for the case of the (110) and (001) facets, we also explored the possibility that the water molecules adsorb in the two closest Ru-centers (-c) or in two Ru-centers that are further separated (-f). Relative energies for both molecular and dissociated forms, as well as major structural parameters are given in Table 4.2. Figure 4.4 shows the optimized geometries of the structures associated to the (110) surface and Figure 4.5 presents the most stable structures associated to the other facets.

First of all, we focus on the (110) surface. Here we explore the adsorption on adjacent Ru atoms as well as the adsorption on Ru centers separated by the O_{br} chain (distance between Ru centers is more than 6.3 Å). The adsorption of two water molecules on Ru_{5c} leads to an adsorption energy per water molecule that it is essentially equal to that computed for an isolated water molecule. The structural parameters are also very similar to those of the adsorption of a single water molecule and no H-bonding between the two water molecules is formed Figure 4.4-a. Similarly, the adsorption energy per water unit of two dissociated water molecules in two distant Ru_{5C} centers is essentially that of a single dissociated water molecule. Again, no hydrogen bonding between the two OH^-/H^+ motifs are formed. Finally, the adsorption of one molecular water and one dissociated leads to an adsorption energy per H_2O unit that is in between the adsorption energy of one wat and one dissociated water molecule as a result of the lack of cooperative effects.

Table 4.2: Water adsorption energies on the most favorable facets ($kJ \cdot mol^{-1}$) at half monolayer coverages $\theta = {}^2/_4$ or ${}^4/_8$, main structural parameters (in Å), and Bader atomic charges.

(hkl)		E_{ads}	Ru-Ru	O_{w1}-H_{w1}	O_{br}-H_{w1}	O_{br}-H_{w2}	Ru-O_{w1}	Ru-O_{w2}	O_{w1}-H_{w2}	$q_{O_{br}}$	$q_{H_2O}/q_{H_3O_2}$	q_{H+}
(1 1 0)	wat/wat-c[a]	-142.5	3.138	1.384	1.605	1.650	2.226	2.222	2.298	-0.796	0.086	
	wat/dis-c[a]	-151.3	3.149	1.920	0.999	1.846	2.044	2.198	1.739	-0.786 -1.066	-0.425	0.636
	dis/dis-c[a]	-149.6	3.139	1.864	1.005	1.009	2.002	2.002	2.234			
	wat/wat-f[b]	-131.7	3.139	1.864	1.005	1.009	2.002	2.002	2.234			
	wat/dis-f[b]	-139.2	6.427	1.765	1.010	1.606	1.996	2.181	-			
	dis/dis-f[b]	-143.0	6.426	1.782	1.008	1.007	1.990	1.989	-			
(0 1 1)	4wat	-126.7	3.666	0.974	1.022	3.035	2.097	2.202	1.463	-0.798 -1.068	0.078 -0.460	0.645
	2wat/2dis	-132.1	3.679	0.974	1.022	3.536	2.093	2.166	1.494	-0.786 -1.068	0.088 -0.448	0.639
	1wat/3dis	-127.5	3.674	0.975	1.023	3.530	2.092	2.207	1.481			
(1 0 0)	wat/wat	-128.3	3.144	1.007	1.711	1.676	2.204	2.204	2.346	-0.813	0.086	
	wat/dis	-127.1	3.069	1.603	1.044	2.233	2.073	2.179	1.717	-0.755 -1.082	-0.444	0.637
	dpro/dis	-112.9	3.081	0.977	1.016	1.023	2.012	2.027	2.275			
(0 0 1)	wat/wat-c[a]	126.2	4.554	0.975	1.535	1.711	2.186	2.168	-	-0.882	0.069	
	wat/dis-c[a]	-122.9	4.483	0.975	1.077	1.673	2.052	2.167	-	-0.822 -1.140	0.078	0.636
	wat/wat-f[b]	-122.4	6.402	1.039	1.519	1.643	2.185	2.165	2.952		0.078	0.636

(a) Water adsorption takes place in adjacent unsaturated ruthenium centers. (b) Water adsorption takes place in distant unsaturated ruthenium centers.
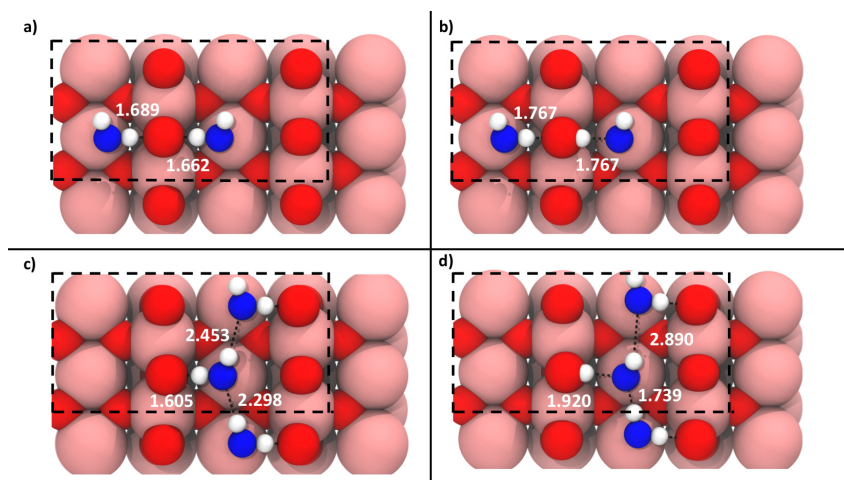
Figure 4.4: Optimized structures associated with water adsorption on the (110) surface with a half monolayer coverage.

The situation is completely different when the adsorption takes place on contiguous ruthenium centers (the distance between Ru centers in the pristine surface is 3.137 Å). The adsorption of two water molecules leads to an adsorption energy per water molecule of -142.5 $kJ \cdot mol^{-1}$, which is larger (in absolute value) than that determined for the adsorption of one water molecule (-131.3 $kJ \cdot mol^{-1}$). This indicates the presence of cooperative effects as a result of moderate hydrogen bond interactions between water molecules, the $H_{w1} \cdots O_{w2}$ distance being 2.298 Å (Figure 4.4-c). Note that the structural parameters associated with the $Ru \cdots H_2O$ interaction are similar to those of the isolated water and the subtle differences suggest that the interaction between the RuO_2 surface and the adsorbed molecules is weaker at higher coverages (larger $Ru_{5C} \cdots O_w$ and $O_{br} \cdots H_w$ distances). Similarly, the formation of two OH^-/H^+ species on contiguous Ru centers leads to an adsorption energy that it is also higher than that of one isolated OH^-/H^+ species (-149.6 vs. -131.7 $kJ \cdot mol^{-1}$). The origin of this extra stabilization arises again from the formation of moderate hydrogen bonding between OH^-/H^+ fragments (2.234 Å) rather than from a stronger interaction with the surface.

Finally, the situation in which one of the water molecules is dissociated and the other remains as molecular water results in the formation of a $H_3O_2^-$ species (Figure 4.4-d), with a strong intermolecular hydrogen bond (1.739 Å). In contrast, the H-bonding between the hydrogen atom of the OH^- fragment and the subsequent water molecule is significantly larger (2.890 Å). At this point it should be highlighted that, as already observed for the OH^-/H^+ form, formation of Ru-OH bond involves a significant electron donation from the formal OH^- to the RuO_2 surface that accumulates on the oxygen atoms of the surface and particularly at the O_{br}. Overall, the negative charge on O_{br} significantly increases and the Bader charge of the formal $H_3O_2^-$ unit is significantly smaller than -1. Nevertheless, we will hereafter refer to this motif as $H_3O_2^-$ species for simplicity, even though its charge indicates an intermediate situation. The adsorption energy of -151.3 $kJ \cdot mol^{-1}$ is larger than the adsorption of two water molecules, either in their molecular and dissociated forms. Overall, calculation suggest that the most stable configuration for a half monolayer in the (110) surface is *wat*/*dis*-c which encloses $H_3O_2^-$ dimers due to the strength of the cooperative effects as recently reported by Dohnálek and co-workers.[163,164]

The situation for the remaining surfaces is similar to that of the (110) facet, but with some particularities associated to the morphology of each surface. In the (011) facet, the contiguous unsaturated Ru_{5C} centers are still sufficiently close (3.731 Å in the clean surface) that cooperative effects between adsorbed water molecules, OH^-/H^+ species or combination of both are also present when four water molecules are adsorbed. This leads to an adsorption energy per water molecule that is higher than that of a single water (either in its molecular or dissociated forms). Interestingly, stronger cooperative effects are again found when the $H_2O_3^-$ dimer is formed (Figure 4.5-a). Because of that, structures such as 3*wat*/1*dis* or 4*dis* are not found as minima on the potential energy surface and evolve to 2*wat*/2*dis* and 1*wat*/3*dis* situations, respectively. Indeed, the gain achieved with the cooperative effects resulting from the formation of the $H_2O_3^-$ dimers are sufficient to compensate the 12.6 $kJ \cdot mol^{-1}$ preference for

the adsorption of molecular water with respect to water dissociation. Overall, the situation in which 50% of water molecules are dissociated is preferred by 5.4 $kJ \cdot mol^{-1}$.
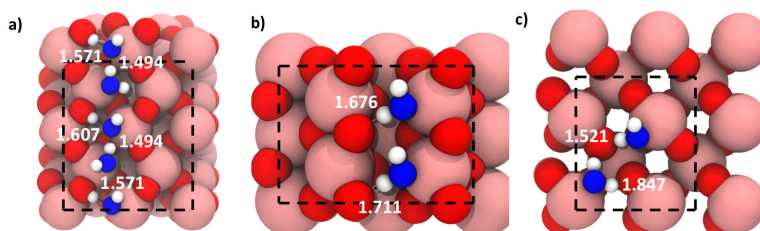

Figure 4.5: Optimized geometries of the most stable structures associated to water adsorption with a half monolayer coverage on the: a) (011), b) (100) and c) (001) surfaces. Distances are in Å.

In the (100) surface, the distance between close Ru_{5C} centers is also short (3.137 Å). Nevertheless, the surface morphology avoids the formation of moderate or strong H-bonds between water molecules and OH^-/H^+ moieties. This is a consequence of relative orientation of the $H_w \cdots O_{br}$ and $O_w \cdots H_{br}$ hydrogen bonds with respect to the adjacent water or OH^-/H^+ groups. As a consequence, the adsorption energies are essentially invariant to the increase of water coverage both for the 2*wat* and 2*dis* situations. Only for the case of the $H_2O_3^-$ dimer formation, cooperative effects appear to be relevant, but in this case, they are not sufficient to overcome the 14.7 $kJ \cdot mol^{-1}$ preference for the adsorption of molecular water. Overall, the 2*wat* structure is preferred (Figure 4.5-b) but both the 2*wat* and 1*wat*/1*dis* situations are very close in energy, the difference being less than 1.2 $kJ \cdot mol^{-1}$. This suggests that both situations would probably be present in this surface and the amount of dissociated water would be lower than 50%.

Finally, Ru_{5C} centers at the (001) surface are all separated by more than 4Å. Therefore, no cooperative effects can be established between water molecules, when coverage increases. Thus the preferred configuration is that in which the

two water molecules are adsorbed without dissociation as for the isolated water molecule. This turns in adsorption energies that are marginally lower than those of the isolated water molecule. Despite that we were able to find a structure in which at least one water molecule dissociates. However, this situation is 3.3 $kJ \cdot mol^{-1}$ less favorable than the adsorption of molecular water. Therefore, the degree of dissociation is predicted to be zero at the (001) surface, the most favorable structure being represented in Figure 4.5-c.

Overall, at half coverages $\theta = 2/4$ and regardless of the surface morphology, the preferred situation implies the adsorption of water molecules in contiguous Ru centers forming H-bond chains. The degree of water dissociation varies significantly as a function of the considered surface and this is largely controlled by the strength of the cooperative effects. In the (110) and (011) surface, morphology allows the formation of strong cooperative H-bonds, which results in the formation of chains constituted by $H_3O_2^-$ dimers leading to a high degree of dissociation (50 %). For the other facets, cooperative effects are weaker and the degree of dissociation tends to decrease. For instance, the preferred configuration for the (100) and (001) surfaces is the adsorption of water molecules (0 % dissociation), although the structure with 50 % of dissociated water is only marginally less favorable.

The stronger hydrogen bonding at 50 % of dissociation can be understood by analyzing the variation of the acid and basic strength of the resulting species when interacting with the surface. Adsorbed molecular water becomes more acidic when it interacts with Ru centers (positive Bader atomic charges), and more basic when it dissociates (the OH$^-$ fragment is negatively charged). Therefore, the interaction of one adsorbed molecule (acting as donor) with one OH$^-$ species (acting as an acceptor) forms a strong hydrogen bond, leading to the formation of the $H_3O_2^-$ dimer. The hydrogen bond is intermediate when the species involved are both water or OH$^-$ species since either the acceptor or the donor is not optimal. As expected, the worst situation is the interaction of an OH$^-$ group as a donor and a water molecule as acceptor, which leads to very long hydrogen

bonds. This behavior perfectly correlates with the observed trends in H-bonding distances shown in the appendix (Figure B.3 and B.4).

4.2.2 Water Adsorption at Monolayer Coverage

With the aim of analyzing the structure of water monolayer on each surface, we considered the adsorption of four water molecules per unit cell for the (110), (100) and (001) facets and eight water molecules in the (011) surface. Under these conditions, all unsaturated ruthenium centers of the surface are occupied by one water molecule. However, since the density of unsaturated atom on the surface varies depending on the considered facet, the number of water molecules is close to 5 per nm^2 in the (110) and (001) surfaces and between 7 and 8 for the (011) and (100) (Table 4.3). The first considered configuration for each facet was that with only adsorbed molecular water. From these structures successive water dissociations were explored. Table 4.3 reports the adsorption energies per water molecule, some selected distances, the Bader atomic charges and the adsorption energy per surface area (Å^2) of the most favorable degree of dissociation. The reference configuration consisting in a monolayer without any dissociation is added for comparison. Figure 4.6 shows the optimized geometry of the preferred structure in each facet. Further information on the structures and energetics of other configurations enclosing different water dissociation degrees can be found in Figure 4.7.

In general, the addition of water molecules to the most stable $\theta = 2/4$ coverage structures leads to the formation of a second water chain that is separated from the initial one by the presence of the O$_{br}$ chain. This results in a significant separation between the two water chains and thus, there is almost no interaction between water molecules of different chains. However, depending on the nature of the O$_{br}$, the facets can be divided into two groups. In the case of the (110), the O$_{br}$ atoms involved in the hydrogen bonding with the adsorbed water molecules are not bound to unsaturated Ru center and thus, the increase of water coverage has very little influence in the relative stabilities of the molecular and dissociated

adsorption modes. In contrast, for the other surfaces (011), (100) and (001), the O_{br} centers are directly bound to an unsaturated Ru atom that becomes the adsorption center of the additional water molecules. As a consequence, the adsorption energies and preferred structures are influenced by the increase of water coverage, favoring water dissociation.

In detail, the addition of two water molecules to the $\theta = 2/4$ coverage structures of the (110) leads to the formation of a second chain, which can be formed of either water molecules, $H_3O_2{}^-$ building blocks or OH^- groups, without any relevant interaction with the first chain. In this context, the water monolayer without any water dissociation corresponds to a structure formed by two parallel chains of water molecules and the corresponding adsorption energy per water molecule, albeit marginally smaller, is almost that of water adsorption without dissociation with the $\theta = 2/4$ coverage. The most favorable situation corresponds to the dissociation of two water molecules per unit cell (2−*dis*), one in each water chain, so that the resulting structure presents two parallel chains made of the formal $H_3O_2{}^-$ dimer as basic unit. Consequently, the adsorption energy per water molecule resembles that of a single chain of $H_3O_2{}^-$ species. Following the same argumentation, the structure with only one dissociated water molecule corresponds to the situation in which there are alternate water and $H_3O_2{}^-$ parallel chains and it has an adsorption energy per water molecule that is in between the adsorption energies of the two chains (water and $H_3O_2{}^-$) separately (-143.0 $kJ \cdot mol^{-1}$). Finally, the structure of three dissociated water molecules per unit cell, corresponds to two parallel chains: one has OH^- groups as building blocks and the other is formed by the $H_3O_2{}^-$ units. Results for the $\theta = 2/4$ coverage revealed that the chain with $(H_3O_2{}^-)_n$ is preferred over the chain formed by OH^- groups; therefore, the situation with three dissociated water molecules is less favorable than the formation of two $(H_3O_2{}^-)_n$ chains. Indeed, the associated adsorption energy per water molecule is again in between the values obtained for the two chains separately.

Table 4.3: Water adsorption energies on the main RuO$_2$ facets ($kJ \cdot mol^{-1}$) at monolayer coverages $\theta = {}^4/_4$ or ${}^8/_8$, the associated main structural parameters (in Å), and Bader charges (in au).

| (h k l)		ρ_{H_2O}	E_{ads}	$E_{ads/A}$	d($O_w - H_w$)	d($O_{br} - H_w$)	$\angle_{H_2O}$	d($Ru - O_w$)	d($O_w - Hw2$)	q_{Obr}	q_{H_2O}
(1 1 0) **2wat/2dis**	wat	4.96	-138.0	-685	0.981 1.031	1.728	105.9	2.231	2.281	-0.86	+0.08
	dis	4.96	-147.7	-733	0.973 1.524	0.995	106.7	2.131	1.689	-0.71^d -1.11^e	0.09^f $-0.40/+0.62^g$
(011) **4wat/4dis**	dis	7.97	-130.4	-1039	0.986 1.034	1.024	106.6	2.096	1.475	-1.00^d -0.751^e	0.09
(100) **3wat/1dis**	wat	7.92	-135.4	-950	0.980 1.018	1.587	105.4	2.176	2.245	-0.88	+0.08
	dis	7.92	-136.2	-615	0.984 1.039	1.458	101.1	2.193	2.396	-0.928	+0.07
(001) **3wat/1dis**	wat	4.84	-126.9	-615	0.984 1.039	1.458	101.1	2.193	2.396	-0.928	+0.07
	dis	4.84	-131.0	-635	0.975 1.568	1.036	109.4	2.133	1.965	–	$+0.09^f$ $-0.57/+0.64^g$
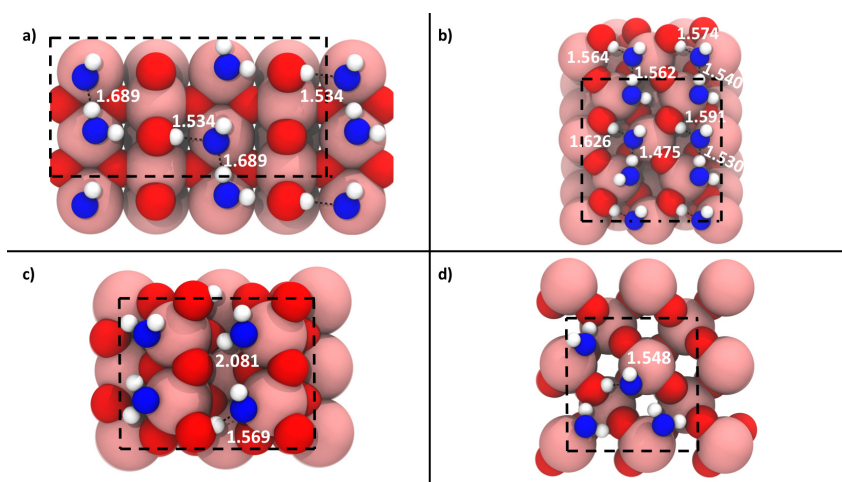
Figure 4.6: Optimized geometries of the most stable structures associated to water adsorption with monolayer coverage on the: a) (110), b) (011), c) (100) and d) (001) surfaces. Distances are in Å.

The situation is significantly different in the other surfaces. In the (011), (100) and (001) facets, the separating O$_{br}$ chain is formed by oxygen atoms bonded to the unsaturated Ru centers, and the increase of water coverage has an effect both on the adsorption energies and the degree of water dissociation. In this context, although there is not a direct interaction between the water molecules of different chains, the fact that the Ru center bonded to the O$_{br}$ acting as hydrogen-bond acceptor accommodates the adsorption of the additional water molecule produces an increase of the basicity of the O$_{br}$, which induces a decrease of the H$_w$···O$_{br}$ distance of about 0.01 Å and a marginally increase of the adsorption energy. The increase in the O$_{br}$ basicity also favors water dissociation, and thus, the amount of dissociated water tends to increase. These effects are very minor on the (011). The adsorption energy per water molecule on the (011) surface $\theta = 4/4$ coverages is very similar to that of the half monolayer coverage in this (011) facet. All our attempts to localize structures with higher and lower degrees of dissociation spontaneously evolved to structures with 4 water and 4 H$^+$/OH$^-$ units. Regarding the (100) facet, the adsorption energy increases 7.9 $kJ \cdot mol^{-1}$

with respect to the $\theta = 2/4$ situation and the associated global minimum presents 25% of dissociated water molecules instead of 0% as in the preferred structure of the half monolayer coverage. Finally, in the (001) facet, the preferred degree of dissociation is also 25% and the adsorption energy per water molecule increases from -126.2 $kJ \cdot mol^{-1}$ in the $\theta = 2/4$ to -130.0 $kJ \cdot mol^{-1}$ in $\theta = 4/4$.

Overall, when increasing the water coverage from the most stable structures of the half monolayer situation to the full monolayer, cooperative effects between water molecules remain unchanged. This is due to the formation of parallel water chains that are too far apart for forming hydrogen bonding interaction between them. However, the increase of O_{br} basicity due to the adsorption of water molecules in unsaturated Ru centers bonded to this O_{br} centers increases the degree of dissociation and/or the adsorption energy per water molecule in the (100) and (001) surfaces. The final amount of dissociated water in the monolayer is 50% in the (110) and (011) and 25% in the (100) and (001) surfaces. Trends in the degree of dissociation within the different facets is in good agreement with experimental results reported in a very recent contribution.[169] All these data were used to determine the most favorable coverage at different temperatures through *ab initio* thermodynamics (Figure B.5). Results show that from 0 to around 700 K the preferred coverage is the monolayer, and this is regardless of the surface. At around this temperature, water desorption begins, and it does not take place stepwise. Once the monolayer coverage becomes unfavorable, the preferred structure becomes the 0 coverage. Although the temperature of desorption may by too high, results suggest a general preference for the monolayer coverage.

At this point it is worth mentioning that while the adsorption energy per water molecule is an important descriptor for analyzing how strong is the interaction between water and RuO_2 in the interface, other factors are also key. In particular, the density of unsaturated Ru centers on the surface is significantly different in the four studied facets. In fact, the number of water molecules adsorbed per unit area is significantly higher in the (011) and (100) surfaces and thus, the adsorption energy per surface does not correlate with the strength of the

RuO_2-H_2O interaction of each particular water molecule (higher for the (110) surface). Indeed, considering the water density over the surface, the strongest water-RuO_2 surface interaction is observed in the (011) facet, followed by the (100). This suggest that these two surfaces will be the most stabilized ones in solution with respect with their surface energies in vacuum. As a consequence, these two surfaces would be the most favorable ones in pH conditions favoring neutral surfaces and they are expected to be predominant during crystal growth. Despite the limitations of the current approach, this suggest that the shapes of crystals or nanoparticles could be very different depending on the experimental conditions.
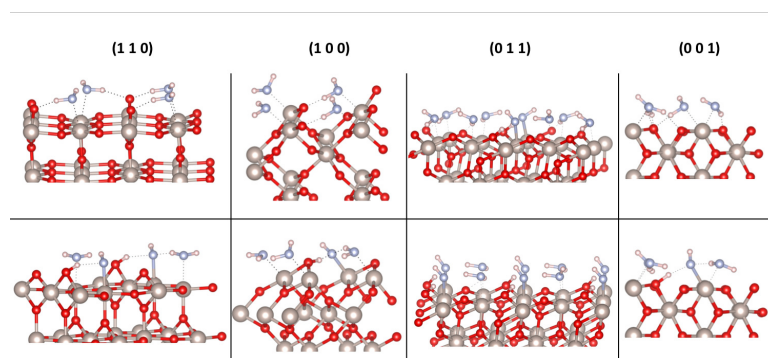

Figure 4.7: Optimized geometries of the reference and most stable structures associated with the adsorption of a monolayer of water on the main RuO_2 surfaces.

It is worth mentioning that adsorption energies including solvent effects through the implicit continuum model implemented in VASPsol[238] were also computed for single water and water monolayer coverages for the (110) and (100) surfaces (Table B.3). Results showed that the inclusion of solvent effects leads to a significant decrease of the global adsorption energy of a single water molecule by about 27 to 39 $kJ \cdot mol^{-1}$, the decrease being larger for the dissociated form. As a consequence, the preference for the dissociated form is reduced. Remarkably, for the monolayer coverage, solvent effects are similar for both the water and

dissociated structures, so that relative stabilities between them remain almost unaltered. Therefore, while the reported E_{ads} may be overestimated, we do not expect that including solvent effects through a continuum model will change the major trends.

Monolayer Ab Initio Molecular Dynamics

Thermal effects may modify the relative stability of above discussed configurations. Because of that, we have run NVT (AIMDs)[212,213] up to 8 ps (1ps equilibration) for the two surfaces with higher contribution on the Wulff Construction, (110) and (011), starting from the most stable monolayer obtained with static calculations. Structural analysis of H-bond distances corresponding to two interacting water molecules and those between these water molecules and O_{br} along the simulation as well as the $(Ru-O_w)$ distances and reported in Figure 4.8.
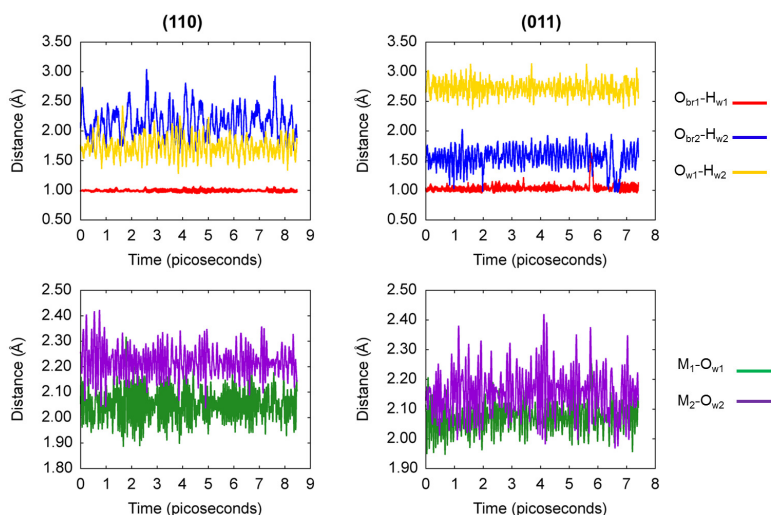

Figure 4.8: H-bond (Top) and $Ru-O$ (Bottom) distances of two neighbor water molecules in (Å) along the dynamics.

The frequency of each possible configuration, considering that proton transfer to an O_{br} occurs if the H-bond distance is smaller than 1.2 Å is summed up in Table 4.4. The most stable configurations of the (110) facet is 2*wat*/2*dis*, which

remains along the 7-8 ps of simulation. H-bond distances are consistent with the presence of H$_3$O$_2$$^-$ species and a protonated O$_{br}$ almost all along the simulation. Note that the frequency of the 2*wat*/2*dis* configuration is 99.9 % and only the 1*wat*/3*dis* arrangement appears in 0.1 %.

Table 4.4: Percentage of Configurations with Different Degree of Water Dissociation on the (110) and (011) Surfaces.

Surface	Structures	Dissociation Degree
(110)	4wat	0.0
	3wat / 1dis	0.0
	2wat / 2dis	99.9
	1wat / 3dis	0.1
	4dis	0.0
(011)	8wat	0.0
	7wat / 1dis	0.0
	6wat / 2dis	1.11
	5wat / 3dis	22.7
	4wat / 4dis	71.8
	3wat / 5dis	4.4
	2wat / 6dis	0.0
	1wat / 7dis	0.0
	8dis	0.0

Regarding the (011) surface, the 4*wat*/4*dis* is the most stable configuration from static calculations, and thus the most frequent arrangement 72% along the simulation. AIMD simulations shows that thermal effects tend to weaken the Ru-OH$_2$ interaction, thereby increasing the percentage of molecular water. However, during the simulation other percentage of water dissociation are observed. Indeed, although the 3*wat*/5*dis* represents about the 4% of configurations, structures with lower degrees of dissociation than the most stable 4*wat*/4*dis* isomer are more frequent, specially the 5*wat*/3*dis* which accounts for about 23% of representation.

4.3   RuO$_2$ Nanoparticles and H$_2$O Interaction

The previous section focused on the interaction between water and RuO$_2$ sur-
faces. This section addresses the water interaction with RuO$_2$ nanoparticles and
compares it with that obtained with the slab models. For that, the adsorption of
an isolated water molecule on different topological locations of the nanoparticle
surface has been carried out to determine the interaction strength and which is
the preferred adsorbed form, molecular water or dissociated. Both the Ru$_{33}$O$_{66}$
(1.20 nm) and Ru$_{51}$O$_{102}$ (1.80 nm) nanoparticles shown in chapter 3 have been
considered to analyze the water adsorption. At this point, it is worth noting that
present nanoparticles are Wulff like models, obtained from cutting the bulk and
cleaning up the excess of dangling oxygen atoms to achieve stoichiometry. This
has led to the presence of six singly coordinated oxygen atoms on the surface.
This situation is likely unstable and, indeed, for some metal oxides such as CeO$_2$,
metal reduction to avoid the presence of single coordinated species is likely more
favorable. Metal reduction, however, is not expected to occur for RuO$_2$ and, in
fact, Ru$-$O oxo species is the surface termination proposed in electrochemical
setups at potentials around 1.5 V. Thus, present study has been done with the
Wulff like stoichiometric models generated, without further modification.

Figure 4.9 shows the four different undercoordinated Ru sites on the nanoparticle
surface: Face, Corner, Tip and Edge. These sites exhibit different coordination
number, topological and electronic properties. Both Face and Corner sites consist
in a Ru$_{5C}$ metal center, which essentially corresponds to the (110) and (011)
surfaces matching the Wulff shape orientations. In contrast, Tip and Edge sites
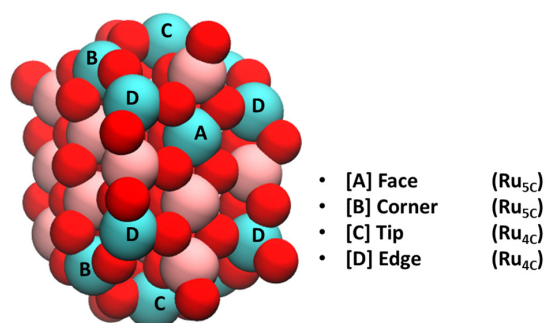consist in a Ru$_{4C}$ metal center.

Figure 4.9: Different locations present on the nanoparticle surface.

Table 4.5, shows the adsorption energies at different sites for the water molecule *wat* and dissociated *dis* forms, as well as the main geometrical parameters, and Figure 4.10 shows the optimized geometries. Regarding the *dis* form, we have explored the proton transfer to the closest non-dangling oxygens and included only the most stable one.

Table 4.5: Adsorption energies ($kJ \cdot mol^{-1}$) and structural parameters of water interaction on the 1.80 nm nanoparticle models.

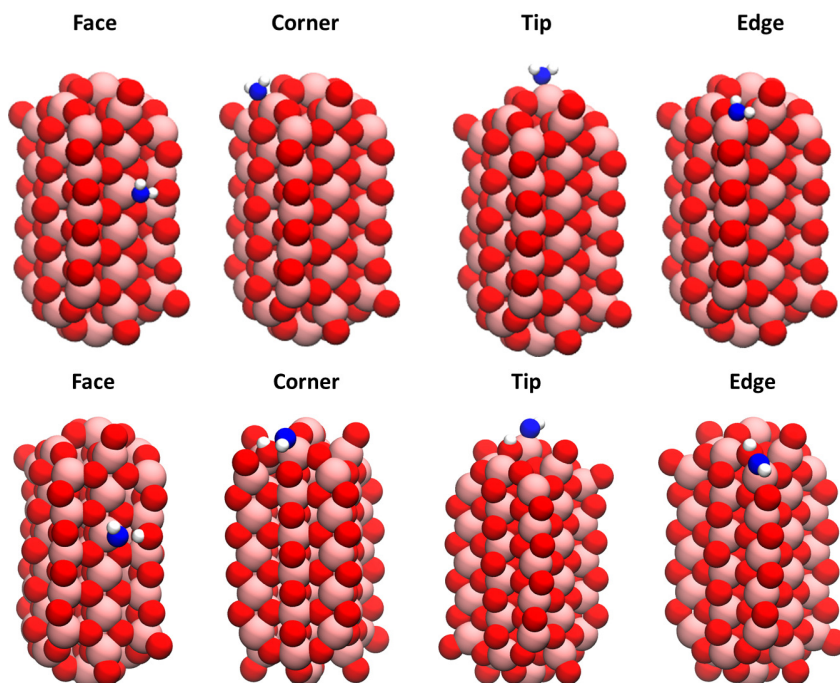| Site	Configuration	$\mathbf{E}_{ads}$	O_W-H_{W1}	O_W-H_{W2}	H_W-O_{NPS}	$Ru-O_W$	$\mu(\mathrm{Ru})$	$\mu(O_W)$
Face	*wat*	-131.2	0.974	1.043	1.558	2.162	0.00	0.00
	dis	-139.0	0.976	1.715	1.013	1.994	0.01	0.00
Corner	*wat*	-99.5	0.977	0.976	2.658	2.198	-0.14	0.00
	dis	-128.3	0.980	2.539	0.982	1.930	-0.09	-0.01
Tip	*wat*	-102.2	0.978	0.974	2.952	2.229	0.85	0.00
	dis	-124.2	0.983	2.737	0.976	1.895	0.00	0.00
Edge	*wat*	-94.6	0.977	0.981	2.383	2.206	0.15	0.00
	dis	-106.3	0.982	3.226	0.978	1.882	0.03	0.01

Figure 4.10: Adsorption of the *wat* and *dis* form on the different locations on the 1.80 nm model.

First of all, it can be observed that the adsorption energies at the Face site (-131.2 and -139.0 $kJ \cdot mol^{-1}$ for *wat* and *dis*, respectively) are essentially the same to those determined with the slab model for the (110) surface (-131.3 and -139.6 $kJ \cdot mol^{-1}$, respectively), the dissociated form being the most stable situation. This indicates that Lewis acidity of Ru atom and basicity of O_{br} do not change when going from the surface to the nanoparticle, which manifests itself in very similar geometrical parameters; i.e., The Ru−O distances for the *wat* and *dis* forms are 2.162 and 1.994 Å in the nanoparticle and 2.172 and 1.993 Å in the slab model.

In contrast, adsorption energies for the *wat* form on the other sites (Corner, Tip and Edge) are significantly smaller (adsorption energies range from -97 to 106 $kJ \cdot mol^{-1}$) since, due to the nanoparticle shape, adsorption does not

lead to H-bond interactions with surface O$_{br}$ atoms. Indeed, for these sites H$_W$−O$_{br}$ distances are now much larger (2.3-2.6 Å) than for the Face site (1.56 Å). Furthermore, the *dis* form arising from the transfer to the closest O$_{br}$ is more stable than the *wat* form. This is remarkable since one would expect Corner and Edge sites to behave similarly to those of the (011) surface and Tip sites to the (001) surface, for which previous simulations with slab models have indicated that the *dis* form is less stable than the *wat* one. This seems to suggest that Ru Lewis acidity and O$_{br}$ basicity are larger in the nanoparticle than in these surfaces. This is in agreement with the fact that Ru−O distances in the *dis* form at these sites are 0.10-0.13 Å smaller than on the (011) surface (see Table 4.1). Furthermore, projected density of states (pDOS) of the p orbitals of the O$_{br}$ site that receives the proton (Figure 4.11) also confirms that these oxygen atoms are more basic (the energy is higher) in the nanoparticle than at the surfaces (see Figure 4.2 for comparison). The formation of the *dis* form from the molecular adsorbed *wat* species is, however, expected to occur with a larger kinetic barrier than that found for the (110) facet (see Figure 4.3) due to the fact that now the O$_{br}$−O$_{br}$ distance is much larger.
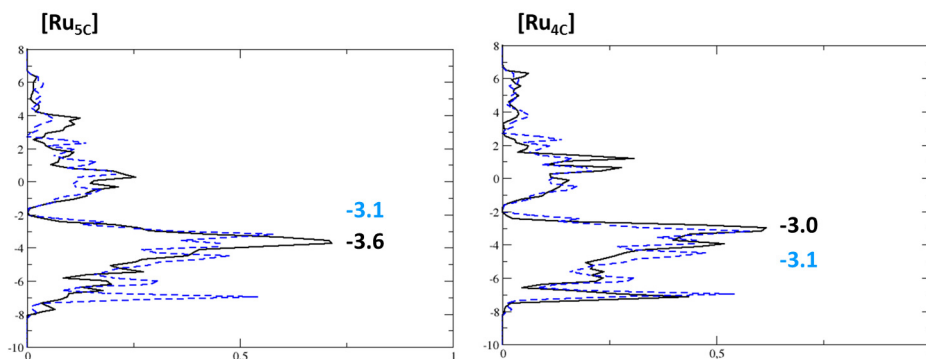

Figure 4.11: Projected density of states (pDOS) associated with the 2p orbitals of O$_{br}$ in the clean 1.80 nm nanoparticle. [Left] Face (solid black), Corner (dashed blue) and [Right] Tip (solid black), Edge (dashed blue).

Remarkably, for the Tip site, water adsorption reduces the magnetic moment from 0.85 to 0.00. It should be mentioned that we have located another *wat* adsorbed configuration at this site, in which the magnetic moment of the Ru atoms remains 0.85 as in the clean nanoparticle. This configuration shows, however, a smaller adsorption energy (-86.9 $kJ \cdot mol^{-1}$) and a significantly larger Ru$-$O distance (2.229 Å), thereby indicating that water interaction may largely change the electronic structure of RuO$_2$ nanoparticles.

The influence of the nanoparticle size has also been addressed by considering the water adsorption at the 1.20 nm nanoparticle (Figure B.6). The obtained results for the different sites with analogous chemical environments as those reported for the 1.80 nm are given also in the appendix (Table B.4). Results shows the same trends for the two nanoparticles, dissociation being favored at all sites, and adsorption energies differing by less than 0.2 eV.

Finally, we have considered the interaction of the water monolayer with the two nanoparticles. For that, all the undercoordinated Ru atoms of the nanoparticle surface were saturated with water molecules, O dangling bonds were OH termi-nated, and a 11 ps (1ps equilibration) NVT molecular dynamics simulation was carried out. Figure 4.12-a shows a snapshot of the full water monolayer coverage of the 1.80 nm nanoparticle model. The *wat* and *dis*-form are labeled as light and dark blue, respectively. One can observe that water molecules are disposed to maximize the formation of H-bonding interactions and that proton transfer processes have occurred. Such dissociation processes allow the formation of the H$_3$O$_2{}^-$ dimer motifs, which are very stable due to the cooperative effects described in the previous section for the main surfaces.
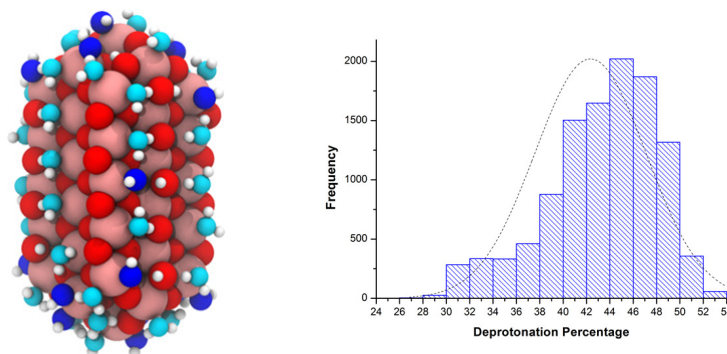
Figure 4.12: 1.80 nm nanoparticle model [a] Snapshot and [b] Deprotonation percentage along the MD simulation.

Figure 4.12-b shows the frequency of configurations with different degrees of dissociation, which ranges from 28% to 54%, the most frequent ones being 44 % and 46% of dissociation. Thus, the preferred monolayer configuration is not determined by water-surface interactions, which would suggest full dissociation, but by H-bond cooperative effects that are maximum when $H_3O_2^-$ motifs are formed.

4.4 Conclusions

RuO$_2$-Water interactions have been analyzed for the most relevant surfaces, (110), (011), (100) and (001), and for the Wulff like RuO$_2$ nanoparticles, with different water coverages that range from an isolated water molecule to a full monolayer.

Present results suggest that the water adsorption energy and the degree of dissociation are controlled by three main factors. The first one is the intrinsic acidity of the unsaturated ruthenium centers and the basicity of the O$_{br}$ groups in the pristine surface. The former increases when decreasing the coordination number of the ruthenium center. The latter is highly influenced by the energy levels of the p-orbitals of the O$_{br}$, which are related to the Ru$-$O$_{br}-$Ru angle.

This leads to the fact that dissociation at very low coverages is only favorable for the (110) surface. The second factor is the presence of cooperative effects between the adsorbed water molecules, which generates a chain of interaction species adsorbed on contiguous ruthenium centers. The usual preferred structure when cooperative effects are important is the formation of the formally ($H_3O_2^-$) unit that presents a strong internal hydrogen bond. Since the (110) surface is the flattest one and presents short distances between contiguous ruthenium centers, it also presents the strongest cooperative effects, maximizing a degree of dissociation of the 50%. In contrast, (001) surface, with the most separated Ru centers, presents the weakest cooperative effects, the weakest adsorption energies, and the smallest degree of dissociated water. Finally, it has been observed that O_{br} groups become more basic when additional water molecules to the half monolayer structures are adsorbed on Ru centers bonded to these O_{br} groups. This occurs at the highest coverages of the (011), (100) and (001) resulting in stronger adsorption energies and slightly higher water dissociation percentages when moving from the single chain of adsorbed water molecules to the monolayer. Furthermore, thermal effects seem to favor configurations with a smaller degree of dissociation because of an enlargement of Ru$-$O distances, which leads to a smaller increase of water acidity.

Interestingly, the density of unsaturated ruthenium centers in the different surface varies significantly, and thus, the interaction energies between water and RuO_2 per surface area, which are significantly higher for the (011) and (100) surfaces, do not correlate with the adsorption energies per water molecule (the interaction in the (110) surface is the strongest). As a consequence, nanoparticle shapes could vary significantly depending on the synthetic procedure (vacuum or solution). Since the strength of water adsorption and the degree of dissociation varies significantly as a function of the surface morphology, the synthesis of materials with one particular predominant face could tune the material properties and, ultimately, could have an influence in the catalytic processes.

Built RuO_2 nanoparticle models of different sizes (1.20 and 1.80 nm) have been

used to address the water adsorption and the dissociation process as a function of the surface location, nanoparticle size and water coverage. Results suggest that adsorption properties at the Face sites are very similar to those found for the main (110) RuO$_2$ surface, the dissociated form being the preferred adsorption situation. Molecular adsorption on the other sites (Corner, Tip and Edge) is significantly smaller due to the absence of H$-$O$_{br}$ interactions, and the dissociation form is always the most stable form. As found for main RuO$_2$ surfaces, (110) and (011), the degree of water dissociation of the monolayer interacting with nanoparticles is close to 50 % thereby indicating that H-bond cooperative effects leading to H$_3$O$_2{}^-$ motifs is the major driving force that determines the structure of the water interface.

Chapter 5

Oxygen Evolution Reaction

"CO_2 is the exhaling breath of our civilization, literally ... Changing that pattern requires a scope, a scale, a speed of change that is beyond what we have done in the past."

Al Gore

The following chapter presents the results obtained for the oxygen evolution reaction (OER). First, we will consider slab models of the main RuO_2 surfaces with the aim of determining which the most reactive crystallographic facet is, and secondly we will study this reaction on RuO_2 nanoparticles of different sizes, with the main goal of identifying the most reactive sites and compare their reactivity with that obtained with the slab models.

5.1 Introduction

In the last decades, a considerable effort has been devoted to identify versatile materials that allow the replacement of fossil fuels by non-carbon based ones. Renewable energy sources, for instance wind, tides, sunlight and geothermal are unlimited but also intermittent. As a consequence, due to nowadays large-scale power necessities, efficient methodologies to extract energy from no restricting provenance and its storage is required. Water splitting, as introduced in *Chapter 1*, can be understood as an artificial photosynthesis, where the energy is stored as molecular hydrogen, obtained through H_2O oxidation coupled with a proton reduction cell. Thus, an efficient catalyst able to oxidize water could be decisive to solve the current energetic problem and address the environmental greenhouse effect and air pollution. Oxygen Evolution Reaction (OER) is considered to be the bottleneck in the development of artificial solar fuel systems, requiring the presence of a water oxidation catalyst (WOC). Unfortunately, acidic media in the electrochemical water oxidation process gives rise to a substantial energy loss, due to high overpotentials at the anode semi-cell or undesired catalyst decompositions. Experiments have disclosed that metal oxide surfaces, in particular rutile-like oxides such as TiO_2,[239] RuO_2[240] and IrO_2[241] are considerable better as oxygen evolving electrodes in acidic conditions that others, RuO_2 being the most active one. Because of that this metal oxide is the one that has been chosen in the present thesis.

The catalyst activity for the oxygen evolution reaction catalyzed by RuO_2 has been extensively studied experimentally.[242–244] It is nowadays well accepted that RuO_2 is the most active catalyst in acidic conditions, but it suffers from its high cost and lower stability compared to IrO_2, for large and practical applications. Consequently, in recent years four main topics have been mainly addressed to overcome these limitations: i) characterization of intermediate species to elucidate the applying reaction mechanism; ii) determination of the different activities of RuO_2 monocrystals as a function of the exposed facets; iii) improvement of the

catalyst stability by synthesizing mixed materials, and iv) reduction of the catalyst cost by increasing the number of sites per gram of catalyst through the use of RuO_2 nanoparticles or ultimately Ru single atom catalysts.

Regarding the activity of the different facets, Shao-Horn and co-workers[242] have shown that the (001) and (100) surface presents the highest initial activities in terms of current produced at a fixed voltage. Interestingly, the decrease of this initial activity is different depending on the exposed surface. So that in subsequent catalytic tests, the most active surface may change.

Two mechanisms have been proposed for the electrochemical oxygen evolution reaction on metal oxide surfaces: i) the water nucleophilic attack (WNA) and ii) the oxocoupling (I2M) mechanism, the former one being the most commonly accepted. Both of them share the generation of M$-$OH and M$=$O species through proton coupled electron transfer (PCET) processes, the main difference arising from the formation of the O_2 species. That is, whereas the WNA mechanism involves the formation of the M$-$OOH intermediate which subsequently decomposes to O_2 (Figure 5.1-black), in the I2M mechanism, the O_2 is formed through the coupling of two oxo species (Figure 5.1-blue).
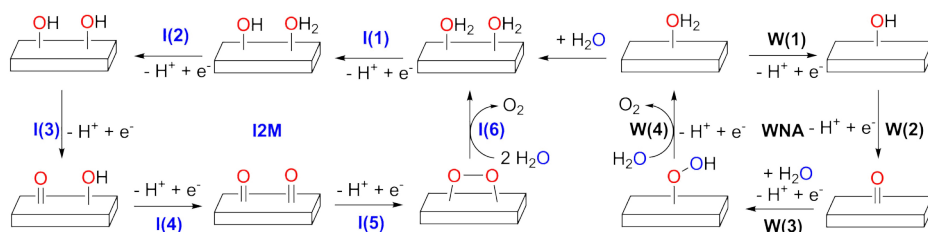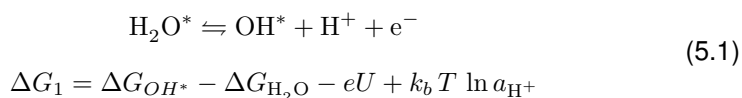

Figure 5.1: Oxygen evolution reaction both WNA (Black), I2M (Blue).

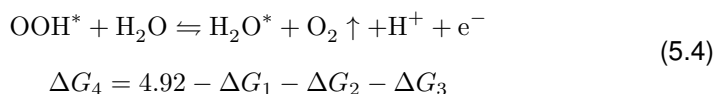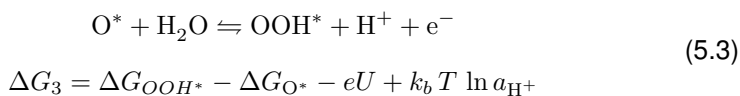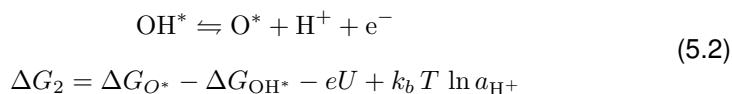Computational chemistry has been used to understand the system and propose the most likely reaction mechanism as well as descriptors for further catalyst design. In particular, Norskov[171,174] *et al.* have proposed the difference in adsorption energies of O* and OH* ($\Delta G_O - \Delta G_{OH}$), as a descriptor of the catalytic activity of a bunch of materials. This descriptor has been extensively

used to build a volcano plot, where the maximum corresponds to the most catalytically active material. Concerning the reaction mechanism, the majority of contributions have only explored the water nucleophilic attack pathway on the most stable (110) surface.[174,240,245] Nowadays, the first calculations were performed assuming spin non-polarized formalism, arguing that spin polarization has little influence. Nevertheless, recent contributions have suggested that the radical character of the OOH species is important for the catalyst activity.[246] In addition, the majority of contributions in the literature consider $Ru{=}O$ to $Ru{-}OOH$ conversion as a single step, even though it implies both the nucleophilic attack chemical process to form the $Ru{-}OOH/H$ species and a proton coupled electron transfer step that remove the $(H^+ + e^-)$ from the surface. Finally, it is also worth mentioning that, with the aim of avoiding the calculation of O_2, in many cases the energy of the $Ru{-}OOH + H_2O \rightarrow Ru{-}H_2O + O_2 \uparrow + (H^+ + e^-)$ is computed as the difference between the experimentally determined thermodynamics and the energy cost of the previous steps. Present thesis addresses both mechanisms for the most relevant RuO_2 surfaces and for two representative RuO_2 nanoparticles.

5.2   Water Nucleophilic Attack (WNA) Mechanism

Energetics of all steps involved in the WNA mechanism for each facet has been computed, at the PBE-D2 level of theory using both spin and non-spin polarized formalisms. Solvent effects were accounted for as implemented in the external VASPsol package for implicit solvation. Energy values are always given with respect to the most stable configuration. That is, for adsorbed H_2O, we have considered the molecular form for the (100), (011) and (001) surfaces and the dissociated one for the (110) surface. Gibbs free energies of the four proton coupled electron transfer processes are computed as follows:

$$H_2O^* \rightleftharpoons OH^* + H^+ + e^-$$

$$\Delta G_1 = \Delta G_{OH^*} - \Delta G_{H_2O} - eU + k_b T \ln a_{H^+}$$

(5.1)

$$\text{OH}^* \leftrightharpoons \text{O}^* + \text{H}^+ + \text{e}^-$$

$$\Delta G_2 = \Delta G_{O^*} - \Delta G_{\text{OH}^*} - eU + k_b\,T\,\ln a_{\text{H}^+} \tag{5.2}$$

$$\text{O}^* + \text{H}_2\text{O} \leftrightharpoons \text{OOH}^* + \text{H}^+ + \text{e}^-$$

$$\Delta G_3 = \Delta G_{OOH^*} - \Delta G_{O^*} - eU + k_b\,T\,\ln a_{\text{H}^+} \tag{5.3}$$

$$\text{OOH}^* + \text{H}_2\text{O} \leftrightharpoons \text{H}_2\text{O}^* + \text{O}_2 \uparrow + \text{H}^+ + \text{e}^-$$

$$\Delta G_4 = 4.92 - \Delta G_1 - \Delta G_2 - \Delta G_3 \tag{5.4}$$

Note tat ΔG_{O_2} is computed using the Gibbs energy of O_2 from the experimental ΔG value of the 2 $\text{H}_2\text{O} \rightarrow$ 2 $\text{H}_2 + \text{O}_2$ reaction, (4.92 eV) so that $\sum \Delta G_{1-4} = 4.92$ eV. This way we avoid the errors associated to the calculation of O_2 as usually done in the literature. Thermal corrections to Gibbs energies have been computed considering only the vibrational contribution of the adsorbed species from the harmonic frequencies. Furthermore, we have considered the following conditions (pH=0, T=298.15 K and U=0), since the overpotential and the potential determining step (PDS) do not depend on the pH or the applied potential values. Indeed, the required overpotential is the difference between the largest computed $\eta^{OER} = max\{\Delta G_{1-4}\}/e$ and 1.23 V. This value corresponds to one fourth of the Gibbs energy (4.92 eV). Moreover, adsorbate binding energies of the OER intermediates $\text{H}_2\text{O}*$, OH^*, O^* and OOH^* are calculated as shown in Eq. 5.5, where $G(*)$ represents the empty site where the catalytic cycle is performed.

$$\Delta G_{\text{OH}^*} = G(\text{OH}^*) - G(*) - (G_{\text{H}_2\text{O}} - {}^1\!/_2\,G_{\text{H}_2})$$

$$\Delta G_{\text{O}^*} = G(\text{O}^*) - G(*) - (G_{\text{H}_2\text{O}} - G_{\text{H}_2}) \tag{5.5}$$

$$\Delta G_{\text{OOH}^*} = G(\text{OOH}^*) - G(*) - (2\,G_{\text{H}_2\text{O}} - {}^3\!/_2\,G_{\text{H}_2})$$

Table 5.1 shows the spin-polarized Gibbs energies with (ΔG_{solv}) and without (ΔG) solvent effects. The ΔG values obtained with non-spin polarized approach (Table C.1) as well as the optimized structures (Figure C.1) are given in the appendix.

Table 5.1: ΔG_{solv} (ΔG) of WNA mechanism on each RuO$_2$ surface (in eV). Bold values correspond to the potential determinant step (PDS). Computed overpotential (η^{OER}) in Volts.

Step	Reaction	(110)	(100)	(011)	(001)
W(1)	$H_2O^* \rightarrow OH^* + (H^+ + e^-)$	1.27 (1.43)	1.40 (1.30)	**1.31 (1.25)**	0.92 (0.83)
W(2)	$OH^* \rightarrow O^* + (H^+ + e^-)$	1.40 **(1.59)**	1.49 **(1.46)**	1.18 (1.12)	1.37 (1.33)
W(3)	$O^* + H_2O \rightarrow OOH^* + (H^+ + e^-)$	**1.69** (1.04)	**1.52** (1.02)	-	**1.86 (1.48)**
W(4)	$OOH^* + H_2O \rightarrow H_2O^* + O_2 \uparrow$	0.56 (0.86)	0.52 (1.13)	-	1.05 (1.26)
η^{OER}		0.46 (0.36)	0.29 (0.23)	-	0.63 (0.25)

First of all, it should be noted that spin polarized calculation collapse to non-spin polarized solutions for the (011) surface, since computed magnetic moments are zero for all species and both energies are equal. In contrast, for (110), (100) and (001) magnetic moments show spin density at the adsorbed species and Ru atoms. This is particularly significant for the (110) surface for which magnetic moments can be as large as 0.6 in some cases (Table 5.2). This explains why differences between spin and non-spin polarized results are more pronounced (up to 0.18 eV) for this surface. At this point it is worth mentioning that while one would expect spin polarized results to be more accurate, radical species may also be over-stabilized with GGA methods, such as PBE, due to self-interaction error.[227,228,246] Nevertheless, since spin-polarized approach is expected to provide a more complete picture of the reaction, from now on, the discussion will be based on the values obtained with this formalism.

As mentioned, Ru surface sites in the (110) and (100) surfaces, are pentacoordinated and the vacant site is in the axial position. In contrast, in the (011) surface,

Ru site is pentacoordinated but the vacant site is equatorial, whereas in the (001) surface Ru is tetracoordinated and the two vacant positions are equatorial. This will influence the catalytic activity and thus, the discussion will be presented accordingly.

Table 5.2: Structural parameters of OER intermediates for the (110), (100), (011) and (001) surfaces (in Å).

Surface	Species	Ru$-$O$_{w1}$	O$_{w1}$$-H_w$	O$_{w1}$$-O_{w2}$	$\mu(O_{w1})$	$\mu(O_{w2})$	$\mu(Ru_1)$
(110)	H$_2$O-dis	1.989	0.976	-	0.05	-	-0.06
	OH*	1.934	0.982	-	0.08	-	0.34
	Ox*	1.729	-	-	0.20	-	0.19
	OOH*	1.953	2.003	1.373	0.28	0.19	0.10
(100)	H$_2$O-wat	2.186	1.013 - 0.976	-	0.00	-	-0.12
	OH*	1.917	0.983	-	-0.03	-	-0.11
	Ox*	1.723	-	-	0.00	-	0.05
	OOH*	1.937	1.913	1.396	0.02	-0.01	-0.08
(011)	H$_2$O-dis	2.177	0.975 - 1.022	-	0.00	0.00	0.00
	OH*	1.940	0.979	-	0.00	0.00	0.00
	Ox*	1.724	-	-	0.00	0.00	0.00
	OOH*	1.923	1.886	1.527	0.00	0.00	0.00
(001)	H$_2$O-wat	2.190	0.975 - 1.036	-	0.00	0.00	0.00
	OH*	1.915	0.984	-	0.00	0.00	0.00
	Ox*	1.716	-	-	0.00	0.00	0.00
	OOH*	1.878	1.936	1.424	0.00	0.00	0.00

For the (110) and (100) surfaces, the first three steps exhibit reaction energies that are higher than the ideal values, 1.23 eV. Among them, the potential determinant step in both cases is the water nucleophilic attack to the O* species **W(3)**, shown in Figure 5.2. Noteworthily, the high energy cost of this step arises from the PCET, since the chemical reaction involving the water nucleophilic attack leading to OOH and a proton to the surface oxygen bridge is thermodynamically easy $\Delta G =$0.55 and 0.36 eV, respectively. The fact that **W(3)** is computed to be the resting state is in agreement with what was previously reported in literature for

the (110). However, with our model, this step becomes the rate determining step only if continuum solvent effects are considered. Otherwise, the O^* formation **W(2)**, would be the less favorable step. The increase of the ΔG for **W(3)** upon considering solvent effects in mainly due to the stabilization of the incoming water and to the changes on the charges of the adsorbed species. Note that we formally go from an oxo species $Ru^{VI}-O^{2-}$ to a Ru^V-OOH^-. Indeed, the fact that changes in (110) are less pronounced than in (100), may be due to the fact that oxo species shows a larger radical character in the former case.
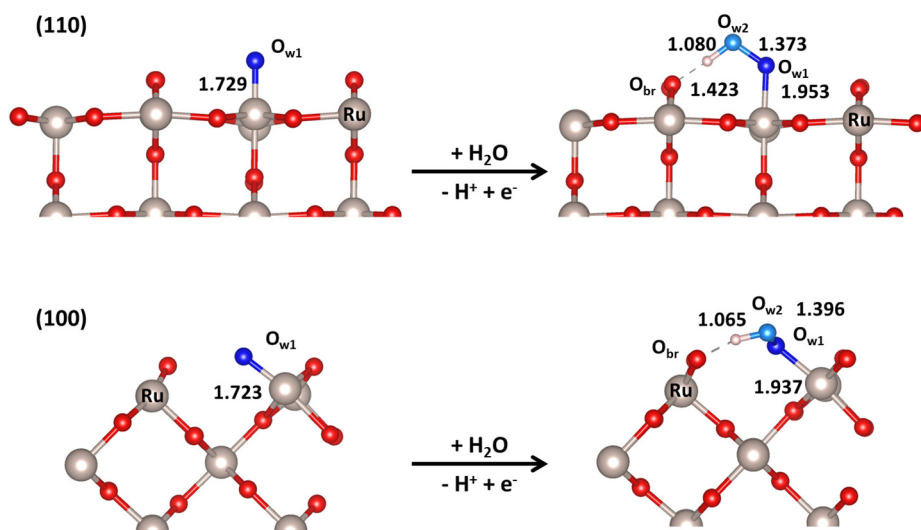

Figure 5.2: WNA mechanism on the oxo group O^* at the (110) and (100) RuO_2 surface.

For the (011) surface, the oxo formation appears to be easier than in previous surfaces. This is mainly because H_2O and OH are less adsorbed on this surface due to the equatorial nature of the vacant site, which for RuO_2 exhibits a larger distance due to bulk tetragonal compression. Indeed $Ru-O$ distances for adsorbed H_2O and OH are in general larger in the (011) surface than in (110) and (100), and adsorption energies smaller (see *Chapter 4*). Furthermore, formation of the OOH species is not achieved since the OOH species spontaneously

dissociates to O* + OH* adsorbed species. Thus, with this model, the reaction would proceed through the I2M mechanism. Such dissociation, however, would probably be prevented if close Ru undercoordinated sites already have additional adsorbed species. Indeed, if one considers a surface with the neighbor Ru atom O-terminated, the OOH species is found at 1.59 eV.

Finally, for the (001) surface, formation of both OH* and O* species is significantly easier than in the previous cases. Indeed, the oxo formation $(\Delta G_1 + \Delta G_2)$ is 2.3 eV in this case while on the other surfaces this value ranges from 2.5 to 2.9 eV. This is due to the tetracoordinated nature of Ru atom, which leads to stronger interactions with all species, particularly with O*, Ru$-$O distance being one among all surfaces. Consequently, the water nucleophilic attack on this surface is the most unfavorable. Indeed, although the chemical WNA appears feasible the ΔG for **W(3)** is computed to be 2.00 eV.

Figure 5.3-blue shows that the water nucleophilic attack is the potential determining step in all the cases where implicit solvation is included. The computed overpotential is 0.46, 0.29 and 0.63 V for the (110), (100) and (001), respectively. Thus, the (100) surface is the one that shows a larger catalytic activity. This is in agreement with recent experimental studies,[242] which suggest that the (100) is the more active one in comparison to the (011), (110) and (111) surfaces. In contrast, this is in disagreement with other experimental studies that includes the (001) surface being the most reactive one.[244] This, discrepancy may be due to the fact that we are using defect free surface model while surfaces considered in experiments present a root mean square roughness of 1 nm, thus suggesting the presence of some defects, caused by its partial dissolution in acidic conditions.
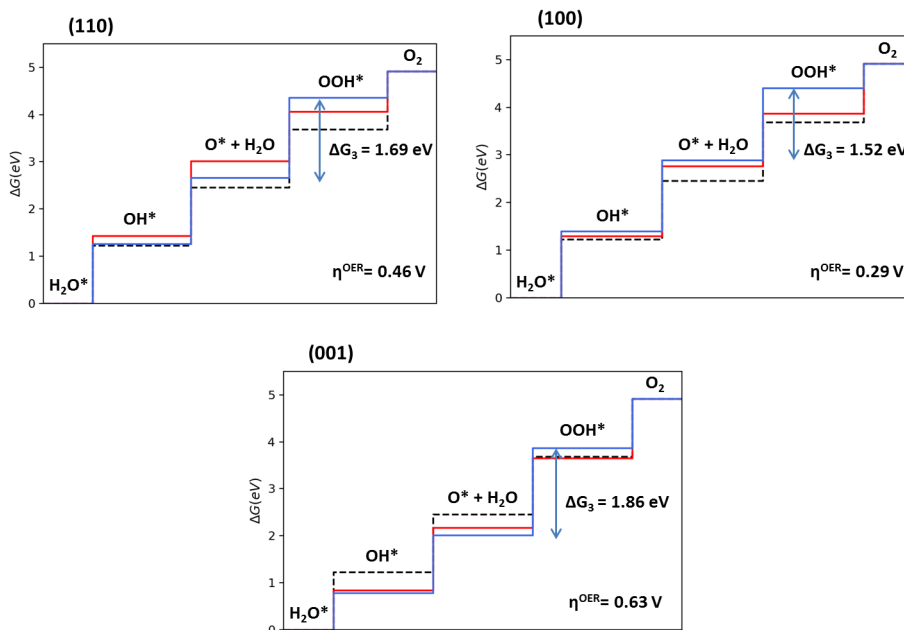
Figure 5.3: WNA mechanism profiles for the (110), (100) and (001) where: [Red] Profile in gas phase, [Blue] with implicit solvation and [Dashed Black] Ideal Catalyst. ΔG_3 as (PDS) and the computed overpotential (η^{OER}) are also given (with solvation effects).

5.3 Oxo-Coupling (I2M) Mechanism

The I2M mechanism (Figure 5.1-blue) starts with two water molecules adsorbed on vicinal undercoordinated ruthenium centers that evolve to the formation of two vicinal oxo species through four PCET processes. These electrochemical steps define the overpotential that has to be applied in the reaction. After that, two chemical steps take place, whose feasibility also determines the viability of the I2M route. This two chemical steps are associated with the homolytic coupling between two oxo species and the O_2 release. All optimized structures are given in (Figure C.2 to C.5).

Table 5.3: ΔG_{solv} (ΔG) of I2M mechanisms on each RuO_2 surface (in eV). Computed overpotential (η^{OER}) in Volts.

Step	Reaction	(110)	(100)	(011)	(001)^a
I(1)	$H_2O^* + H_2O^* \rightarrow OH^* + H_2O^* + (H^+ + e^-)$	1.24 (1.29)	1.25 (1.19)	1.00 (0.98)	0.91 (1.10)
I(2)	$OH^* + H_2O^* \rightarrow OH^* + OH^* + (H^+ + e^-)$	**1.42** (1.21)	**1.41** (1.35)	1.26 (1.27)	0.99 (1.25)
I(3)	$OH^* + OH^* \rightarrow O^* + OH^* + (H^+ + e^-)$	1.33 **(1.74)**	1.38 **(1.44)**	1.13 (1.25)	**1.52 (1.28)**
I(4)	$O^* + OH^* \rightarrow O^* + O^* + (H^+ + e^-)$	1.34 (1.36)	1.31 (1.28)	**1.31 (1.32)**	1.19 (1.26)
I(5)	$O^* + O^* \rightarrow O{-}O^*$	0.79 (0.65)	1.30 (1.23)	0.78 (0.74)	0.71 (0.76)
I(6)	$O{-}O^* + 2H_2O \rightarrow H_2O^* + H_2O^* + O_2 \uparrow$	-1.20 (-1.32)	-1.74 (-1.56)	-0.56 (-0.53)	-0.40 (-0.73)
η^{OER}		0.19 (0.51)	0.18 (0.21)	0.08 (0.10)	0.29 (0.05)

a) Oxo-coupling takes place at the same Ru_{4C} atom

Table 5.3 shows the energetics of all steps for each facet. Again, results with and without considering solvent effects are included for comparison (ΔG_{solv} and ΔG). All energies are referred with respect to the most stable conformation of the two adsorbed water molecules. As already described in *Chapter 5*, the most favorable configuration is the formation of the $H_3O_2^-$ dimer and a protonated oxygen bridge on the (110) and (011) surfaces and the adsorption of two water molecules for the other two surfaces ((100) and (001)). Therefore, the origin of energies is face dependent. Results will be presented following the same structure than in the previous section based on the nature of the Ru center. We will focus first on the (110) and (100) surfaces, then on the (011) and finally on the (001) surface.

Table 5.4: OER intermediates adsorption energies (in eV).

Species	(110)	(100)	(011)	(001)
H_2O^*	-1.08	-1.10	-1.02	-1.01
OH^*	0.18	0.30	0.29	-0.23
O^*	1.58	1.79	1.40	1.00
OOH^*	3.27	3.30	-	2.86

Computed as shown in Eq. 5.5.

The undercoordinated ruthenium centers on the (110) and (100) are pentacoordi-
nated with a vacant site in axial position. This leads to stronger H_2O adsorption
energies when compared to the (011) or (001) surfaces (see Table 5.4) with an
equatorial vacant site, but less stabilized oxo groups. As a consequence, calcula-
tions predict that the formation of oxo species is more energetically demanding
in the (110) and (100) surface than in the other two facets when considering the
adsorption of a single water molecule. This behavior is also found when two water
molecules are adsorbed, the reaction energy associated to the formation of the
two oxo groups being 5.3 eV for the (110) and (100) surfaces and 4.6 - 4.7 eV for
the (011) and (001). As a consequence, the formation of two vicinal oxo species
requires overcoming four PCET, the computed energy of each being higher than
the ideal value (1.23 eV) and the overpotential is 0.19 and 0.18 V for the (110)
and (100), respectively. The computed values for the individual steps, albeit being
generally lower, resemble those computed for a single water molecule, the small
deviation arising from a subtle balance between the loss of hydrogen bonding in
each PCET and the increase of the interaction with the surface, which becomes
stronger when hydrogen bonds between adsorbed molecules disappear (see
Table 5.5).

Table 5.5: Structural parameters of I2M intermediates on (110), (100), (011) and (001) surfaces (in Å).

Surfaces	Species	$Ru-O_w$	$O_{w1}-H_w$	$O_{w2}-H_w$	$O_{w1}-H_{w2}$	$O_{w1}-O_{w2}$	Ru_1-Ru_2
(110)	$OH-H_2O$	1.973 - 2.196	0.975	1.008 - 1.004	1.759	2.727	3.146
	$OH-OH$	1.941 - 1.936	0.983	0.985	2.309	3.181	3.138
	$Ox-H_2O$	1.754 - 2.185	-	0.998 - 1.001	1.835	2.778	3.145
	$Ox-OH$	1.739 - 1.910	-	0.991	1.945	3.424	3.137
	$Ox-Ox$	1.717 - 1.716	-	-	-	3.135	3.137
	Ox-Bridge	2.070 - 2.067	-	-	-	1.346	3.043
(100)	$OH-H_2O$	1.939 - 2.215	0.982	1.002 - 0.980	2.615	3.421	3.145
	$OH-OH$	1.934 - 1.934	0.985	0.985	2.273	3.138	3.138
	$Ox-H_2O$	1.730 - 2.207	-	0.999 - 0.978	-	3.422	3.158
	$Ox-OH$	1.721 - 1.896	-	0.990	-	3.280	3.142
	$Ox-Ox$	1.708 - 1.709	-	-	-	3.139	3.137
	Ox-Bridge	2.059 - 2.059	-	-	-	1.343	2.998
(011)	$OH-H_2O$	2.046 - 2.140	0.975	0.975 - 1.077	1.446	2.511	3.631
	$OH-OH$	1.986 - 1.900	0.976	1.01	1.724	2.699	3.626
	$Ox-H_2O$	1.769 - 2.181	-	0.977 - 1.011	1.738	2.718	3.601
	$Ox-OH$	1.744 - 1.919	-	0.989	2.044	2.930	3.600
	$Ox-Ox$	1.722 - 1.725	-	-	-	2.944	3.582
	Ox-Bridge	1.996 - 2.021	-	-	-	1.372	3.544
$(001)^a$	$OH-H_2O$	1.925 - 2.186	0.985	0.998 - 1.00	-	2.833	4.477
	$OH-OH$	1.926 - 1.926	0.986	0.985	-	2.578	4.553
	$Ox-H_2O$	1.742 - 2.183	-	1.009	-	2.852	4.406
	$Ox-OH$	1.720 - 1.901	-	0.994	-	2.852	4.453
	$Ox-Ox$	1.734 - 1.734	-	-	-	2.808	4.562
	Ox-Bridge	1.969 - 1.969	-	-	-	1.398	4.558

a) I2M intermediates on the (001) are adsorbed in one Ru site

The chemical steps present very different reaction energies. The O_2 displacement by two H_2O molecules is extremely favorable (ΔG = -115.8 $kJ \cdot mol^{-1}$ for the (110) and -167.9 $kJ \cdot mol^{-1}$ for the (100)) and this is mainly due to the strong interaction between water and the surface, when compared to that between O_2 superoxide and RuO_2. In contrast, the oxo-coupling process (Figure 5.4) is energetically demanding with a reaction energy of 72.6 $kJ \cdot mol^{-1}$ and 118.9 $kJ \cdot mol^{-1}$ for the (110) and (100) surfaces, respectively. This high reaction energy suggests that although the electrochemical steps are at least as favorable

as those computed for the WNA mechanism, the I2M mechanism is strongly disfavored due to the oxo coupling. Indeed, a potential WNA on one of the two vicinal oxo intermediates is computed to be significantly easier ($\Delta G =0.032$ eV) than the oxo coupling both in the (110) and (100) surfaces, suggesting that the oxo species on the (110) and (100) surfaces will preferentially proceed through WNA in contact with a water solution.
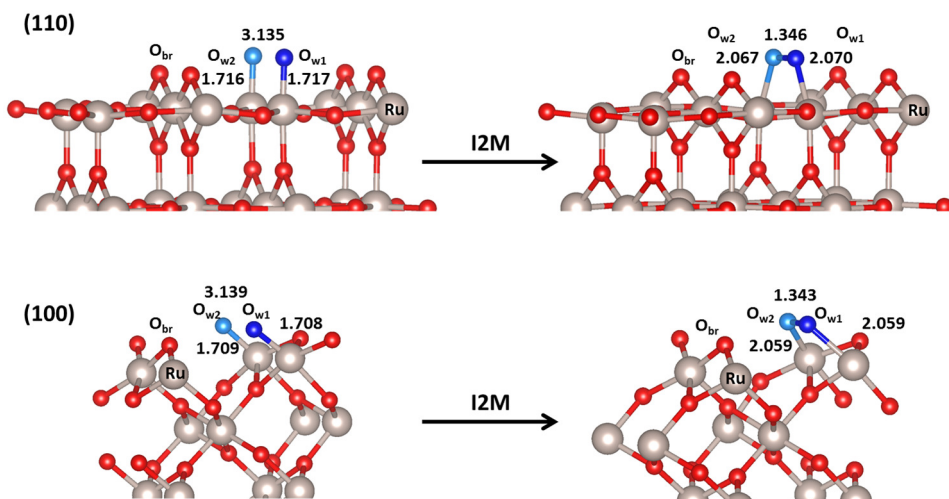

Figure 5.4: Oxo-coupling (I2M) process on (110) and (100) surfaces.

Similarly to the (110) and (100) surfaces, the electrochemical steps leading to the formation of two vicinal oxo species on the (011) resemble those computed with a single water molecule. The potential determining step is the formation of the second oxo group from adsorbed OH and the associated overpotential is 0.08 V. This value is smaller than that computed for the (110) and (100) surfaces, as a result of the weaker intrinsic interaction of water with the surface and the stronger intrinsic interaction of the oxo (see Table 5.4), which makes oxo formation much more favorable. Noticeably, the oxo coupling is again challenging, the computed reaction energy being 75.3 $kJ \cdot mol^{-1}$. Thus, although the subsequent O_2 release is extremely easy, the computed data suggest again that the I2M mechanism is unlikely.

The reaction on the (001) has some particularities that merit to be mentioned. As a result of the stronger interaction between the unsaturated tetracoordinated ruthenium centers and the oxo ligand, the formation of the two oxo ligands in vicinal unsaturated ruthenium centers of the (001) surface is the least energetically demanding. However, the two formed oxo groups are very distant and this large separation between vicinal ruthenium centers, more than 4 Å (Table 5.5), makes the oxo coupling very challenging ($\Delta G = 135.1\ kJ \cdot mol^{-1}$). Taking into account that superficial ruthenium centers are tetracoordinated, we explored the possibility to form two oxo species on the same metal center and then explore their coupling. The computed values for the bis-oxo formation do not differ significantly with the formation of two oxo in vicinal centers, suggesting that at reaction conditions the bis-oxo complex is feasible, shown in Figure 5.5. The fact that the two oxo groups are now very close (2.94 Å) makes the coupling easier, the final reaction energy being ΔG=68.1 $kJ \cdot mol^{-1}$ which is the lowest values for all computed oxo coupling steps. However, 68.1 $kJ \cdot mol^{-1}$ is still quite high so that the I2M mechanism is not expected to apply in this surface neither.
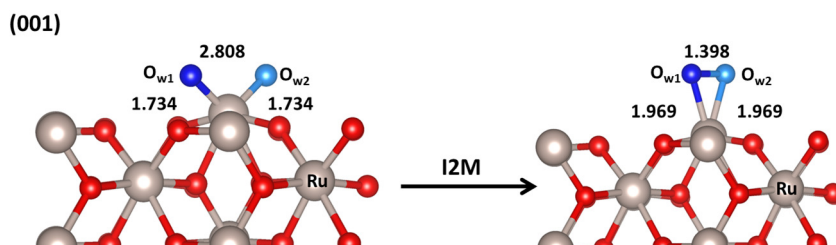

Figure 5.5: Oxo-coupling (I2M) process on (001) surface on one Ru site.

Overall, the I2M mechanism appears to be unlikely in all considered surfaces. This is mainly due to a strongly disfavored oxo coupling with respect to the WNA on the same species. These results are in agreement with the conclusions drawn by Goddard and co-workers[247] on IrO$_2$ (110) surface. Trends observed between the different oxo coupling processes as a function of the surface can be related to the Ru−Ru distance, the larger the distance the less favorable it becomes.

Figure 5.6 summarizes the energetics of the I2M mechanism on each surface, colored from lightblue to red as a function of the ΔG associated to the $O^* + O^* \rightarrow O{-}O^*$ step. Overall, (001) surface is the least energetically demanding, followed by the (011) surface, whereas the (110) and (100) surfaces are the most demanding ones.
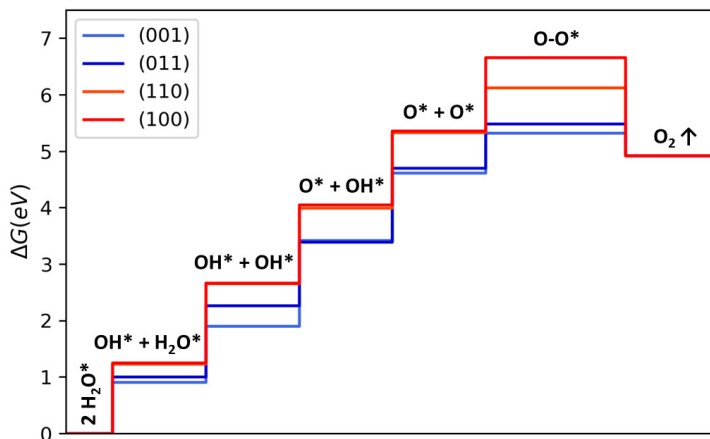

Figure 5.6: I2M mechanism profiles for the (001), (011), (110) and (100) as lightblue, blue, orange and red (in solvent conditions).

The study of the two proposed reaction mechanisms suggest that the applying one in RuO_2 surfaces is the water nucleophilic attack as generally accepted in the literature. This is the most favorable mechanism regardless of the surface and the presence or absence of vicinal oxo species. The computed overpotentials are those of the WNA mechanism and vary from 0.21 V for the (110) to 0.29 V for the (100) and 0.77 V for the (001) when the solvent effects are taken into account. As already mentioned, this does not allow to understand while the (001) surface shows the higher activity at 1.6 V voltages, but this disagreement may be associated to the presence of defects that could facilitate the reaction, something that has been recently pointed out by Norskov and co-workers.[171,174] Indeed, the experimentally measured roughness of the materials employed in the catalysis test is quite large.[248]

5.4 OER on RuO$_2$ Nanoparticles

At this point, we decided to explore if RuO$_2$ nanoparticles increase or decrease the overpotential that has to be applied to make the oxygen evolution reaction to occur, with the aim of evaluating if, in addition to the economic benefit of having a large percentage of active centers per gram of material, the use of nanoparticles also leads to more active catalysts. For that we considered the WNA mechanism on the four different sites of the two nanoparticle models considered in *Chapter 4*: the Face, Corner, Tip and Edge positions of the 1.80 and 1.20 nm nanoparticles. For the shake of completeness, in the case of the face sites, we also considered the I2M mechanism to ensure that the oxo coupling is also challenging on the nanoparticles. Reaction energies for the 1.80 nm (1.20 nm) models are given in Table 5.6 and optimized structures in Figure C.6 (Figure C.7), respectively.

Table 5.6: ΔG of WNA mechanism on RuO$_2$ 1.80 nm (1.20 nm) nanoparticles on each location (in eV). Computed overpotential (η^{OER}) in Volts.

Step	Reaction	Face	Corner	Tip	Edge
W(1)	H$_2$O* → OH* + (H$^+$ + e$^-$)	1.23 (1.40)	0.95 (0.96)	0.63 (0.83)	0.97 (0.86)
W(2)	OH* → O* + (H$^+$ + e$^-$)	1.32 (1.27)	1.25 (1.25)	1.36 (0.79)	1.13 (1.14)
W(3)	O* + H$_2$O → OOH* + (H$^+$ + e$^-$)	**1.42 (1.49)**	**1.73 (1.64)**	**2.00 (2.09)**	**1.94 (1.65)**
W(4)	OOH* + H$_2$O → H$_2$O* + O$_2$ ↑	0.95 (0.59)	1.11 (1.07)	0.93 (1.21)	0.88 (1.27)
η^{OER}		0.19 (0.26)	0.50 (0.41)	0.77 (0.86)	0.71 (0.42)

Results show that the energetics on the Face location is similar to that obtained with the slab model of the (110) surface. However, Corner, Edge and Tip sites show significant differences. First, ΔG value for the first PCET process is much larger on the Face site that on the other sites, due to the presence of a H-bond interaction between the protonated O$_{br}$ and OH in former case. Secondly, the formation of the O* species appears to be more favorable on the Edge and Corner sites than on the Face and Tip sites, the reaction Gibbs energy being 1.13, 1.25 and 1.32, 1.36 eV, respectively. This can be associated to the larger oxygen

adsorption energy, particularly at the Ru_{4C} Edge and Tip sites (Table 5.7).

Table 5.7: Adsorption energies on 1.80 nm (1.20 nm) NPS sites (in eV).

Species	Face	Corner	Tip	Edge
H_2O^*	-1.52 (-1.49)	-0.87 (-1.09)	-1.37 (-1.07)	-1.28 (-1.17)
OH^*	-0.29 (-0.09)	-0.04 (-0.14)	-0.74 (-0.25)	-0.32 (-0.32)
O^*	1.04 (1.18)	1.14 (1.12)	0.62 (0.55)	0.81 (0.23)
OOH^*	2.46 (2.66)	2.80 (2.75)	2.62 (2.64)	2.75 (2.48)

Computed as shown in Eq. 5.5.

Indeed, Ru−O distances of the O^* species at these sites are shorter than at the pentacoordinated Face and Corner sites (Table 5.8). Consequently, the water nucleophilic attack, which in all cases is the potential determining step, has larger ΔG values at the Edge and Tip sites. The computed overpotentials are 0.19, 0.50, 0.77 and 0.71 V at the Face, Corner, Tip and Edge sites, respectively, which indicates that the larger catalytic activity occurs on the Face location (see Figure 5.7).

Table 5.8: Structural parameters of OER intermediates for the 1.80 nm (1.20 nm) nanoparticle models (in Å).

Site	Species	$Ru-O_{w1}$	$O_{w1}-H_w$	$O_{w1}-O_{w2}$
Face	OH^*	1.934 (1.930)	0.978 (0.980)	-
Face	Ox^*	1.737 (1.740)	-	-
Face	OOH^*	1.927 (1.915)	1.899 (1.883)	1.456 (1.454)
Corner	OH^*	1.917 (1.911)	0.983 (0.980)	-
Corner	Ox^*	1.714 (1.724)	-	-
Corner	OOH^*	1.903 (1.886)	1.881 (1.879)	1.446 (1.459)
Tip	OH^*	1.898 (1.897)	0.987 (0.983)	-
Tip	Ox^*	1.709 (1.704)	-	-
Tip	OOH^*	1.891 (1.866)	1.887 (1.877)	1.445 (1.462)
Edge	OH^*	1.913 (1.923)	0.980 (0.979)	-
Edge	Ox^*	1.687 (1.714)	-	-
Edge	OOH^*	1.917 (1.893)	1.878 (1.912)	1.453 (1.465)

(∗) Structural parameters for H_2O^* are the same for the *dis*-form (*Chapter 3*).

d(Ru-O$_{w1}$): 1.739   d(Ru-O$_{w1}$): 1.915, d(O$_{w1}$-O$_{w2}$): 1.454
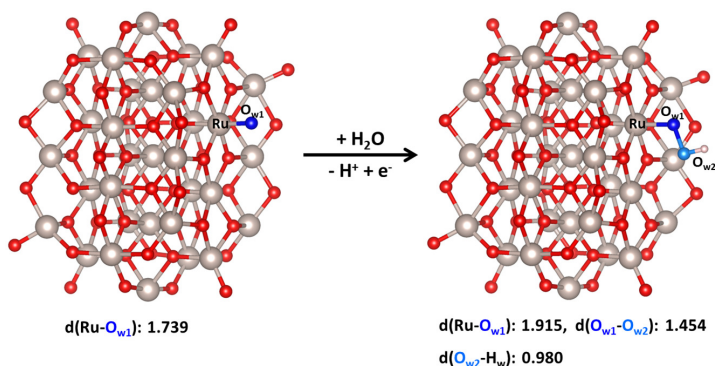
d(O$_{w2}$-H$_w$): 0.980

Figure 5.7: WNA step on the 1.20 nm nanoparticle at Face location.

Regarding the I2M mechanism on the nanoparticle surface, the homo-coupling step on the Face location (Figure 5.8) starts with two O* oxo groups adsorbed on Ru$_{5C}$ active sites leading to the formation of a O$-$O bond ($\Delta G = 0.36$ eV). The reaction energy is decreased on the nanoparticle surface by 0.24 eV compared to the same step on the (110) and (100) surfaces. Such decrease is attributed to a larger flexibility of the nanoparticles compared to the slab model stiffness. Indeed, while upon O$_2$ formation the Ru$-$Ru distance only decreases 0.1 Å (from 3.14 to 3.04 Å) on the slab model, this variation is significantly larger on the nanoparticle (from 3.12 to 2.53 Å). Therefore, although it is still less favorable than the WNA, the oxo-coupling reaction starts being competitive in the nanoparticle surface.

d(Ru-O$_{w1}$): 1.742, d(Ru-O$_{w2}$): 1.745,   d(Ru-O$_{w1}$): 2.02, d(Ru-O$_{w2}$): 2.02

d(O$_{w1}$-O$_{w2}$): 3.258   d(O$_{w1}$-O$_{w2}$): 1.379
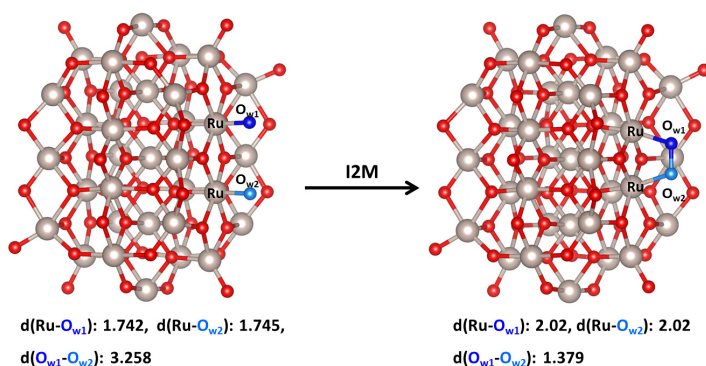
Figure 5.8: Oxocoupling step on the 1.20 nm nanoparticle at Face location.

In general, nanoparticle catalysts increases the number of active sites per gram of material but does not seem to improve the catalytic activity compared to the surface. The computed overpotentials are higher than those obtained for the surfaces and the oxo-coupling reaction, which was determined to be very unfavorable (around 70-80 $kJ \cdot mol^{-1}$) on the surface, becomes much less energetically demanding (35 $kJ \cdot mol^{-1}$) on the nanoparticle.

Figure 5.9 summarizes the energetics of the WNA mechanism on each 1.80 nm nanoparticle location, colored from lightblue to red as a function of the ΔG associated to the water nucleophilic attack **W(3)** step. The Face location is the least energetically demanding, followed by the Corner one, whereas the Edge and Tip surfaces are the most demanding ones.
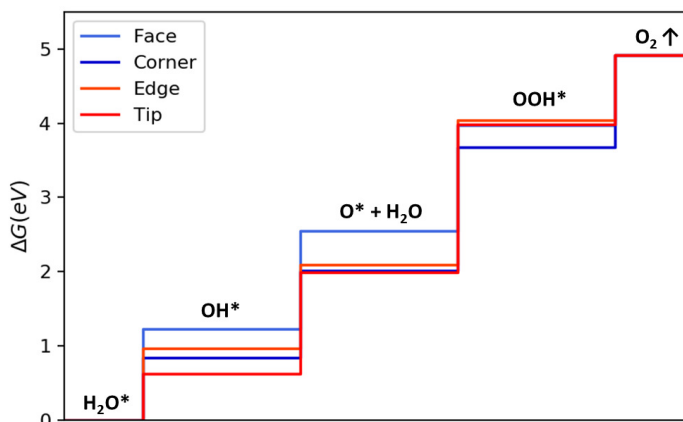
Figure 5.9: WNA mechanism profiles for the 1.80 nm nanoparticle on each site: Face (lightblue), Corner (blue), Edge (orange), Tip (red).

5.5   Conclusions

Figuring out the catalytic performance of the most relevant RuO_2 surfaces and nanoparticles on oxygen evolution reaction (OER) is important to characterize the different reaction intermediates as a function of the catalyst and the active site nature. This has been addressed through *ab initio* computational methodologies on two OER mechanisms, i) the water nucleophilic attack (WNA) and ii) the oxo-coupling mechanism (I2M). In this context, we analyzed the influence of the OER adsorbed intermediates OH^*, O^* and OOH^* stability as a function of the Ru site. For that, we considered the four most relevant stoichiometric non-polar surfaces (110), (100), (011) and (001) as well as two nanoparticle sizes considering four differential locations available on their surface known as Face, Corner, Tip and Edge.

Present results suggest that the OER performance is controlled by many factors. The first factor is related with the potential determinant step (PDS) which in general has been shown to be the formation of the OOH^* intermediate through the WNA mechanism. The latter is highly influenced by the adsorption energy of the adsorbed oxo-group O^* which is well correlated with the OER activity. In contrast, the potential determinant step on the I2M mechanism is the formation of the first O^* group, where the homo-coupling reaction between two O^* groups becomes easier to the nucleophilic attack by 0.7 eV in terms of reaction energy. This is also true on the nanoparticle surface where the homo-coupling reaction on the Face location lowers the reaction energy by a factor of 0.24 eV, attributed to the Ru−Ru bond flexibility. The second, as the nanoparticle size increases the OER catalytic activity converge to that on the macroscopic surface, as in the Face location. However, Edge and Tip location shows a lower catalytic activity than what was firstly expected to them, but this is attributed to the strong O^* species binding energy. Overall, it seems that nanoparticle catalytic performance increases due to the available number of active sites per gram of material but not because of an improved catalytic activity.

Chapter 6

Single Site Ir@ITO Catalyst

"Das schwarze geheimnis ist hier,
hier ist das schwarze geheimnis"

Eugen Gomringer

In this chapter we show how using surface organometallic chemistry, it is possible to prepare iridium sites atomically dispersed on indium tin oxide (ITO). These sites demonstrate high catalytic activity in one of the most challenging electrochemical process, oxygen evolution reaction OER. *In situ* X-ray absorption studies revealed the formation of $Ir^V{=}O$ intermediate under OER conditions. This work was performed in the ETH-Hönggerberg, Zürich, in Copéret's research group during a predoctoral stay. My contribution consisted mainly on the computational modeling of the system. Therefore, along this chapter special attention will be paid to the simulations, which in this case were used to determine the structure of the observed intermediates and propose a reaction mechanism consistent with the experimental data.

6.1   Introduction

Metal sites atomically-dispersed on supporting oxides have recently received more attention due to their unique catalytic properties. Atomically dispersed late transition metals, usually called (SACs), enabled numerous processes including alkene hydrogenation,[249] CO oxidation,[125,250,251] CO_2 electro-reduction[252–254] and photocatalysis.[255] In addition to site isolation, enabling unique reaction mechanisms, SACs provide an ultimate dispersion of a metal on the surface since all atoms are in principle active sites.[256] This is in contrast to metallic nanoparticles, where only atoms coming from the shell can directly be enrolled in the catalytic process: metallic nanoparticles of size $>$ 2.5nm have less than 50% of available metal atoms for catalysis. The ultimate dispersion becomes critical for the expensive and scarce noble metals catalysts such as Pt, Pd or Ir, where decreasing the noble metal content is essential for minimizing the price of the final catalyst as long as the metal sites provide the desired reactivity. In addition, because SACs have active-site elements different from bulk support, they are particularly suitable for molecular-level understanding of the active-site structure and reaction pathways by using a variety of element specific analytical tools (e.g X-ray adsorption and X-ray photoelectron spectroscopies, nuclear magnetic and electron paramagnetic resonances, Mossbauer spectroscopy, etc.) backed by *in situ* and *operando* characterization coupled with computational modeling.

Water splitting is perhaps one of the applications where SACs could lead to a significant advantage over classical metal oxide nanoparticle catalysts.[257–261] Indeed, the kinetics of the water splitting is mostly dictated by its anodic part, oxygen evolution reaction (OER), which requires harsh reaction conditions limiting the pool of possible catalysts to solely iridium and ruthenium based materials.[140] Therefore, decreasing the nobel metal content in OER catalysts becomes critical for the development of water electrolyzers involved in the sustainable hydrogen production. Furthermore, given the high complexity of the OER mechanism, four proton coupled electron transfer processes, studying SACs for OER could provide

unique information regarding the structure of the active site and reaction pathways. With rigorous isolation of the metal sites on the surface, formation of the O−O bond can only occur via the water nucleophilic attack (WNA) through a high-valent M=O intermediate and not via bimolecular coupling of two oxygen radicals on adjacent metal centers. Such reactivity would parallel what is proposed to take place in the natural oxygen evolving cluster of the photosystem II responsible for all the oxygen present in the atmosphere, in contrast to most of the experimental studies of the artificial OER systems, pointing that the oxygen radical coupling pathway is more efficient that the WNA.

6.2   Summary of Experimental Results

The atomically dispersed iridium centers on indium tin oxide (ITO) electrodes were synthesized by using the surface organometallic (SOMC) approach. In particular, the [(COD)(IMES)Ir(OH)] complex (COD= cyclooctadiene, IMES= 1,3-dimesitylimidazol-2-ylidene) was initially grafted on porous ITO. Afterwards, the sample was calcined at 400 Celsius degrees to remove all organic ligands (Figure 6.1), giving rise to the atomically dispersed iridium centers on the ITO surface (Ir_{SAC}−ITO).
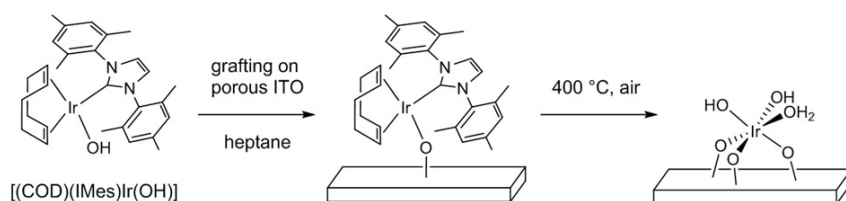
Figure 6.1: Ir_{SAC}−ITO preparation scheme with the proposed structure.

The calcined sample was characterized with elemental analysis, High-angle Annular Dark Field Scanning Transmission Electron Microscopy (HAADF-STEM) (Figure 6.2), X-Ray photoelectron spectroscopy (XPS) and Extended X-ray Absorption Fine Structure (EXAFS) (Table 6.1). The elemental analysis of the

$Ir_{SAC}-$ITO electrodes gave an Ir loading of less than one Ir per nm^2 of the ITO surface. Moreover, the HAADF-STEM microscopy showed that bright dots clearly appear after calcination on the ITO surface (Figure 6.2), which were attributed to single iridium atoms without the presence of Ir or IrO_2 cluster or nanoparticles. The XPS spectrocopy was used to determine the oxidation state of the grafted iridium center, all data being in agreement with an Ir^{III} center. The obtained data confirms the absence of large iridium or iridium oxide aggregates. Moreover, it suggests the presence of 6 oxygen neighbors at 2.04 ± 0.02 Å distance (Table 6.1), which is very close to the values found for Ir^{III} in IrO_x.[262]
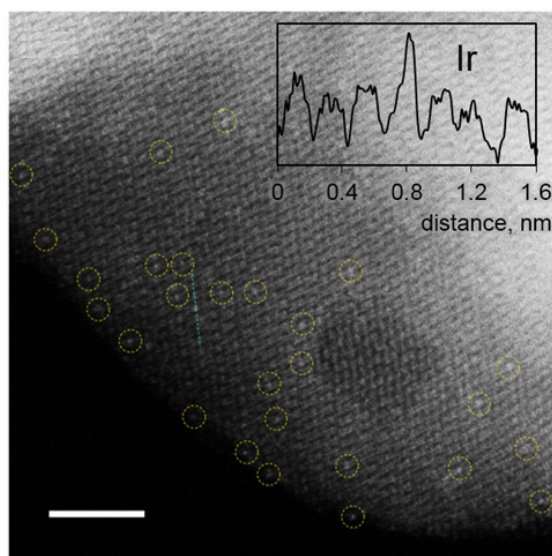
Figure 6.2: HADDF-STEM of the $Ir_{SAC}-$ITO catalyst. Bright dots highlighted with yellow circles assigned to isolated Ir atoms.

Visible-near IR transmission studies of the electrodes showed that deposition of iridium does not lead to a significant increase of the light absorption of the electrodes (on average 4% decrease of the transmission), which is in line with the low iridium amount and atomic nature of the iridium species. Moreover, this makes the proposed catalyst design suitable for use in the sunlight-driven water splitting devices with a transparent anode.

Table 6.1: Structural parameters from EXAFS data for $Ir_{SAC}-ITO$.

Fit	Sample	Shell	R	N	$\sigma \cdot 10^3$	R-Factor	Reduced Chi
	Pristine $Ir_{SAC}ITO$ (ex situ)						
1	3.2-10.68 k-space	Ir—O	2.04	6	5.6	0.003	214
	1.25-2.08 R-space						
	$Ir_{SAC}-ITO$ after 2h at 10 mA cm^2						
2	3.2-10.68 k-space	Ir—O	2.03	6	5.1	0.002	376
	1.25-2.08 R-space						
3	1.46 V vs RHE (in situ)	Ir—O	2.00	6	4.9	0.004	240
4	3.2-10.68 k-space	Ir—O	1.80	1	3.5	0.0006	40
	1.25-2.04 R-space	Ir—O	1.99	5	3.5		
5	1.46 V vs RHE (in situ)	Ir—O	2.01	6	7.0	0.005	40
6	3.2-10.68 k-space	Ir—O	1.83	1	2.3	0.0013	11
	1.25-2.04 R-space	Ir—O	2.03	5	2.3		
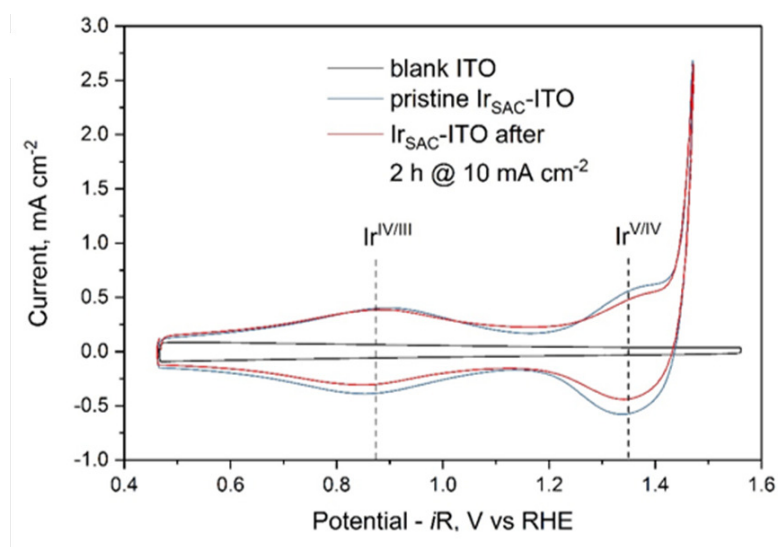
Figure 6.3: Cyclic voltammetry of blank ITO, pristine $Ir_{SAC}-ITO$ and $Ir_{SAC}-ITO$ after 2h at 10 mA cm^{-2} (0.1M HClO$_4$, 10mV s^{-1}).

The OER catalytic activity of $Ir_{SAC}-ITO$ was examined using chronoamperometric measurements in 0.1M $HClO_4$, observing similar or slightly higher catalytic activities than the state of the art iridium based catalyst. Indeed, the Tafel plot of $Ir_{SAC}-ITO$ presents a slope of 46 ± 4 mV dec^{-1}, which is similar to what is observed on iridium oxide nanoparticles.[263–265] The current of 10 A gIr^{-1} can be achieved at 1.449 ± 0.005 V vs RHE, which is lower than 1.470 V reported for Ir nanoparticles dispersed on ITO and high surface are IrO_2 and IrO_2-TiO_2 catalysts (1.485 - 1.497 V). Moreover, $Ir_{SAC}-ITO$ produces the current of 156 ± 13 A $g(Ir)^{-1}$ at 1.51 V vs RHE, which is higher than that reported for state of the art Ir and IrO_2 nanoparticles. High activity of the $Ir_{SAC}-ITO$ is likely due to the ultimate Ir dispersion on the electrode surface. In order to analyze the reaction products and confirm the formation of oxygen, the amount of O_2 released was quantified using a Clark electrode sensor, obtaining a 99 % of O_2.

With the aim of characterizing the intermediate species during the catalytic process. Cyclic voltammetry (Figure 6.3) and experiments were carried out (XAS and EXAFS). The cyclic voltammetry shows the presence of two redox waves located at 0.89 and 1.35 V vs RHE that were attributed to the one electron Ir(III/IV) and (IV/V) transitions.[264] These assignments were also confirmed by X-Ray absorption spectroscopy, which was also used to characterize the coordination of the Ir^{VI} species. Indeed, *in situ* EXAFS data at a potential of 1.46 V vs RHE shows the best fitting when considering one short $Ir-O$ distance of 1.83 Å and five larger ones at distances around 2.03 Å.

6.3 Computational Results

DFT calculations were used to further characterize the reaction intermediates as well as to propose a reaction mechanism in agreement with experimental data. For that, i) different isomers have been explored across the possible Ir oxidation states as a tris-grafted single site, ii) the energy cost of the electrochemical processes between the different Ir oxidation states have been computed as a function of pH (Pourbaix diagram) and iii) two possible reaction pathways has been proposed through the water nucleophilic attack (WNA) mechanism.

6.3.1 Methodology and Models

Calculations were carried out using periodic boundary conditions as implemented in the *Vienna Ab-initio Simulation Package* (VASP)[214,215] code. All calculations were performed considering the projector augmented wave (PAW)[216] pseudopotentials. Valence electrons were expanded in plane waves with kinetic energy cutoff equal to 500 eV. The chosen functional was the PBE exchange correlation GGA functional.[217] This functional have been largely used for the study of oxygen evolution reaction by a variety of heterogeneous catalysts, but it does not properly describe dispersion forces. This has been corrected by adding the Grimme's (D2)[194] empirical correction. This correction has been recently reported to better reproduce lattice parameters for a larger variety of systems when compared with the D3 one. The energy threshold for the self-consistency of the electron density was set to 10^{-5} eV and the optimization of the structure was conducted through a conjugate gradient technique, which stops when Hellmann-Feynman forces on all atoms are less than 0.01 eV Å^{-1}. Bulk calculations were performed considering a K-point mesh for the Brillouin Zone (BZ) of (6,6,6) employing the Monkhorst-pack grid (MP),[218] while slab calculations were performed considering a Monkhorst-Pack K-point mesh of (6,6,1). The cutoff and K-point mesh were calibrated by ensuring the convergence of both cell parameters and cell energies.

All calculation involving the monodisperse single-site Ir species onto the surface were performed as spin-polarized. Iridium electron configuration is $6s^2\ 5d^7$, thus Ir^{III}, Ir^{IV}, Ir^V and Ir^{VI} pseudo-octahedral complexes present 6, 5, 4, 3 electrons respectively on the t_{2g} d orbitals. Therefore, the ground states of Ir^{III}, Ir^{IV}, Ir^V and Ir^{VI} are singlet, doublet, triplet and doublet respectively, and this can only be described with a spin-polarized formalism.

The isolated Ir center on ITO has been represented with a (14.5 x 14.5 Å) slab periodic model of the (111) surface (Figure 6.4) containing the Ir center coordinated to indium oxide support through three $Ir-O(H)-In$ bonds. In this model the Ir loading is 0.55 Ir per nm^2 which is very close to the experimental one. Tin atoms were omitted in the calculation for simplification as we do no expect that the presence of very few Sn atoms in the model would influence the electronic structure of Ir. The slab models were constructed from the fully optimized unit cell, considering a 4-layer thickness, the minimum slab thickness for achieving the convergence in terms of surface energy. Computed values, along with previously reported ones are given in Table 6.2 along with the work function. As can be seen, the obtained values for the surface energy as well as the work function are in a good agreement with the previous values from the literature.[266,267]
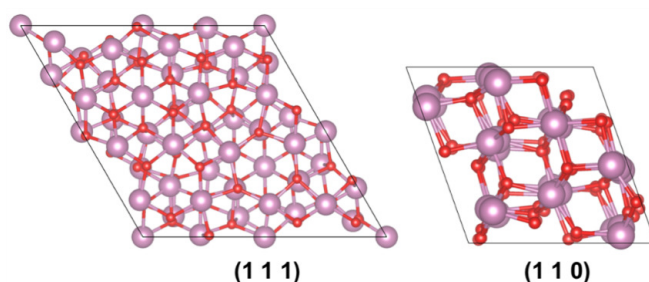
Figure 6.4: Top view of In_2O_3 slab models.

Table 6.2: In_2O_3 main crystallographic orientations surface energies (in $eV/Å^2$) and work function (in eV).

Surface	$\gamma_{hkl}^{a,b}$	γ_{hkl}^{c}	Work F.
(111)	0.04(9)	0.0499	5.041
(110)	0.06(9)	0.0690	4.260

(a, b) Surface energy values from Ref.[266,267]

(c) Computed surface energy values in this work.

The *c* value was set to 35 Å ensuring an interlayer distance of at least 21 Å to minimize the interaction between replicas at the (hkl) perpendicular direction. Due to the asymmetry generated upon anchoring the Ir single site, a dipolar correction in the z axis has been added.

Addition of the Ir center on the (111) surface was made in two steps. First, we constructed a solvated model of the (111) indium oxide surface without the presence of iridium and added a high local water coverage. During the optimization about half of the adsorbed water molecules dissociates. In a second step, Ir center in the form of $Ir(OH)_3(H_2O)_3$ cluster was added on a locally solvated surface, which was followed by three proton transfers from surface $In-OH$ to the OH ligands of iridium. Attachment of the Ir complex to the surface involves the displacement of three water molecules to establish the new $In-O-Ir$ bonds, leading to a tris-bound species (Figure 6.5). Note that additional proton transfer occurs during the optimization between the Ir ligands and the surface as well as between adsorbed water molecules and the $In-O-Ir$ bonds. As a consequence, several species for each oxidation state are plausible. In this context the Ir oxidation state is defined by the total number of hydrogens in the model and assuming that the oxygen and indium oxidation states are always -2 and -3, respectively. In total, the initial Ir^{III} complex supported on indium oxide model presents 48 indium, 83 oxygen, one iridium and 19 hydrogen atoms. The Ir^{IV}, Ir^{V} and Ir^{VI} species are thus modeled subtracting one hydrogen atom in a stepwise manner.
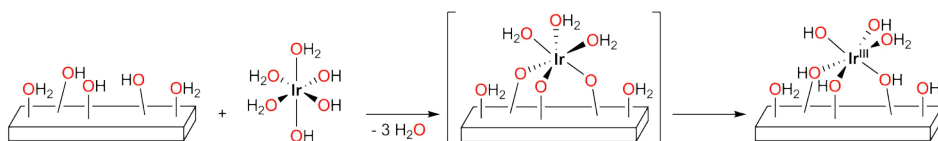
Figure 6.5: $Ir(OH)_3(H_2O)_3$ complex grafting process onto In_2O_3 support.

The electronic energies for the iridium single site system along the OER were corrected with single point calculations applying an ONIOM[268] like scheme with two layers: i) the low level corresponds to the PBE-D2 periodic model computed with VASP and ii) the inner layer corresponds to the $(H_2O)(OH)Ir(OH)_2(H_2O)$ cluster (for initial Ir^{III} species) computed with the highly accurate double-hybrid[269] functional B2GP-PLYP as implemented in ORCA.[270] The B2GP-PLYP method includes 36 and 65 percentage of MP2 and HF, respectively. In the molecular calculation, atoms were represented with the split-valance triple-z basis set with polarization def2-TZVP.[271] The equation for the electronic energy correction is:

$$E_{intermediate} = E_{PBE-D2}^{PBC} + (E_{PBE-D2}^{SAC} - E_{B2GP-PLYP}^{SAC}) \qquad (6.1)$$

where the term E_{PBE-D2}^{PBC} consists in the electronic energy of the full system using VASP, E_{PBE-D2}^{SAC} is the electronic energy of the above-mentioned cluster with the same theoretical level as the periodic VASP calculation, and finally $E_{B2G-PLYP}^{SAC}$ is the electronic energy of the molecular cluster computed using a double-hybrid functional with ORCA DFT code.[270]

6.3.2 Nature of Ir Intermediates

Several Ir_{SAC}−ITO species were explored for each Ir oxidation state (from Ir^{III} to Ir^{VI}). We first considered the Ir_{SAC}−ITO as a tris-grafted Ir^{III} complex bonded to three OH species coming from the built solvated slab model of In_2O_3. Complexes with higher oxidation state, from Ir^{IV} to Ir^{VI} were modeled by subsequently subtracting a $H^+ + e^-$. Relative energies of all computed isomers enclosing a different number of OH/H_2O in the first coordination sphere of Ir are shown in Figure 6.6. Main structural parameters are given in Table 6.3 and optimized structure in appendix (Figure D.1).

Three different Ir^{III} isomers were considered. The most stable structure has a general formula of $(\equiv InOH)_3Ir(OH)_2(H_2O)$ with three hydroxyl ligands bonded to In atoms of the oxide surface (In-OH-Ir). The optimized Ir−O distances vary from 1.98 to 2.15 Å with an average value of 2.06 Å (Table 6.3, Appendix A.1), which is close to the value obtained via EXAFS data (2.04 Å) of pristine Ir_{SAC}−ITO (Table 6.1). The other two isomers present two aquo ligands as a consequence of a proton transfer process either from the surface or from one of the In−OH−Ir. The computed energies suggest that they are significantly less stable (40.5 to 51.1 $kJ \cdot mol^{-1}$)

Similarly, three different isomers for Ir^{IV} were considered. The most stable structure has a general formula of $(\equiv InOH)_3Ir(OH)_3$. In this case, Ir−O distances vary from 1.94 to 2.10 Å with an average value of 2.02 Å (Table 6.3). Subsequent PCET process from Ir^{IV} reaches the Ir^{V} species. The most stable Ir^{V} presents a general formula of $(\equiv InOH)_3Ir(O)(OH)_2$ anchored to the oxide support. The Ir−O distances vary from 1.80 to 2.10 Å, where the shortest one corresponds to the Ir=O group which matches well the experimental EXAFS data being 1.83 Å (Table 6.1). The average of the other 5 Ir−O distances is 2.05 Å (Table 6.3).
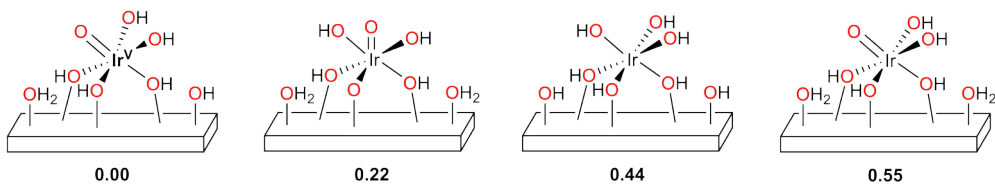
[Ir^{III}] - (1)
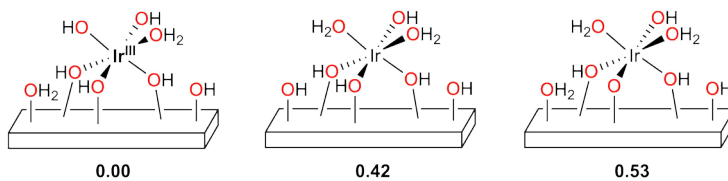
[Ir^{IV}] - (2)
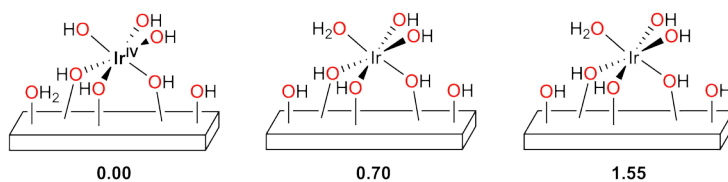
[Ir^{V}] - (3)
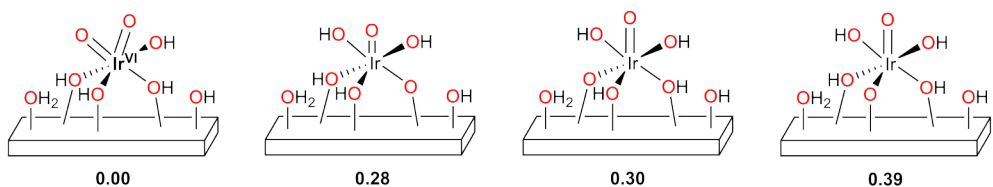

[Ir^{VI}] - (4)

Figure 6.6: Ir^{SAC}−ITO single site catalyst isomers with relative energies in eV. Numbers in parenthesis corresponds to the species label on the OER mechanism.

Table 6.3: Ir−O bond distances for the most stable simulated Ir species.

Ir-Species	Potential[a]	Ir Ox. State[b]	Ir−OH$_2$	Ir−OH	Ir=O	Ir−OH−In	Average
(≡InOH)$_3$Ir(OH)$_2$(H$_2$O)	0.00-0.60	+3	2.15	2.05 2.05	-	2.08 1.98 2.08	2.06
(≡InOH)$_3$Ir(OH)$_3$	0.60-1.34	+4	-	1.94 2.04 1.92	-	2.10 2.00 2.09	2.02
(≡InOH)$_3$Ir(O)(OH)$_2$	1.34-1.55	+5	-	2.04 1.99	1.80	2.06 2.10 2.04	2.05
(≡InOH)$_3$Ir(O)$_2$(OH)	>1.55	+6	-	2.02	1.78 1.79	2.19 2.09 2.03	2.08

(a) all potential are in V vs. RHE and distances in Å

(b) Ir Oxidation state is calculated as formal counting manner

In summary, the Ir[III] to Ir[IV] and Ir[V] oxidation occurs by changing the nature of the initial ligand from neutral aquo to negatively charged hydroxyl group first and then to an Ir=O, while the other ligands of the iridium coordination sphere remain unchanged. At this point it is worth mentioning that the Ir[V] complex is the highest oxidation state observed through experiments and thus, it will be considered the starting point for the water nucleophilic attack (WNA) mechanism, in the following section. Despite this, we decided to explore the possible existence of a potential Ir[VI] intermediate, with the aim to determine its stability with respect to the other species.

The most stable structure of Ir[VI] consist in a bis-oxo with a general formula of (≡InOH)$_3$Ir(O)$_2$(OH) (Figure 6.6). The Ir−O distances vary from 1.78 to 2.19 Å, the shortest ones corresponding to two Ir=O groups (1.78 and 1.79 Å), as expected. The other Ir−O range from 2.02 to 2.19 Å with an average value of 2.08 Å (Table 6.3). These bond distances are significantly different to those determined by EXAFS suggesting that Ir[VI] is not observed experimentally.

Once determined the most stable intermediates we have constructed the Pourbaix diagram (Figure 6.7), assuming that the electrochemical reactions are described by the most stable supported Ir intermediates without the active participation of the support. For the supported Ir system we chose the species with the highest content of H atoms as reference (G_{ref}). From these species we proceeded by removing hydrogen atoms to obtain the Gibbs energies of different species (G_i). The change of Gibbs energy results in:

$$\Delta G_i(U, pH) = G_i - G_{ref} - n_H(\frac{1}{2}G_{H_2} + U + k \cdot pH) \qquad (6.2)$$

Here n_H is the number of (H$^+$ + e$^-$) transferred to the media as a full electrochemical proton coupled electron transfer (PCET) process. The effect of the bias on all steps involving an electron is included by shifting the energy of these states by $(-eU)$, where U is the electrode potential. The dependence on the pH is accounted for the $(k \cdot pH)$ term, which comes from:

$$\Delta G(pH) = -k_B T \cdot ln[\text{H}^+] = k \cdot pH \qquad (6.3)$$

Therefore, we can derive a relationship between the potential and the pH for a wide variety of adsorbates on a supported catalyst assuming as reference the standard condition when ($\Delta G(U, pH) = 0$). As shown in Figure 6.7, the Ir^{III} complex undergoes a PCET to Ir^{IV} at 0.60 V vs RHE (pH=0). This electrochemical step is underestimated in comparison to the experimental potential which is around 0.80 V. Ir^{IV} complex is oxidized to Ir^V at 1.34 V vs RHE, which is in good agreement with experiments (1.35 V vs RHE). Further step consist in the Ir^V oxidation to Ir^{VI} which presents an electrochemical potential of 1.55 V vs RHE, a value in which oxygen bubbles are already observed in experiments and thus Ir^{VI} can not be detected.
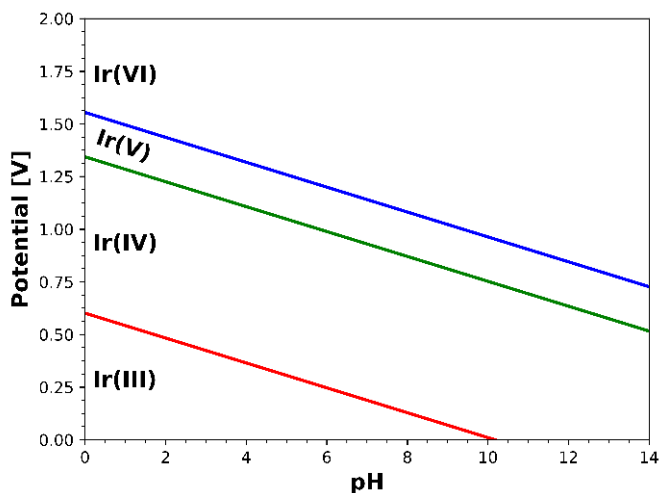
Figure 6.7: Ir$_{SAC}$−ITO Computed Pourbaix diagram.

6.3.3 Oxygen Evolution Reaction Mechanisms

With the aim of proposing a mechanism consistent with the experimental data, two possible pathways for O−O bond formation were explored (Figure 6.8): i) direct water nucleophilic attack (WNA) on Ir^{V} complex **(3)** and ii) WNA on high-valent Ir^{VI} dioxo intermediate (**4**). Noteworthy, three different possibilities for the direct WNA to Ir^{V} were considered.

Both pathways start with the most stable Ir^{III} isomer **(1)**, which is oxidized to Ir^{IV} **(2)** through a proton coupled electron transfer (PCET) process with a ΔG of 0.60 eV. The second step is the oxidation of Ir^{IV} **(2)** intermediate to Ir^{V} **(3)** through a consecutive PCET process, which presents a ΔG of 1.34 eV that well correlates with the electrochemical potential observed experimentally, as shown in the Pourbaix diagram. The Ir^{V} **(3)** intermediate can be nucleophilically attacked on the oxo group Ir^{V}=O or be further oxidized to Ir^{VI} **(4)**, before the WNA takes place.
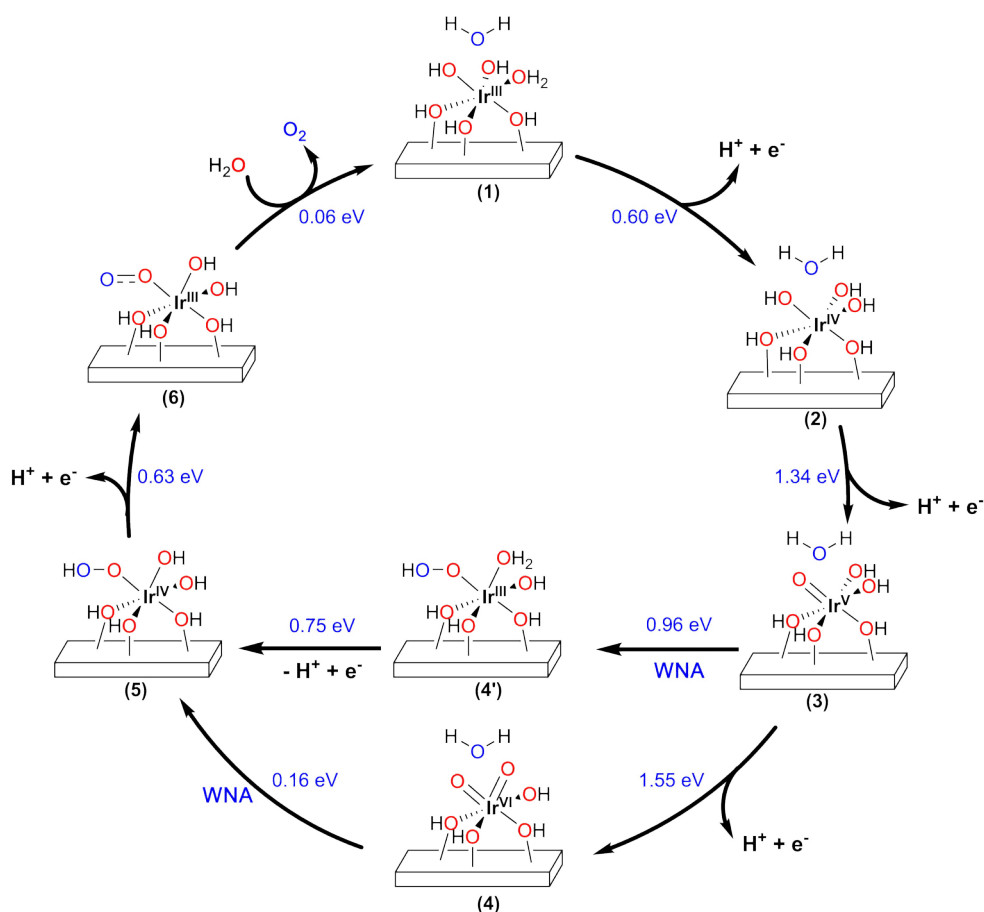
Figure 6.8: Possible pathways for the O−O bond formation on Ir single site catalyst.

From the Ir^V **(3)** intermediate, three possible WNA were envisaged. In the three processes, water is splitted in OH$^-$ and H$^+$ fragments, the former being transferred to the oxo group leading to a OOH ligand. The three explored processes differ on the site receiving the H$^+$. In the first possibility the H$^+$ is transferred to an OH ligand of Iridium. In the second one, the H$^+$ is transferred to the surface. Finally, we also explored the potential formation of an (In−OH$_2$Ir(OH)$_2$(OOH) pentacoordinated complex by transferring the H to an OH group bound both to Indium and Iridium. The pentacoordinated complex appears not to be a minimum

on the potential energy surface as all out trials evolved spontaneously to reactants during the optimization. The WNA attack leading to $(In-OH)_3Ir(OH)(H_2O)(OOH)$ (the proton is transferred to an OH ligand) is highly endergonic with a reaction energy of 0.96 eV (92.6 $kJ \cdot mol^{-1}$). Finally, the WNA process in which the proton is transferred to the surface is even less favorable. Consequently, even though the PCET process leading to $(In-OH)_3Ir(OH)_2(OOH)$, (**(4)′ → (5)**) is electrochemically very easy $\Delta G = 0.75$ eV, the chemical step associated to the direct WNA to Ir^V (**(3) → (4)**) seems unlikely according to calculations.

The Ir^V to Ir^{VI} oxidation is challenging, as already shown in the Pourbaix diagram. It requires overcoming potentials up to 1.55 V. However, once the Ir^{VI} is formed the WNA is feasible with a reaction Gibbs energy of 0.16 eV (15.4 $kJ \cdot mol^{-1}$). Overall, the differences in the chemical step between the two explored mechanisms suggests that oxidation to Ir^{VI} is more likely than the direct attack on the $Ir^V{=}O$.

The O_2 molecule release from the Ir single site catalyst, occurs in two steps: i) a pure electrochemical step from intermediate $Ir-OOH$ **(5)** to generate $Ir-OO$ **(6)** and ii) the chemical O_2 by H_2O substitution. Different isomers for $Ir-OOH$ and $Ir-OO$ have been explored (Figure 6.9) and the most stable one derives from the most stable **(5)** intermediate by losing the hydrogen of the OOH ligand. This electrochemical step is easy ($\Delta G = 0.63$ eV) and the chemical substitution is also favorable thus suggesting that once the $Ir-OOH$ is formed the reaction is downhill at the applied potential.

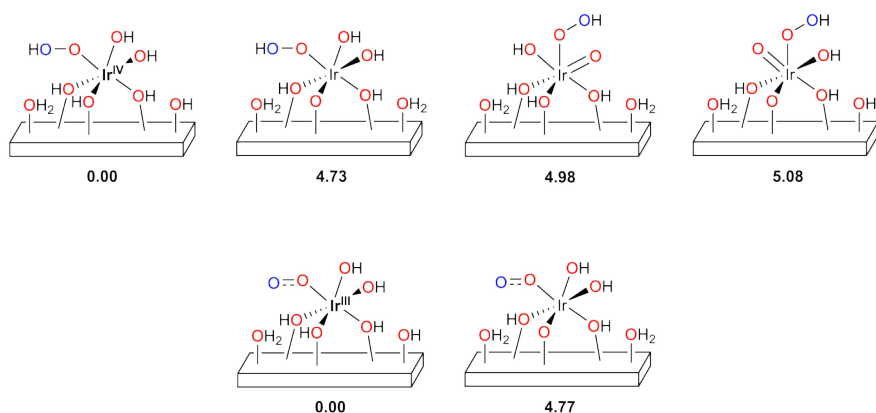**Figure 6.9:** Ir−OOH **(5)** and Ir−OO **(6)** single site catalyst isomers (in eV).

In summary, the Ir^{VI} pathway does not imply any challenging chemical steps and predicts an overpotential of 0.32 V, in agreement with the low overpotential observed experimentally. The fact that the Ir^{VI} intermediate is not observed in the experiment neither by electrochemistry nor by spectroscopy indicates that Ir^{V} is the resting state of the catalyst and that the Ir^{VI} species are short-lived. In this context, DFT calculations indicate that the water nucleophilic attack is too challenging on the Ir^{V} species and another PCET step is required to make the experimentally observed surface Ir^{V}=O more electrophilic. Interestingly, recent computational studies on molecular Ir complexes[73,272] found that formation of the high-valent Ir^{VI} intermediate is plausible and could facilitate the OER catalysis. The proposed Ir^{VI} intermediate is isoelectronic to Ru^{V} species, which are believed to play an important role in molecular OER catalyst.

6.4   Conclusions

A well-defined atomically dispersed Ir electrocatalyst highly active and stable in acidic conditions has been synthesized and characterized by the group of Prof.Dr. Copéret. The high OER activity of the catalyst ranks among that of the highest performing Ir:IrO$_x$ catalysts, which is achieved due to the ultimate Ir dispersion. Computational modeling of Ir^{III},Ir^{IV}, Ir^{V} and Ir^{VI} species and two reaction pathways with isolated Ir sites suggest that the initial oxidation process takes place on one single ligand of Ir$_{SAC}-$ITO catalyst that evolves from H$_2$O to OH and O. Moreover, results that Ir^{V}=O species is the catalyst resting state of the reaction, which should be further oxidized to Ir^{VI}, in the rate determining electrochemical step, before the WNA occurs. This Ir^{VI} is short-lived under electrocatalytic conditions, explaining why it is not detected in the experimental study.

Chapter 7

General Conclusions

This thesis is a contribution to the effort done to understand the catalytic performance differences between heterogeneous RuO_2 surfaces and nano-sized catalysts, as a part of a more general emerging oxygen evolution reaction (OER) electrocatalysis based on the outstanding catalytic performance on nano-sized catalysts. For that, atomistic simulations using state-of-the-art computational techniques were carried out to understand water interaction on RuO_2 main surfaces as well as on built atomistic nanoparticle models of different sizes, considering either different water coverages and different topological undercoordinated Ru sites involved in the water adsorption process. The catalytic performance of RuO_2 on the oxygen evolution reaction (OER) were explored through the water nucleophilic attack (WNA) and oxo-coupling (I2M) mechanisms for both surfaces and nanoparticle models. Furthermore, the catalytic behavior of an Ir single site catalyst supported on indium oxide for OER was studied during a predoctoral stay in the ETH Zürich (Switzerland).

Based on the results obtained the following general conclusions may be drawn. Water adsorption onto the RuO_2 surfaces have shown that the proton transfer process that leads to the dissociated adsorbed form is controlled by three main factors: i) the intrinsic acidity of the undercoordinated Ru atoms, ii) the basicity of the O_{br} groups coming from the surface, and iii) cooperative effects between adsorbed water molecules on contiguous Ru atoms. Indeed, water dissociation only occurs on the (110) surface at low water coverages. However, for larger coverages, intermolecular cooperative effects favor the formation of the $H_3O_2^-$ water dimer motif consisting in a strong internal hydrogen bond between one water and one dissociated water molecules. As a result, ab initio molecular dynamics simulations for the full monolayer lead to a 50 % of dissociation for the (110) and (011) surfaces and to a 25 % of dissociation for the (100) and (001) ones.

Wulff like stoichiometric RuO_2 nanoparticle models of different sizes have been built for the first time and water interactions analyzed. Results showed that dissociated water is not only the preferred form at the Face site but also at the Edges, Tips and Corner sites due to an increase of the O_{br} basicity in the nanoparticle. Nevertheless, due to the high stability of the $H_3O_2^-$ motif because of hydrogen bond cooperativity, AIMD simulations for a full monolayer coverage leads to around 50 % of dissociation.

Concerning the reaction mechanism of OER, results indicate that for all surfaces the WNA is the applying mechanism, the formation of OOH^* being the potential determinant step. The oxo-coupling mechanism I2M is less favorable since the chemical step associated to O_2 formation is energetically too demanding (100 $kJ \cdot mol^{-1}$). Major differences between surface are related to the nature of the surface vacant sites (axial Ru_{5C} on the (110) and (100) surfaces, equatorial Ru_{5C} on (011) and equatorial Ru_{4C} on the (001)), the oxo formation being more favorable on the two latter surfaces, which hinders the subsequent WNA and leads to a higher overpotential. Present results are in agreement with the Shao-Horn and co-workers[242] study, which indicates that the catalytic activity of different

surfaces is (100) > (011) > (110) but it disagrees with a recent study that states that the (001) is the most active one. Discrepancies, however, may be attributed to the presence of defects since prepared surfaces exhibit a roughness of 1 nm. Results for the OER reaction at the Face sites of RuO_2 nanoparticles are very similar to those obtained with the slab model. Corner, Tip and Edge sites show a lower catalytic activity mainly due to a larger O^* adsorption energy at these sites. Noticeably, the I2M mechanism on nanoparticle models seems to be significantly more favorable (60 $kJ \cdot mol^{-1}$) than when considering the slab model due to a higher flexibility of the nanoparticle, which allows shorter Ru−Ru distances. Thus, this mechanism may start being competitive with small nanoparticles.

Finally, simulations of Ir single site catalyst grated on an indium tin oxide (ITO) support were performed and two possible pathways for the O−O bond formation explored: i) a direct WNA on an Ir^V oxo pentavalent complex and ii) WNA on a high-valent Ir^{VI} dioxo intermediate. Such reactivity study concludes that the $Ir^V{=}O$ species is the catalyst resting state and that the preferred process involves a PCET step to form an Ir^{VI} bis-oxo species from which WNA step occurs more favorably than from Ir^V intermediate.

Overall, despite difficulties in the computational description of solvent effects and the electronic structure of these systems, present computational results have provided new insights that can be useful for further design of new and more optimized heterogeneous, nanosized and single site catalysts. In particular, since the most stable surface is not the most reactive one, synthetic methods favoring the presence of the (100) surface should be explored to obtain more active RuO_2 catalysts.

Bibliography

(1) Chow, J.; Kopp, R. J.; Portney, P. R. *Science* **2003**.

(2) Lewis, N. S.; Nocera, D. G. *Proceedings of the National Academy of Sciences* **2006**.

(3) Armaroli, N.; Balzani, V. The future of energy supply: Challenges and opportunities, **2007**.

(4) Economics, B. E. *2018 BP Energy Outlook* **2018**.

(5) Karl, T. R.; Trenberth, K. E. Modern Global Climate Change, **2003**.

(6) By the President, P. In, **2015**.

(7) Tollefson, J. How green is my future?, **2011**.

(8) Morton, O. Solar energy: A new day dawning?: Silicon Valley sunrise, **2006**.

(9) Cook, T. R.; Dogutan, D. K.; Reece, S. Y.; Surendranath, Y.; Teets, T. S.; Nocera, D. G. *Chemical reviews* **2010**, *110*, 6474–6502.

(10) Dasgupta, S.; Brunschwig, B. S.; Winkler, J. R.; Gray, H. B. *Chemical Society Reviews* **2013**, *42*, 2213–2214.

(11) Sanderson, K. Chemistry: The photon trap, **2008**.

(12) Hurst, J. K. In pursuit of water oxidation catalysts for solar fuel production, **2010**.

(13) Barber, J. *Biochemical Society Transactions* **2006**, *34*, 619–631.

(14) Barber, J. *Chemical Society Reviews* **2009**, *38*, 185–196.

(15) Siegbahn, P. E. *Accounts of Chemical Research* **2009**, *42*, 1871–1880.

(16) Nelson, N.; Ben-Shem, A. The complex architecture of oxygenic photosynthesis, **2004**.

(17) McEvoy, J. P.; Brudvig, G. W. Water-splitting chemistry of photosystem II, **2006**.

(18) Ferreira, K. N.; Iverson, T. M.; Maghlaoui, K.; Barber, J.; Iwata, S. *Science* **2004**, *303*, 1831–1838.

(19) Kok, B.; Forbush, B.; McGloin, M. *Photochemistry and Photobiology* **1970**, *11*, 457–475.

(20) Umena, Y.; Kawakami, K.; Shen, J.-R.; Kamiya, N. *Nature* **2011**, *473*, 55.

(21)   Glatzel, P.; Schroeder, H.; Pushkar, Y.; Boron III, T.; Mukherjee, S.; Christou, G.; Pecoraro, V. L.; Messinger, J.; Yachandra, V. K.; Bergmann, U., et al. *Inorganic chemistry* **2013**, *52*, 5642–5644.

(22)   Kulik, L. V.; Epel, B.; Lubitz, W.; Messinger, J. *Journal of the American Chemical Society* **2007**, *129*, 13421–13435.

(23)   Loll, B.; Kern, J.; Saenger, W.; Zouni, A.; Biesiadka, J. *Nature* **2005**, *438*, 1040.

(24)   Yano, J.; Kern, J.; Irrgang, K.-D.; Latimer, M. J.; Bergmann, U.; Glatzel, P.; Pushkar, Y.; Biesiadka, J.; Loll, B.; Sauer, K., et al. *Proceedings of the National Academy of Sciences* **2005**, *102*, 12047–12052.

(25)   Yano, J.; Kern, J.; Sauer, K.; Latimer, M. J.; Pushkar, Y.; Biesiadka, J.; Loll, B.; Saenger, W.; Messinger, J.; Zouni, A., et al. *Science* **2006**, *314*, 821–825.

(26)   Karlsson, S.; Boixel, J.; Pellegrin, Y.; Blart, E.; Becker, H. C.; Odobel, F.; Hammarström, L. *Journal of the American Chemical Society* **2010**.

(27)   Meyer, T. J. *Accounts of Chemical Research* **1989**, *22*, 163–170.

(28)   Bard, A. J.; Fox, M. A. *Accounts of Chemical Research* **1995**, *28*, 141–145.

(29)   Gust, D.; Moore, T. A.; Moore, A. L. *Accounts of chemical research* **2009**, *42*, 1890–1898.

(30)   Styring, S. *Faraday Discuss.* **2011**.

(31)   McKone, J. R.; Lewis, N. S.; Gray, H. B. *Chemistry of Materials* **2013**, *26*, 407–414.

(32)   Amouyal, E. *Solar Energy Materials and Solar Cells* **1995**, *38*, 249–276.

(33)   Tachibana, Y.; Vayssieres, L.; Durrant, J. R. *Nature Photonics* **2012**, *6*, 511.

(34)   Walter, M. G.; Warren, E. L.; McKone, J. R.; Boettcher, S. W.; Mi, Q.; Santori, E. A.; Lewis, N. S. *Chemical reviews* **2010**, *110*, 6446–6473.

(35)   Osterloh, F. E. *Chemical Society Reviews* **2013**, *42*, 2294–2320.

(36)   Green, M. A. *Progress in Photovoltaics: Research and Applications* **2009**, *17*, 183–189.

(37)   Turner, J. A. *Science* **2004**, *305*, 972–974.

(38)   Chen, X.; Shen, S.; Guo, L.; Mao, S. S. *Chemical reviews* **2010**, *110*, 6503–6570.

(39)   Kudo, A.; Miseki, Y. *Chemical Society Reviews* **2009**, *38*, 253–278.

(40)   Kitano, M.; Hara, M. *Journal of Materials Chemistry* **2010**, *20*, 627–641.

(41)   Fujishima, A.; Honda, K. *nature* **1972**, *238*, 37.

(42)   Inoue, H.; Shimada, T.; Kou, Y.; Nabetani, Y.; Masui, D.; Takagi, S.; Tachibana, H. *ChemSusChem* **2011**, *4*, 173–179.

(43) Privalov, T.; Åkermark, B.; Sun, L. *Chemistry–A European Journal* **2011**, *17*, 8313–8317.

(44) Bagotsky, V. S., *Fundamentals of electrochemistry*; John Wiley & Sons: **2005**; Vol. 44.

(45) Bard, A. J.; Faulkner, L. R.; Leddy, J.; Zoski, C. G., *Electrochemical methods: fundamentals and applications*; wiley New York: **1980**; Vol. 2.

(46) Allakhverdiev, S. I.; Casal, J. J.; Nagata, T. *Photochemical & Photobiological Sciences* **2009**, *8*, 137–138.

(47) Sun, L.; Hammarström, L.; Åkermark, B.; Styring, S. *Chemical Society Reviews* **2001**, *30*, 36–49.

(48) Yang, J.; Wang, D.; Han, H.; Li, C. *Accounts of chemical research* **2013**, *46*, 1900–1909.

(49) Romero, I.; Rodrıéguez, M.; Sens, C.; Mola, J.; Rao Kollipara, M.; Francas, L.; Mas-Marza, E.; Escriche, L.; Llobet, A. *Inorganic chemistry* **2008**, *47*, 1824–1834.

(50) Sala, X.; Maji, S.; Bofill, R.; Garcia-Anton, J.; Escriche, L.; Llobet, A. *Accounts of chemical research* **2013**, *47*, 504–516.

(51) Weinberg, D. R.; Gagliardi, C. J.; Hull, J. F.; Murphy, C. F.; Kent, C. A.; Westlake, B. C.; Paul, A.; Ess, D. H.; McCafferty, D. G.; Meyer, T. J. *Chemical Reviews* **2012**, *112*, 4016–4093.

(52) Gersten, S. W.; Samuels, G. J.; Meyer, T. J. *Journal of the American Chemical Society* **1982**, *104*, 4029–4030.

(53) Gilbert, J. A.; Eggleston, D. S.; Murphy Jr, W. R.; Geselowitz, D. A.; Gersten, S. W.; Hodgson, D. J.; Meyer, T. J. *Journal of the American Chemical Society* **1985**, *107*, 3855–3864.

(54) Sens, C.; Romero, I.; Rodrıéguez, M.; Llobet, A.; Parella, T.; Benet-Buchholz, J. *Journal of the American Chemical Society* **2004**, *126*, 7798–7799.

(55) Roeser, S.; Ertem, M. Z.; Cady, C.; Lomoth, R.; Benet-Buchholz, J.; Hammarström, L.; Sarkar, B.; Kaim, W.; Cramer, C. J.; Llobet, A. *Inorganic chemistry* **2011**, *51*, 320–327.

(56) Romain, S.; Bozoglian, F.; Sala, X.; Llobet, A. *Journal of the American Chemical Society* **2009**, *131*, 2768–2769.

(57) Zong, R.; Thummel, R. P. *Journal of the American Chemical Society* **2005**, *127*, 12802–12803.

(58) Zhang, G.; Zong, R.; Tseng, H.-W.; Thummel, R. P. *Inorganic chemistry* **2008**, *47*, 990–998.

(59) Concepcion, J. J.; Jurss, J. W.; Templeton, J. L.; Meyer, T. J. *Journal of the American Chemical Society* **2008**, *130*, 16462–16463.

(60) Richmond, C. J.; Matheu, R.; Poater, A.; Falivene, L.; Benet-Buchholz, J.; Sala, X.; Cavallo, L.; Llobet, A. *Chemistry–A European Journal* **2014**, *20*, 17282–17286.

(61) Matheu, R.; Ghaderian, A.; Francas, L.; Chernev, P.; Ertem, M.; Benet-Buchholz, J.; Batista, V.; Haumann, M.; Gimbert-Suriñach, C.; Sala, X., et al. *Chemistry–A European Journal* **2018**.

(62) Matheu, R.; Ertem, M. Z.; Pipelier, M.; Lebreton, J.; Dubreuil, D.; Benet-Buchholz, J.; Sala, X.; Tessier, A.; Llobet, A. *ACS Catalysis* **2018**, *8*, 2039–2048.

(63) Wasylenko, D. J.; Ganesamoorthy, C.; Borau-Garcia, J.; Berlinguette, C. P. *Chemical Communications* **2011**, *47*, 4249–4251.

(64) Dogutan, D. K.; McGuire Jr, R.; Nocera, D. G. *Journal of the American Chemical Society* **2011**, *133*, 9178–9180.

(65) Ertem, M. Z.; Cramer, C. J. *Dalton Transactions* **2012**, *41*, 12213–12219.

(66) Fu, S.; Liu, Y.; Ding, Y.; Du, X.; Song, F.; Xiang, R.; Ma, B. *Chemical Communications* **2014**, *50*, 2167–2169.

(68) Zhang, T.; Wang, C.; Liu, S.; Wang, J.-L.; Lin, W. *Journal of the American Chemical Society* **2013**, *136*, 273–281.

(69) Fillol, J. L.; Codolà, Z.; Garcia-Bosch, I.; Gómez, L.; Pla, J. J.; Costas, M. *Nature chemistry* **2011**, *3*, 807.

(70) Coggins, M. K.; Zhang, M.-T.; Vannucci, A. K.; Dares, C. J.; Meyer, T. J. *Journal of the American Chemical Society* **2014**, *136*, 5531–5534.

(71) McDaniel, N. D.; Coughlin, F. J.; Tinker, L. L.; Bernhard, S. *Journal of the American Chemical Society* **2008**, *130*, 210–217.

(72) Dzik, W. I.; Calvo, S. E.; Reek, J. N.; Lutz, M.; Ciriano, M. A.; Tejel, C.; Hetterscheid, D. G.; de Bruin, B. *Organometallics* **2011**, *30*, 372–374.

(73) Vilella, L.; Vidossich, P.; Balcells, D.; Lledós, A. *Dalton Transactions* **2011**, *40*, 11241–11247.

(74) Karkas, M. D.; Verho, O.; Johnston, E. V.; Åkermark, B. *Chemical reviews* **2014**, *114*, 11863–12001.

(75) Muhler, M. *Berichte der Bunsengesellschaft für physikalische Chemie*, *101*, 1560–1560.

(76) Koper, M. T. *Journal of Solid State Electrochemistry* **2013**, *17*, 339–344.

(77) Sabatier, P.; La Catalyse en Chemie Organique, L. *Google Scholar* **1911**.

(78) Huynh, M.; Shi, C.; Billinge, S. J.; Nocera, D. G. *Journal of the American Chemical Society* **2015**, *137*, 14887–14904.

(79) Kuo, C.-H.; Li, W.; Pahalagedara, L.; El-Sawy, A. M.; Kriz, D.; Genz, N.; Guild, C.; Ressler, T.; Suib, S. L.; He, J. *Angewandte Chemie International Edition* **2015**, *54*, 2345–2350.

(80) Boppana, V. B. R.; Jiao, F. *Chemical Communications* **2011**, *47*, 8973–8975.

(81) Kim, J.; Kim, J. S.; Baik, H.; Kang, K.; Lee, K. *RSC Advances* **2016**, *6*, 26535–26539.

(82) Plaisance, C. P.; Reuter, K.; van Santen, R. A. *Faraday discussions* **2016**, *188*, 199–226.

(83) Bocca, C.; Cerisola, G.; Magnone, E.; Barbucci, A. *International Journal of Hydrogen Energy* **1999**, *24*, 699–707.

(84) Kim, N.-I.; Sa, Y. J.; Cho, S.-H.; So, I.; Kwon, K.; Joo, S. H.; Park, J.-Y. *Journal of The Electrochemical Society* **2016**, *163*, F3020–F3028.

(85) Smith, R. D.; Prévot, M. S.; Fagan, R. D.; Trudel, S.; Berlinguette, C. P. *Journal of the American Chemical Society* **2013**, *135*, 11580–11586.

(86) Liu, X.; Jia, H.; Sun, Z.; Chen, H.; Xu, P.; Du, P. *Electrochemistry Communications* **2014**, *46*, 1–4.

(87) Liu, X.; Cui, S.; Sun, Z.; Du, P. *Electrochimica Acta* **2015**, *160*, 202–208.

(88) Elumeeva, K.; Masa, J.; Sierau, J.; Tietz, F.; Muhler, M.; Schuhmann, W. *Electrochimica Acta* **2016**, *208*, 25–32.

(89) Sharpe, R.; Lim, T.; Jiao, Y.; Niemantsverdriet, J.; Gracia, J. *ChemCatChem* **2016**, *8*, 3762–3768.

(90) Seo, M. H.; Park, H. W.; Lee, D. U.; Park, M. G.; Chen, Z. *Acs Catalysis* **2015**, *5*, 4337–4344.

(91) May, K. J.; Carlton, C. E.; Stoerzinger, K. A.; Risch, M.; Suntivich, J.; Lee, Y.-L.; Grimaud, A.; Shao-Horn, Y. *The journal of physical chemistry letters* **2012**, *3*, 3264–3270.

(92) Burns, R. G.; Burns, R. G., *Mineralogical applications of crystal field theory*; Cambridge University Press: **1993**; Vol. 5.

(93) Nikolov, I.; Darkaoui, R.; Zhecheva, E.; Stoyanova, R.; Dimitrov, N.; Vitanov, T. *Journal of Electroanalytical Chemistry* **1997**, *429*, 157–168.

(94) Li, M.; Xiong, Y.; Liu, X.; Bo, X.; Zhang, Y.; Han, C.; Guo, L. *Nanoscale* **2015**, *7*, 8920–8930.

(95) Wang, H.-Y.; Hung, S.-F.; Chen, H.-Y.; Chan, T.-S.; Chen, H. M.; Liu, B. *Journal of the American Chemical Society* **2015**, *138*, 36–39.

(96) Singh, N.; Singh, R. **1999**.

(97) Al-Hoshan, M.; Singh, J.; Al-Mayouf, A.; Al-Suhybani, A.; Shaddad, M. *Int. J. Electrochem. Sci* **2012**, *7*, 4959–4973.

(98) Hirai, S.; Yagi, S.; Seno, A.; Fujioka, M.; Ohno, T.; Matsuda, T. *RSC advances* **2016**, *6*, 2019–2023.

(99) Frydendal, R.; Paoli, E. A.; Knudsen, B. P.; Wickman, B.; Malacrida, P.; Stephens, I. E.; Chorkendorff, I. *ChemElectroChem* **2014**, *1*, 2075–2081.

(100) Lee, Y.; Suntivich, J.; May, K. J.; Perry, E. E.; Shao-Horn, Y. *The journal of physical chemistry letters* **2012**, *3*, 399–404.

(101) Kötz, R.; Neff, H.; Stucki, S. *Journal of The Electrochemical Society* **1984**, *131*, 72–77.

(102) Cherevko, S.; Geiger, S.; Kasian, O.; Kulyk, N.; Grote, J.-P.; Savan, A.; Shrestha, B. R.; Merzlikin, S.; Breitbach, B.; Ludwig, A., et al. *Catalysis Today* **2016**, *262*, 170–180.

(103) Audichon, T.; Napporn, T. W.; Canaff, C.; Morais, C.; Comminges, C.; Kokoh, K. B. *The Journal of Physical Chemistry C* **2016**, *120*, 2562–2573.

(104) Fedlheim, D. L.; Foss, C. A., *Metal nanoparticles: synthesis, characterization, and applications*; CRC press: **2001**.

(105) Astruc, D., *Nanoparticles and catalysis*; John Wiley & Sons: **2008**.

(106) Rodríéguez, J. A.; Fernández-Garcíéa, M., *Synthesis, properties, and applications of oxide nanomaterials*; John Wiley & Sons: **2007**.

(109) Biswas, K.; Rao, C. *Journal of nanoscience and nanotechnology* **2007**, *7*, 1969–1974.

(110) Hsieh, C.-S.; Tsai, D.-S.; Chen, R.-S.; Huang, Y.-S. *Applied physics letters* **2004**, *85*, 3860–3862.

(111) Lee, S. W.; Gallant, B. M.; Byon, H. R.; Hammond, P. T.; Shao-Horn, Y. *Energy & Environmental Science* **2011**, *4*, 1972–1985.

(112) Bi, R.-R.; Wu, X.-L.; Cao, F.-F.; Jiang, L.-Y.; Guo, Y.-G.; Wan, L.-J. *The Journal of Physical Chemistry C* **2010**, *114*, 2448–2451.

(113) Min, M.; Machida, K.; Jang, J. H.; Naoi, K. *Journal of The Electrochemical Society* **2006**, *153*, A334–A338.

(114) Kimling, J.; Maier, M.; Okenve, B.; Kotaidis, V.; Ballot, H.; Plech, A. *The Journal of Physical Chemistry B* **2006**, *110*, 15700–15707.

(115) Philippot, K.; Chaudret, B. *Comptes Rendus Chimie* **2003**, *6*, 1019–1034.

(116) Pelzer, K.; Vidoni, O.; Philippot, K.; Chaudret, B.; Colliere, V. *Advanced Functional Materials* **2003**, *13*, 118–126.

(117) Ma, Z.; Zhang, Y.; Liu, S.; Xu, W.; Wu, L.; Hsieh, Y.-C.; Liu, P.; Zhu, Y.; Sasaki, K.; Renner, J. N., et al. *Journal of Electroanalytical Chemistry* **2018**, *819*, 296–305.

(118) Klepser, B. M.; Bartlett, B. M. *Journal of the American Chemical Society* **2014**, *136*, 1694–1697.

(119) Sheehan, S. W.; Thomsen, J. M.; Hintermair, U.; Crabtree, R. H.; Brudvig, G. W.; Schmuttenmaer, C. A. *Nature communications* **2015**, *6*, 6469.

(120) Lightcap, I. V.; Kosel, T. H.; Kamat, P. V. *Nano letters* **2010**, *10*, 577–583.

(121) Coperet, C.; Chabanas, M.; Petroff Saint-Arroman, R.; Basset, J.-M. *Angewandte Chemie International Edition* **2003**, *42*, 156–181.

(122) Candy, J.-P.; Copéret, C.; Basset, J.-M. In *Surface and Interfacial Organometallic Chemistry and Catalysis*; Springer: **2005**, pp 151–210.

(123) Wegener, S. L.; Marks, T. J.; Stair, P. C. *Accounts of chemical research* **2011**, *45*, 206–214.

(124) Serna, P.; Gates, B. C. *Accounts of chemical research* **2014**, *47*, 2612–2620.

(125) Qiao, B.; Wang, A.; Yang, X.; Allard, L. F.; Jiang, Z.; Cui, Y.; Liu, J.; Li, J.; Zhang, T. *Nature chemistry* **2011**, *3*, 634.

(126) Zhang, Y.; Wu, C.; Jiang, H.; Lin, Y.; Liu, H.; He, Q.; Chen, S.; Duan, T.; Song, L. *Advanced Materials* **2018**, *30*, 1707522.

(127) Liu, J.-C.; Ma, X.-L.; Li, Y.; Wang, Y.-G.; Xiao, H.; Li, J. *Nature communications* **2018**, *9*, 1610.

(128) Yan, H.; Lin, Y.; Wu, H.; Zhang, W.; Sun, Z.; Cheng, H.; Liu, W.; Wang, C.; Li, J.; Huang, X., et al. *Nature communications* **2017**, *8*, 1070.

(129) Ji, S.; Chen, Y.; Fu, Q.; Chen, Y.; Dong, J.; Chen, W.; Li, Z.; Wang, Y.; Gu, L.; He, W., et al. *Journal of the American Chemical Society* **2017**, *139*, 9795–9798.

(130) Over, H. *Chemical Reviews* **2012**, *112*, 3356–3426.

(131) Kuhlenbeck, H.; Shaikhutdinov, S.; Freund, H.-J. *Chemical reviews* **2013**, *113*, 3986–4034.

(132) Hess, F.; Over, H. *ACS Catalysis* **2016**, *7*, 128–138.

(133) Over, H.; Kim, Y. D.; Seitsonen, A.; Wendt, S.; Lundgren, E.; Schmid, M.; Varga, P.; Morgante, A.; Ertl, G. *Science* **2000**, *287*, 1474–1476.

(134) Fan, C. Y.; Wang, J.; Jacobi, K.; Ertl, G. *The Journal of Chemical Physics* **2001**, *114*, 10058–10062.

(135) López, N.; Gómez-Segura, J.; Marıén, R. P.; Pérez-Ramıérez, J. *Journal of Catalysis* **2008**, *255*, 29–39.

(136) Liu, H.; Iglesia, E. *The Journal of Physical Chemistry B* **2005**, *109*, 2155–2163.

(137) Teschner, D.; Farra, R.; Yao, L.; Schlögl, R.; Soerijanto, H.; Schomäcker, R.; Schmidt, T.; Szentmiklósi, L.; Amrute, A. P.; Mondelli, C., et al. *Journal of catalysis* **2012**, *285*, 273–284.

(138) Weaver, J. F. *Chemical reviews* **2013**, *113*, 4164–4215.

(139) Exner, K. S.; Anton, J.; Jacob, T.; Over, H. *Angewandte Chemie International Edition* **2014**, *53*, 11032–11035.

(140) Suen, N.-T.; Hung, S.-F.; Quan, Q.; Zhang, N.; Xu, Y.-J.; Chen, H. M. *Chemical Society Reviews* **2017**, *46*, 337–365.

(141) Jung, H.-G.; Jeong, Y. S.; Park, J.-B.; Sun, Y.-K.; Scrosati, B.; Lee, Y. J. *Acs Nano* **2013**, *7*, 3532–3539.

(142) Paoli, E. A.; Masini, F.; Frydendal, R.; Deiana, D.; Schlaup, C.; Malizia, M.; Hansen, T. W.; Horch, S.; Stephens, I. E.; Chorkendorff, I. *Chemical science* **2015**, *6*, 190–196.

(143) Reier, T.; Oezaslan, M.; Strasser, P. *Acs Catalysis* **2012**, *2*, 1765–1772.

(144) Over, H.; Muhler, M. *Progress in surface science* **2003**, *72*, 3–17.

(145) Reuter, K.; Scheffler, M. *Physical Review B* **2006**, *73*, 045433.

(146) Teschner, D.; Novell-Leruth, G.; Farra, R.; Knop-Gericke, A.; Schlögl, R.; Szentmiklósi, L.; Hevia, M. G.; Soerijanto, H.; Schomäcker, R.; Pérez-Ramıérez, J., et al. *Nature chemistry* **2012**, *4*, 739.

(147) Trasatti, S. *Electrochimica Acta* **2000**, *45*, 2377–2385.

(148) Zang, L.; Kisch, H. *Angewandte Chemie International Edition* **2000**, *39*, 3921–3922.

(149) Rolison, D. R.; Hagans, P. L.; Swider, K. E.; Long, J. W. *Langmuir* **1999**, *15*, 774–779.

(150) Paulus, U. A.; Wang, Y.; Kim, S. H.; Geng, P.; Wintterlin, J.; Jacobi, K.; Ertl, G. *The Journal of chemical physics* **2004**, *121*, 11301–11308.

(151) Nellist, M. R.; Laskowski, F. A.; Lin, F.; Mills, T. J.; Boettcher, S. W. *Accounts of chemical research* **2016**, *49*, 733–740.

(152) Henderson, M. A. *Surface Science Reports* **2002**, *46*, 1–308.

(153) Verdaguer, A.; Sacha, G.; Bluhm, H.; Salmeron, M. *Chemical reviews* **2006**, *106*, 1478–1510.

(154) Campbell, C. T.; Sellers, J. R. *Chemical reviews* **2013**, *113*, 4106–4135.

(155) Mu, R.; Zhao, Z.-j.; Dohnálek, Z.; Gong, J. *Chemical Society Reviews* **2017**, *46*, 1785–1806.

(156) Borgarello, E.; Kiwi, J.; Pelizzetti, E.; Visca, M.; Grätzel, M. *Nature* **1981**, *289*, 158.

(157) Zhao, Z.; Li, Z.; Zou, Z. *Physics Letters A* **2011**, *375*, 2939–2945.

(158) Gala, F.; Agosta, L.; Zollo, G. *The Journal of Physical Chemistry C* **2015**, *120*, 450–456.

(159) Zhao, Z.-J.; Li, Z.; Cui, Y.; Zhu, H.; Schneider, W. F.; Delgass, W. N.; Ribeiro, F.; Greeley, J. *Journal of Catalysis* **2017**, *345*, 157–169.

(160) Lobo, A.; Conrad, H. *Surface science* **2003**, *523*, 279–286.

(161) Chu, Y.; Lister, T.; Cullen, W.; You, H.; Nagy, Z. *Physical review letters* **2001**, *86*, 3364.

(162) Rao, R. R.; Kolb, M. J.; Halck, N. B.; Pedersen, A. F.; Mehta, A.; You, H.; Stoerzinger, K. A.; Feng, Z.; Hansen, H. A.; Zhou, H., et al. *Energy & Environmental Science* **2017**, *10*, 2626–2637.

(163) Mu, R.; Cantu, D. C.; Glezakou, V.-A.; Lyubinetsky, I.; Rousseau, R.; Dohnálek, Z. *The Journal of Physical Chemistry C* **2015**, *119*, 23552–23558.

(164) Mu, R.; Cantu, D. C.; Lin, X.; Glezakou, V.-A.; Wang, Z.; Lyubinetsky, I.; Rousseau, R.; Dohnálek, Z. *The journal of physical chemistry letters* **2014**, *5*, 3445–3450.

(165) Keilbart, N.; Okada, Y.; Feehan, A.; Higai, S.; Dabo, I. *Physical Review B* **2017**, *95*, 115423.

(166) Siahrostami, S.; Vojvodic, A. *The Journal of Physical Chemistry C* **2014**, *119*, 1032–1037.

(167) Wirth, J.; Monturet, S.; Klamroth, T.; Saalfrank, P. *EPL (Europhysics Letters)* **2011**, *93*, 68001.

(168) Nguyen, M.-T.; Mu, R.; Cantu, D. C.; Lyubinetsky, I.; Glezakou, V.-A.; Dohnalek, Z.; Rousseau, R. *The Journal of Physical Chemistry C* **2017**, *121*, 18505–18515.

(169)   Rao, R. R.; Kolb, M. J.; Hwang, J.; Pedersen, A. F.; Mehta, A.; You, H.; Stoerzinger, K. A.; Feng, Z.; Zhou, H.; Bluhm, H., et al. *The Journal of Physical Chemistry C* **2018**, *122*, 17802–17811.

(170)   Valdes, A.; Brillet, J.; Grätzel, M.; Gudmundsdottir, H.; Hansen, H. A.; Jonsson, H.; Klüpfel, P.; Kroes, G.-J.; Le Formal, F.; Man, I. C., et al. *Physical Chemistry Chemical Physics* **2012**, *14*, 49–70.

(171)   Rossmeisl, J.; Logadottir, A.; Nørskov, J. K. *Chemical physics* **2005**, *319*, 178–184.

(172)   Hansen, H. A.; Man, I. C.; Studt, F.; Abild-Pedersen, F.; Bligaard, T.; Rossmeisl, J. *Physical Chemistry Chemical Physics* **2010**, *12*, 283–290.

(173)   Koper, M. T. *Journal of Electroanalytical Chemistry* **2011**, *660*, 254–260.

(174)   Man, I. C.; Su, H.-Y.; Calle-Vallejo, F.; Hansen, H. A.; Martıénez, J. I.; Inoglu, N. G.; Kitchin, J.; Jaramillo, T. F.; Nørskov, J. K.; Rossmeisl, J. *ChemCatChem* **2011**, *3*, 1159–1165.

(175)   Stamenkovic, V.; Mun, B. S.; Mayrhofer, K. J.; Ross, P. N.; Markovic, N. M.; Rossmeisl, J.; Greeley, J.; Nørskov, J. K. *Angewandte Chemie* **2006**, *118*, 2963–2967.

(176)   Kitchin, J.; Nørskov, J. K.; Barteau, M.; Chen, J. *The Journal of chemical physics* **2004**, *120*, 10240–10246.

(177)   Mavrikakis, M.; Hammer, B.; Nørskov, J. K. *Physical Review Letters* **1998**, *81*, 2819.

(178)   Bligaard, T.; Nørskov, J. K. *Electrochimica Acta* **2007**, *52*, 5512–5516.

(179)   Calle-Vallejo, F.; Inoglu, N. G.; Su, H.-Y.; Martıénez, J. I.; Man, I. C.; Koper, M. T.; Kitchin, J. R.; Rossmeisl, J. *Chemical Science* **2013**, *4*, 1245–1249.

(180)   Kuo, D.-Y.; Kawasaki, J. K.; Nelson, J. N.; Kloppenburg, J.; Hautier, G.; Shen, K. M.; Schlom, D. G.; Suntivich, J. *Journal of the American Chemical Society* **2017**, *139*, 3473–3479.

(181)   Griffiths, D. J., *Introduction to quantum mechanics*; Prentice Hall: **2018**.

(182)   Born, M.; Oppenheimer, R. *Annalen der physik* **1927**, *389*, 457–484.

(183)   Attila Szabo, N. S. O., *Modern Quantum Chemistry: Intro to Advanced Electronic Structure Theory*; Dover Publications: **1996**.

(184)   Jensen, F., *Introduction to Computational Chemistry*; John Wiley and Sons: **2017**.

(185)   Bartlett, R. J.; Stanton, J. F. *Reviews in computational chemistry* **1994**, 65–169.

(186)   Hohenberg, P.; Kohn, W. *Physical review* **1964**, *136*, B864.

(188)   Vosko, S. H.; Wilk, L.; Nusair, M. *Canadian Journal of physics* **1980**, *58*, 1200–1211.

(189)   Becke, A. D. *Physical review A* **1988**, *38*, 3098.

(190)   Perdew, J. P.; Burke, K.; Ernzerhof, M. *Physical review letters* **1996**, *77*, 3865.

(191)   Tao, J.; Perdew, J. P.; Staroverov, V. N.; Scuseria, G. E. *Physical Review Letters* **2003**, *91*, 146401.

(192)   Raghavachari, K. *Theoretical Chemistry Accounts* **2000**, *103*, 361–363.

(193)   Adamo, C.; Barone, V. *The Journal of chemical physics* **1999**, *110*, 6158–6170.

(194)   Grimme, S. *Journal of Computational Chemistry* **2004**, *25*, 1463–1473.

(195)   D.E., S., *Introduction to crystallography*; Dover Classics of Science & Mathematics; Dover: **1994**.

(196)   Hammond, C., *The Basics of Crystallography and Diffraction*; International Lunion of Crystallography Texts on Crystallography; OUP: **2009**.

(197)   Churchill, J.; Holmstrom, F. *American Journal of Physics* **1982**, *50*, 848–854.

(198)   Neil W.(Neil W. Ashcroft) Ashcroft, N. D. M., *Solid state physics*; Holt, Rinehart and Winston: **1976**.

(199)   Slater, J. C. *Physical Review* **1930**, *36*, 57.

(200)   Boys, S. F. *Proceedings of the Royal Society of London. Series A. Mathematical and Physical Sciences* **1950**, *200*, 542–554.

(201)   Pahl, F. A.; Handy, N. C. *Molecular Physics* **2002**, *100*, 3199–3224.

(202)   Pickett, W. E. *Computer Physics Reports* **1989**, *9*, 115–197.

(203)   Blöchl, P. E. *Physical review B* **1994**, *50*, 17953.

(204)   Pulay, P. *Molecular Physics* **1969**, *17*, 197–204.

(205)   Teter, M. P.; Payne, M. C.; Allan, D. C. *Phys. Rev. B* **1989**, *40*, 12255–12263.

(206)   Bylander, D. M.; Kleinman, L.; Lee, S. *Phys. Rev. B* **1990**, *42*, 1394–1403.

(207)   Henkelman, G.; Jónsson, H. *The Journal of chemical physics* **2000**, *113*, 9978–9985.

(208)   Henkelman, G.; Uberuaga, B. P.; Jónsson, H. *The Journal of chemical physics* **2000**, *113*, 9901–9904.

(209)   Roux, B.; Simonson, T. *Biophysical chemistry* **1999**, *78*, 1–20.

(210)   Baker, N. A. *Reviews in computational chemistry* **2005**, *21*, 349.

(211)   Cramer, C. J., *Essentials of Computational Chemistry: Theories and Models*; John Wiley and Sons: **2004**.

(212)   Dominik Marx, J. H., *Ab initio molecular dynamics: basic theory and advanced methods*; Cambridge University Press: **2009**.

(213)   Tuckerman, M. E., *Statistical Mechanics: Theory and Molecular Simulation*; Oxford Graduate Texts; Oxford University Press, USA: **2010**.

(214)   Kresse, G.; Hafner, J. *Physical Review B* **1993**, *47*, 558–561.

(215)   Kresse, G.; Furthmüller, J. *Physical Review B - Condensed Matter and Materials Physics* **1996**, *54*, 11169–11186.

(216)   Kresse, G. *Physical Review B - Condensed Matter and Materials Physics* **1999**, *59*, 1758–1775.

(217)   Perdew, J.; Burke, K.; Ernzerhof, M. *Physical Review Letters* **1996**, *77*, 3865–3868.

(218)   Monkhorst, H.; Pack, J. *Physical Review B* **1976**, *13*, 5188–5192.

(219)   Ugliengo, P.; Viterbo, D.; Chiari, G. *Zeitschrift fur Kristallographie - New Crystal Structures* **1993**, *207*, 9–23.

(220)   Henkelman, G.; Uberuaga, B.; Jónsson, H. *Journal of Chemical Physics* **2000**, *113*, 9901–9904.

(221)   Henkelman, G.; Jónsson, H. *Journal of Chemical Physics* **2000**, *113*, 9978–9985.

(222)   Sheppard, D.; Terrell, R.; Henkelman, G. *Journal of Chemical Physics* **2008**, *128*.

(223)   Seitsonen, A.; Over, H. *High Performance Computing in Science and Engineering in Munich 2002* **2003**, 171–180.

(224)   Baur, W.; Khan, A. *Acta Crystallogr.* **1971**, *27*, 2133–2139.

(225)   Huang, Y.; Park, H.; Pollak, F. *Materials Research Bulletin* **1982**, *17*, 1305–1312.

(226)   Dovesi, R.; Orlando, R.; Erba, A.; Zicovich-Wilson, C. M.; Civalleri, B.; Casassa, S.; Maschio, L.; Ferrabone, M.; De La Pierre, M.; d'Arco, P., et al. *International Journal of Quantum Chemistry* **2014**, *114*, 1287–1317.

(227)   Berlijn, T.; Snijders, P. C.; Delaire, O.; Zhou, H.-D.; Maier, T. A.; Cao, H.-B.; Chi, S.-X.; Matsuda, M.; Wang, Y.; Koehler, M. R., et al. *Physical review letters* **2017**, *118*, 077201.

(228)   Ping, Y.; Galli, G.; Goddard III, W. A. *The Journal of Physical Chemistry C* **2015**, *119*, 11570–11577.

(229)   Dıéaz, C.; Valenzuela, M.; Spodine, E.; Moreno, Y.; Peña, O. *Journal of Cluster Science* **2007**, *18*, 831–844.

(230)   Cotton, F.; Mague, J. *Inorganic Chemistry* **1966**, *5*, 317–318.

(231)   Kim, Y.; Over, H.; Krabbes, G.; Ertl, G. *Topics in Catalysis* **2000**, *14*, 95–100.

(232) Kim, Y.; Schwegmann, S.; Seitsonen, A.; Over, H. *Journal of Physical Chemistry B* **2001**, *105*, 2205–2211.

(233) Novell-Leruth, G.; Carchini, G.; López, N. *Journal of Chemical Physics* **2013**, *138*.

(234) Gibbs, J. W. **1879**.

(235) Wulff, G. *Zeitschrift für Kristallographie-Crystalline Materials* **1901**, *34*, 449–530.

(236) Viñes, F.; Loschen, C.; Illas, F.; Neyman, K. M. *Journal of Catalysis* **2009**, *266*, 59–63.

(237) Tang, W.; Sanville, E.; Henkelman, G. *Journal of Physics: Condensed Matter* **2009**, *21*, 084204.

(238) Mathew, K.; Sundararaman, R.; Letchworth-Weaver, K.; Arias, T.; Hennig, R. *Journal of Chemical Physics* **2014**, *140*.

(239) Grätzel, M. *nature* **2001**, *414*, 338.

(240) Rossmeisl, J.; Qu, Z.-W.; Zhu, H.; Kroes, G.-J.; Nørskov, J. K. *Journal of Electro-analytical Chemistry* **2007**, *607*, 83–89.

(241) Trasatti, S. *Electrochimica Acta* **1984**, *29*, 1503–1512.

(242) Stoerzinger, K. A.; Diaz-Morales, O.; Kolb, M.; Rao, R. R.; Frydendal, R.; Qiao, L.; Wang, X. R.; Halck, N. B.; Rossmeisl, J.; Hansen, H. A., et al. *ACS Energy Letters* **2017**, *2*, 876–881.

(243) Stoerzinger, K. A.; Rao, R. R.; Wang, X. R.; Hong, W. T.; Rouleau, C. M.; Shao-Horn, Y. *Chem* **2017**, *2*, 668–675.

(244) Roy, C.; Rao, R. R.; Stoerzinger, K. A.; Hwang, J.; Rossmeisl, J.; Chorkendorff, I.; Shao-Horn, Y.; Stephens, I. E. *ACS Energy Letters* **2018**, *3*, 2045–2051.

(245) Fang, Y.-H.; Liu, Z.-P. *Journal of the American Chemical Society* **2010**, *132*, 18214–18222.

(246) Torun, E.; Fang, C.; De Wijs, G.; De Groot, R. *The Journal of Physical Chemistry C* **2013**, *117*, 6353–6357.

(247) Ping, Y.; Nielsen, R. J.; Goddard III, W. A. *Journal of the American Chemical Society* **2016**, *139*, 149–155.

(248) Dickens, C. F.; Nørskov, J. K. *The Journal of Physical Chemistry C* **2017**, *121*, 18516–18524.

(249) Liu, P.; Zhao, Y.; Qin, R.; Mo, S.; Chen, G.; Gu, L.; Chevrier, D. M.; Zhang, P.; Guo, Q.; Zang, D., et al. *Science* **2016**, *352*, 797–800.

(250) Peterson, E. J.; DeLaRiva, A. T.; Lin, S.; Johnson, R. S.; Guo, H.; Miller, J. T.; Kwak, J. H.; Peden, C. H.; Kiefer, B.; Allard, L. F., et al. *Nature communications* **2014**, *5*, 4885.

(251) DeRita, L.; Resasco, J.; Dai, S.; Boubnov, A.; Thang, H. V.; Hoffman, A. S.; Ro, I.; Graham, G. W.; Bare, S. R.; Pacchioni, G., et al. *Nature materials* **2019**, 1.

(252) Gu, J.; Hsu, C.-S.; Bai, L.; Chen, H. M.; Hu, X. *Science* **2019**, *364*, 1091–1094.

(253) Liu, M.; Wang, L.; Zhao, K.; Shi, S.; Shao, Q.; Zhang, L.; Sun, X.; Zhao, Y.; Zhang, J. *Energy & Environmental Science* **2019**, *12*, 2890–2923.

(254) Xiao, M.; Zhu, J.; Li, G.; Li, N.; Li, S.; Cano, Z. P.; Ma, L.; Cui, P.; Xu, P.; Jiang, G., et al. *Angewandte Chemie* **2019**, *131*, 9742–9747.

(255) Lee, B.-H.; Park, S.; Kim, M.; Sinha, A. K.; Lee, S. C.; Jung, E.; Chang, W. J.; Lee, K.-S.; Kim, J. H.; Cho, S.-P., et al. *Nature materials* **2019**, *18*, 620.

(256) Daelman, N.; Capdevila-Cortada, M.; López, N. *Nature materials* **2019**.

(257) Garcíéa-Mota, M.; Vojvodic, A.; Metiu, H.; Man, I. C.; Su, H.-Y.; Rossmeisl, J.; Nørskov, J. K. *ChemCatChem* **2011**, *3*, 1607–1611.

(258) Zhao, Y.; Yang, K. R.; Wang, Z.; Yan, X.; Cao, S.; Ye, Y.; Dong, Q.; Zhang, X.; Thorne, J. E.; Jin, L., et al. *Proceedings of the National Academy of Sciences* **2018**, *115*, 2902–2907.

(259) Zhao, Y.; Yan, X.; Yang, K. R.; Cao, S.; Dong, Q.; Thorne, J. E.; Materna, K. L.; Zhu, S.; Pan, X.; Flytzani-Stephanopoulos, M., et al. *ACS central science* **2018**, *4*, 1166–1172.

(260) Zhu, C.; Shi, Q.; Feng, S.; Du, D.; Lin, Y. *ACS Energy Letters* **2018**, *3*, 1713–1721.

(261) Fei, H.; Dong, J.; Feng, Y.; Allen, C. S.; Wan, C.; Volosskiy, B.; Li, M.; Zhao, Z.; Wang, Y.; Sun, H., et al. *Nature Catalysis* **2018**, *1*, 63.

(262) Oh, H.-S.; Nong, H. N.; Reier, T.; Bergmann, A.; Gliech, M.; Ferreira de Araújo, J.; Willinger, E.; Schlögl, R.; Teschner, D.; Strasser, P. *Journal of the American Chemical Society* **2016**, *138*, 12552–12563.

(263) Abbott, D. F.; Lebedev, D.; Waltar, K.; Povia, M.; Nachtegaal, M.; Fabbri, E.; Copéret, C.; Schmidt, T. J. *Chemistry of Materials* **2016**, *28*, 6591–6604.

(264) Lettenmeier, P.; Majchel, J.; Wang, L.; Saveleva, V.; Zafeiratos, S.; Savinova, E.; Gallet, J.-J.; Bournel, F.; Gago, A.; Friedrich, K. *Chemical science* **2018**, *9*, 3570–3579.

(265) Fu, L.; Zeng, X.; Huang, C.; Cai, P.; Cheng, G.; Luo, W. *Inorganic Chemistry Frontiers* **2018**, *5*, 1121–1125.

(266) Agoston, P.; Albe, K. *Physical Review B* **2011**, *84*, 045311.

(267) Walsh, A.; Catlow, C. R. A. *Journal of Materials Chemistry* **2010**, *20*, 10438–10444.

(268) Svensson, M.; Humbel, S.; Froese, R. D.; Matsubara, T.; Sieber, S.; Morokuma, K. *The Journal of Physical Chemistry* **1996**, *100*, 19357–19363.

(269) Karton, A.; Tarnopolsky, A.; Lamere, J.-F.; Schatz, G. C.; Martin, J. M. *The Journal of Physical Chemistry A* **2008**, *112*, 12868–12886.

(270) Neese, F. *Wiley Interdisciplinary Reviews: Computational Molecular Science* **2012**, *2*, 73–78.

(271) Weigend, F.; Ahlrichs, R. *Physical Chemistry Chemical Physics* **2005**, *7*, 3297–3305.

(272) Liao, R.-Z.; Siegbahn, P. E. *ACS Catalysis* **2014**, *4*, 3937–3949.

Appendices

Appendix A

From Surfaces to Nanoparticles

Table A.1: Cell parameters (a, b and volume) and potential energy of the RuO_2 unit cell as function of the energy cut-off. All calculations are done with the PBE functional and a k-point mesh of 5x5x5.

Cut-Off[a]	a[b]	c[b]	Ratio c/a	Cell Vol.	E[d]
200	4.4878	3.1705	0.707	63.86	-45.9043
400	4.4983	3.1281	0.695	63.30	-44.3524
500	4.5432	3.1372	0.691	64.75	-44.2931
600	4.5452	3.1371	0.690	64.81	-44.3023
800	4.5458	3.1369	0.690	64.82	-44.3189

(a) in eV; (b) in Å; (c) in $Å^3$; (d) in eV.

Table A.2: Cell parameters (a, b and volume) and potential energy of the RuO_2 unit cell as function of the K-point mesh. All calculations are done with the PBE functional and a cut-off of 500eV.

K-Points	a[a]	c[a]	Ratio c/a	Cell Vol.[d]	E[e]
5x5x5	4.5432	3.1372	0.6905	64.75	-44.2931
8x8x8	4.5436	3.1370	0.6904	64.75	-44.2973
10x10x10	4.5433	3.1377	0.6906	64.77	-44.2991
15x15x15	4.5420	3.1375	0.6908	64.73	-44.2986
30x30x30	4.5431	3.1375	0.6906	64.76	-44.2986

(a) in Å; (d) in $Å^3$; (e) in eV.

Appendix B

RuO$_2$-H$_2$O Interface

Table B.1: Adsorption energies (in $kJ\,mol^{-1}$) of wat and dis structures on (110) surface with PBE-D2 and PBE-D3 level of theory. $\Delta(D3 - D2)$ stands for the energy difference between the two methodologies and $\Delta(dis - wat)$ stands for the energy difference between the two structures.

Structure	$E_{ads}(D2)$	$E_{ads}(D3)$	$\Delta(D3 - D2)$
wat	-128.1	-125.6	-2.5
dis	-137.2	-134.5	-2.6
Δ**(dis-wat)**	-9.1	-8.9	-0.2

Table B.2: Potential energy (eV) and vibrational mode and frequency (cm^{-1}) associated with the imaginary frequency.

Surface	Energy	Vibrational Mode	Frequency cm^{-1}
(1 1 0)	-738.490		-748.48
(1 0 0)	-646.639	$O_w \cdots H_{transf.}$ Stretching	-415.50
(0 1 1)	-733.117		-166.88
(0 0 1)	-640.200		-419.97
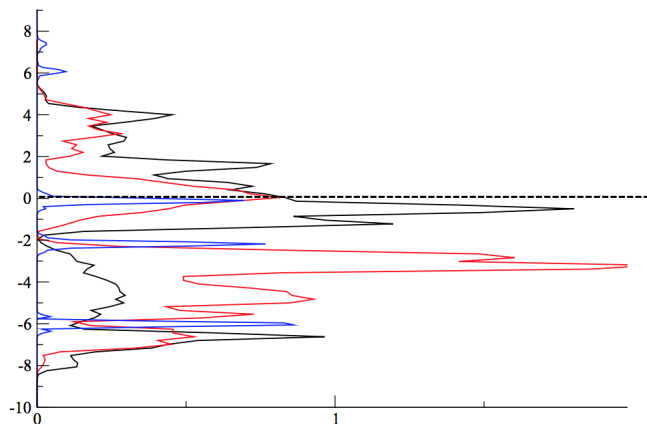
Figure B.1: Projected Density of States (pDOS) of the 4d orbitals of ruthenium unsaturated centers (black line) and 2p orbitals of oxygen bridge atoms of the surface (red line) of the (110) clean surface. The orbitals of the isolated molecular water (blue line) are added for comparison. Interaction is established between the occupied orbitals of water and the empty orbitals of ruthenium atoms.
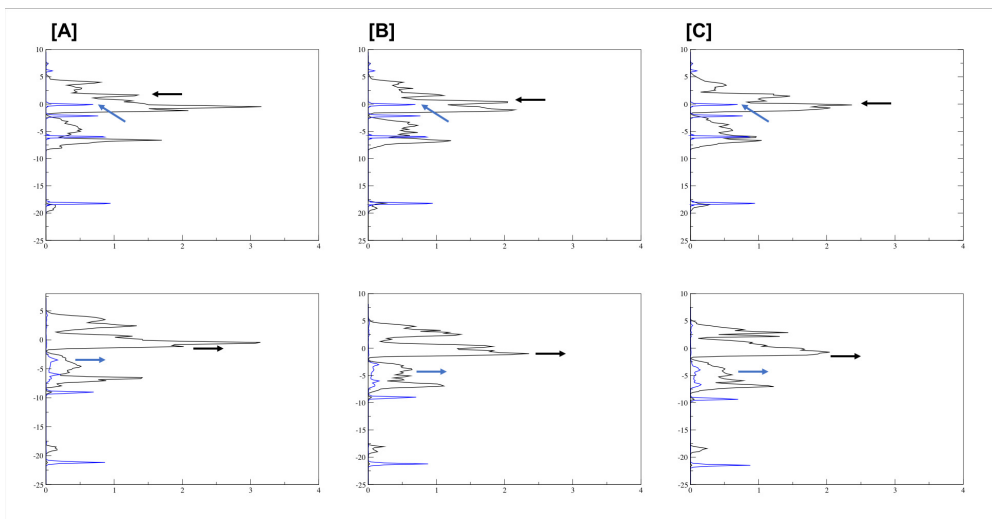
Figure B.2: Projected Density of States (pDOS) of the 4d orbitals of ruthenium unsaturated centers of the clean surface (black line), in which the orbitals of the isolated molecular water (blue line) are also added (top) and the pDOS of the wat structure when considering the adsorption of a single water molecule (bottom). [a] (110) surface; [b] (100) surface and [c] (011) surface.
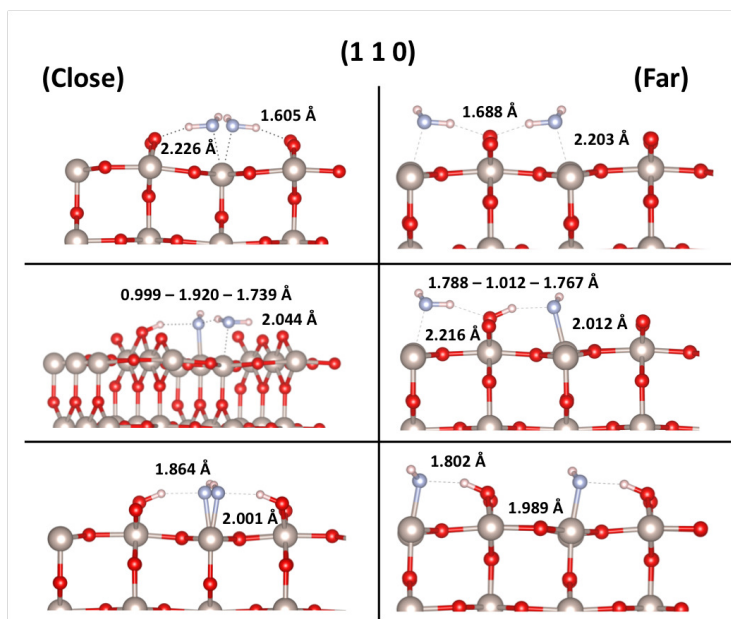
Figure B.3: Optimized geometries of all structures associated with the adsorption of half monolayer of water on the (110) RuO_2 surface.
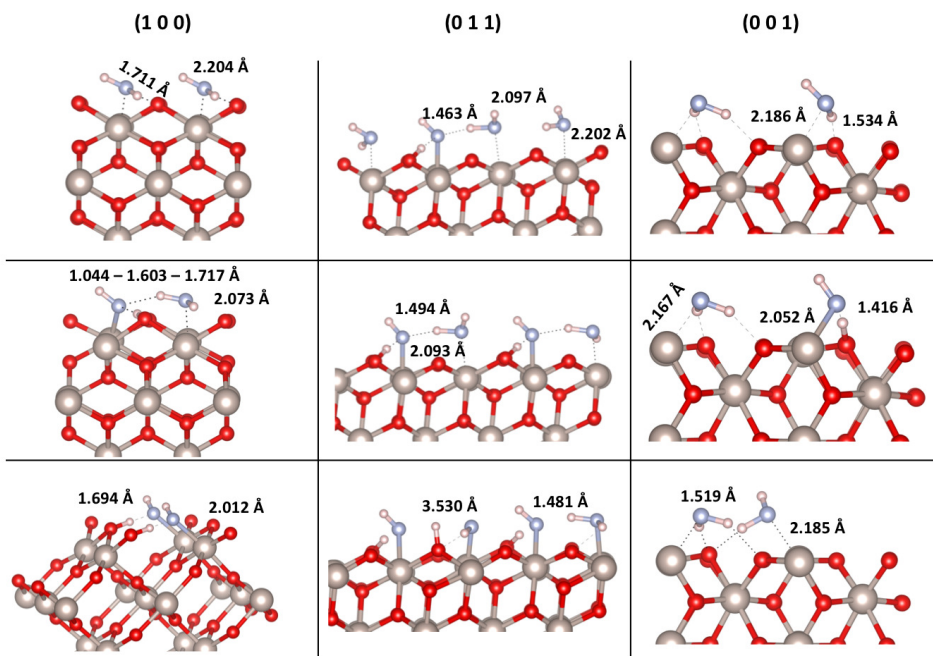
Figure B.4: Optimized geometries of all structures associated with the adsorption of half monolayer of water (011), (100) and (001) RuO_2 surfaces.
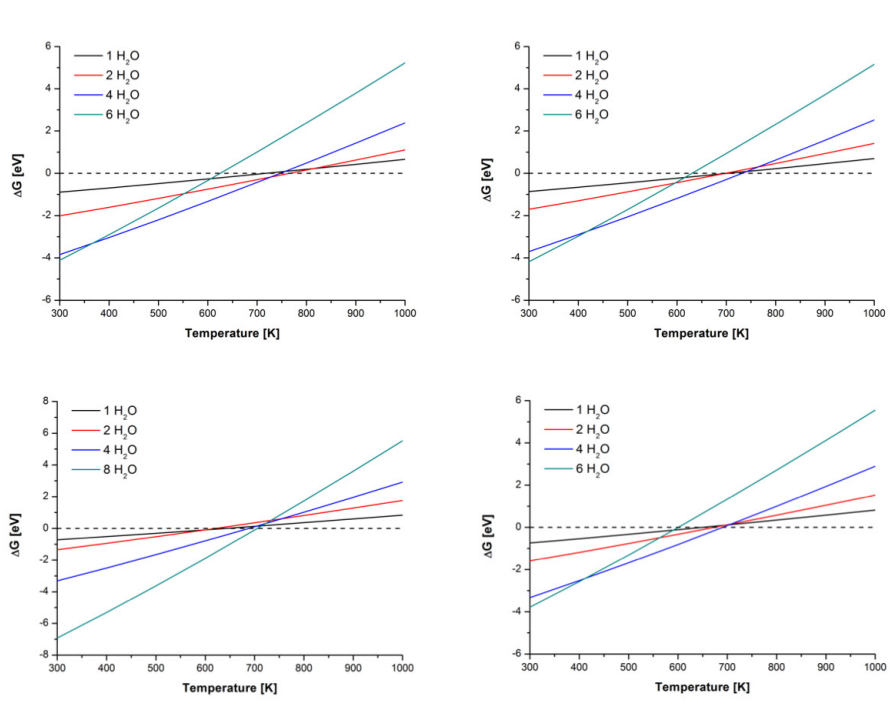
Figure B.5: Water coverage stability as function of temperature at 1 bar.

Table B.3: Water adsorption energies (in $kJ\,mol^{-1}$) at the (110) and (011) surface for one single water molecule and for the full monolayer coverage with and without inclusion of solvent effects with the implicit continuum model. $\Delta(E_{ads}(solv) - E_{ads}))$ stands for the energy difference between the two methodologies and $\Delta(dis - wat)$ stands for the energy difference between the two compared structures.

Structure	E_{ads}	$E_{ads}(solv)$	$\Delta(E_{ads}(solv) - E_{ads})$
		$\Theta = 1/4$	
110-wat	-128.1	-98.7	+29.3
110-dis	-137.2	-103.1	+34.1
Δ(dis-wat)	-9.1	-4.3	+4.8
100-wat	-129.9	-102.2	+27.7
100-dis	-115.3	-80.2	+35.1
Δ(dis-wat)	+14.6	+22.0	+7.4
		$\Theta = 4/4$	
110-4wat	-138.0	-100.5	+37.5
110-2wat∕2dis	-147.7	-109.0	+38.7
Δ(dis-wat)	-9.7	-8.5	+1.2
100-4wat	-135.4	-103.1	+33.0
100-3wat∕1dis	-136.2	-101.7	+35.3
Δ(dis-wat)	-0.8	+1.4	+2.2
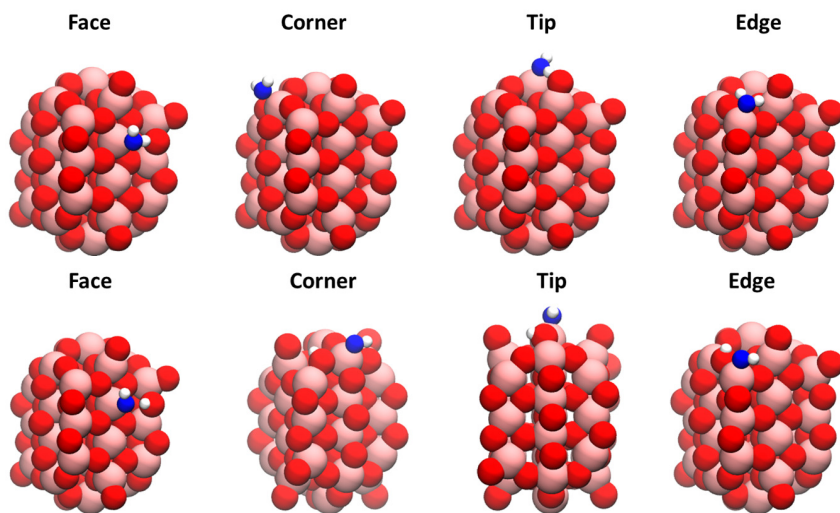
Figure B.6: Optimized geometries of the *wat* and *dis* form on the different locations (1.20 nm model).

Table B.4: Adsorption energies ($kJ \cdot mol^{-1}$) and structural parameters of water interaction on 1.20 nm nanoparticle size.

Site	Configuration	$\mathbf{E}_{ads}$	O_W-H_{W1}	O_W-H_{W2}	$Ru-O_W$	$\mu(Ru)$	$\mu(O_W)$
Face	*wat*	-109.9	0.975	1.082	2.150	-0.006	-0.001
	dis	-137.0	0.976	1.868	1.979	0.108	0.011
Corner	*wat*	-98.4	0.977	0.975	2.188	-0.125	0.00
	dis	-89.7	0.977	2.539	1.935	-0.008	-0.001
Tip	*wat*	-129.3	0.974	1.033	2.126	-0.065	-0.001
	dis	-138.9	0.983	2.502	1.899	-0.018	0.0
Edge	*wat*	-91.7	0.980	0.978	2.212	-0.006	0.00
	dis	-106.1	0.983	2.997	1.902	0.031	-0.001

Appendix C

Oxygen Evolution Reaction

Table C.1: ΔG (non spin-polarized) of WNA mechanism on each RuO$_2$ surface (in eV). Computed overpotential (η^{OER}) in Volts

Step	Reaction	(110)	(100)	(011)	(001)
W(1)	$H_2O^* \rightarrow OH^* + (H^+ + e^-)$	1.42	1.33	1.25	0.84
W(2)	$OH^* \rightarrow O^* + (H^+ + e^-)$	1.43	1.46	1.12	1.33
W(3)	$O^* + H_2O \rightarrow OOH^* + (H^+ + e^-)$	1.29	1.10	-	1.49
W(4)	$OOH^* + H_2O \rightarrow H_2O^* + O_2 \uparrow$	0.85	1.05	-	1.26
η^{OER}		0.36	0.23	-	0.10
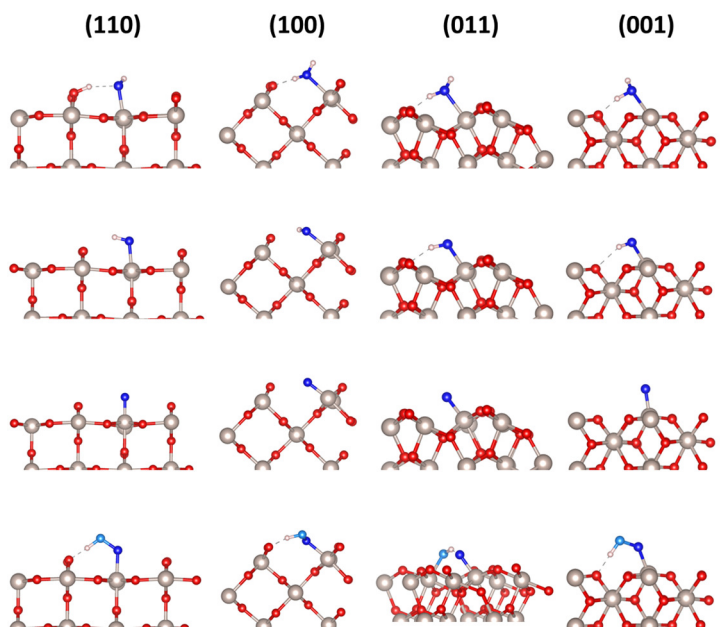
Figure C.1: WNA intermediates for the (110), (100), (011) and (001).
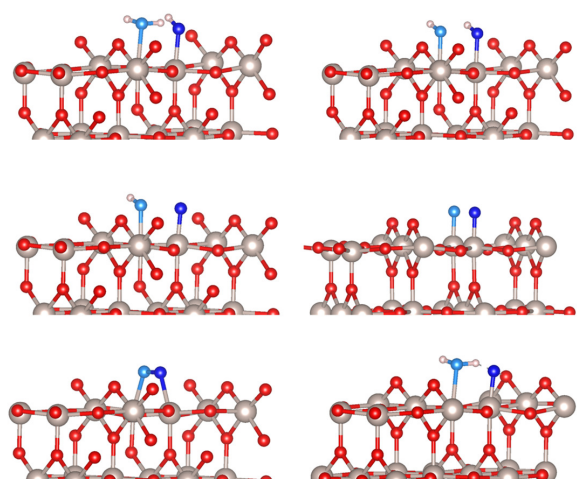
Figure C.2: I2M intermediates for the (110).
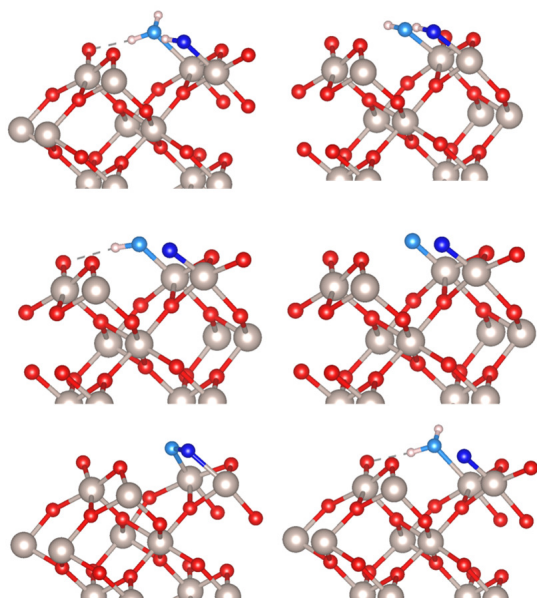
Figure C.3: I2M intermediates for the (100).
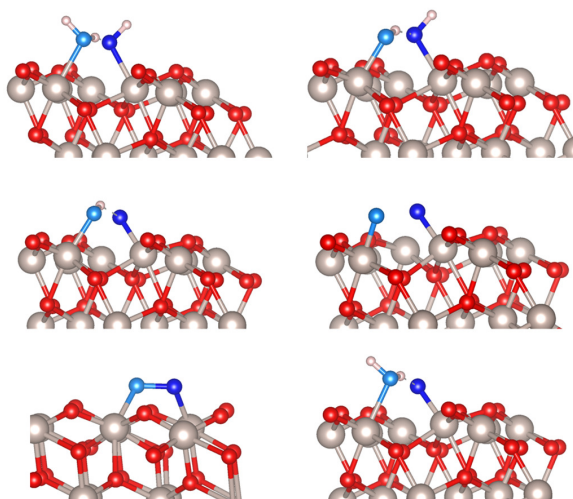
Figure C.4: I2M intermediates for the (011).
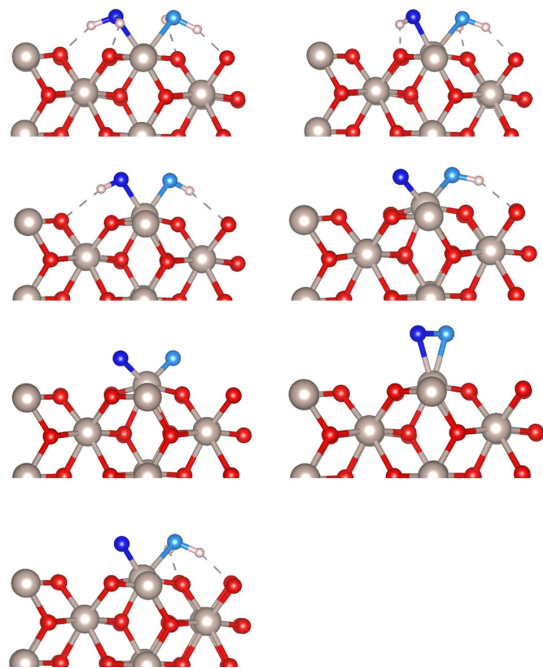
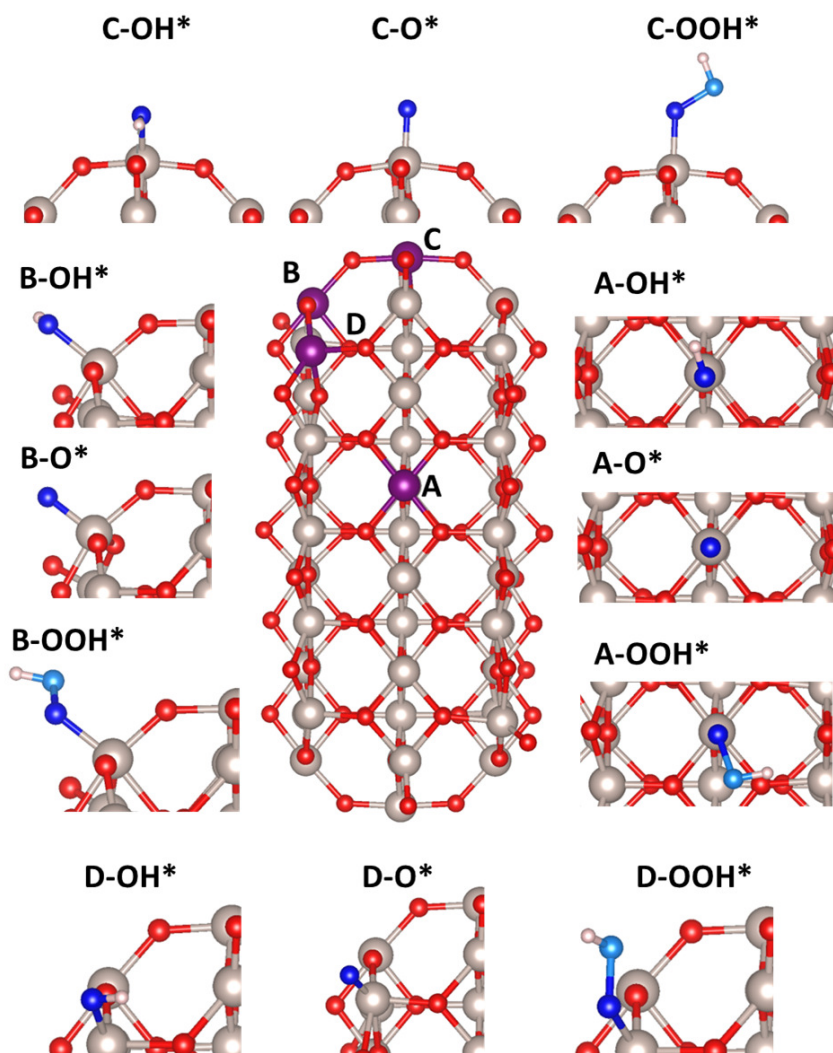**Figure C.5:** I2M intermediates for the (001).

Figure C.6: WNA intermediates for the 1.80 nm nanoparticle model on Face (A), Corner (B), Tip (C) and Edge (D).
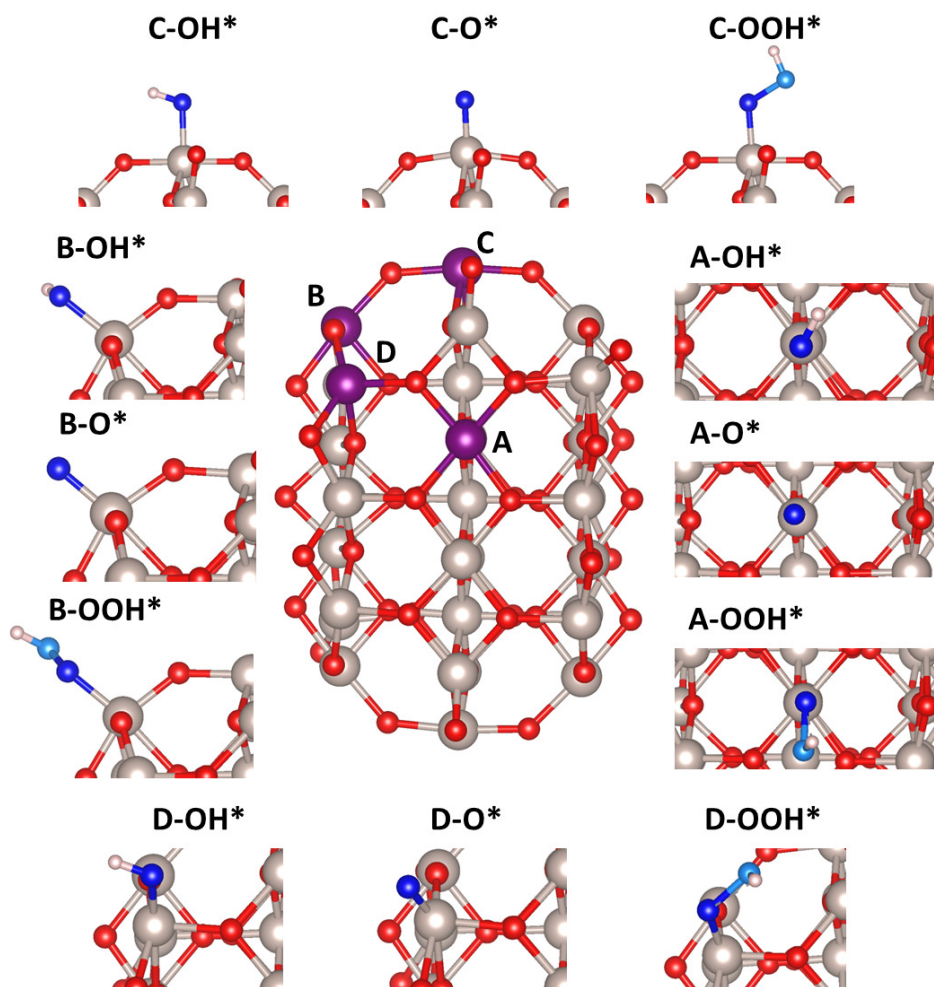
Figure C.7: WNA intermediates for the 1.20 nm nanoparticle model on Face (A), Corner (B), Tip (C) and Edge (D).
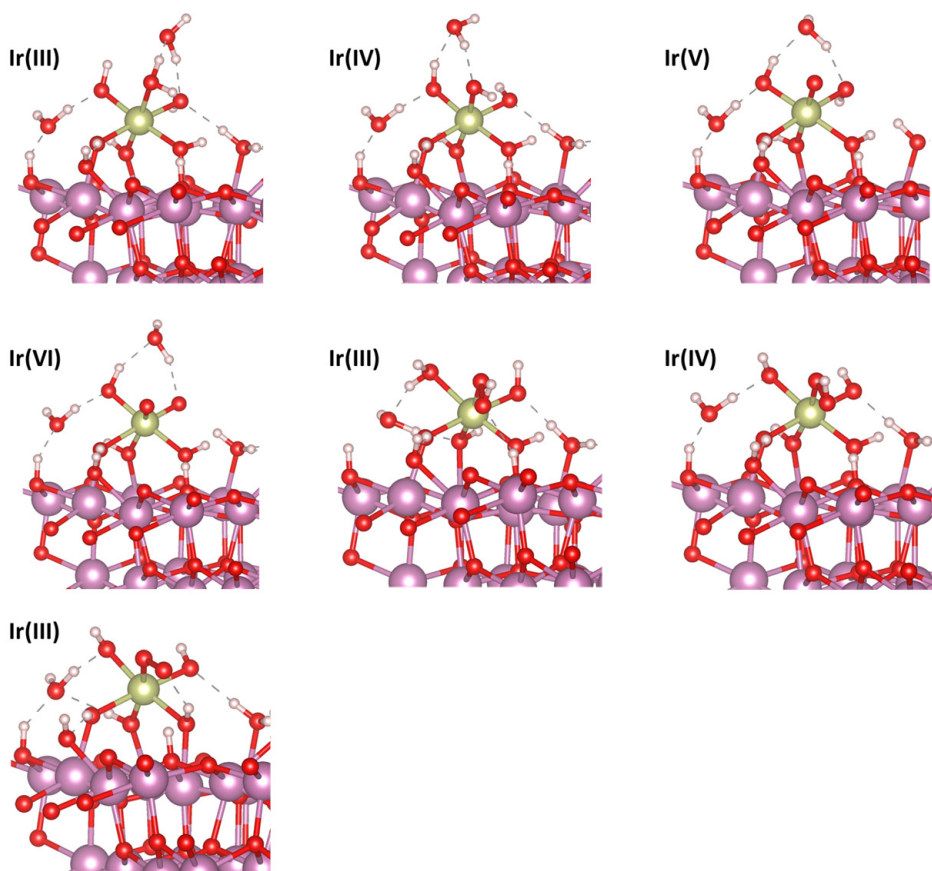
Appendix D

Single Site Ir@ITO Catalyst

Figure D.1: $Ir_{SAC}-ITO$ intermediate geometries.

Acknowledgements

Throughout the writing of this thesis I have received a great deal of support and assistance. I would first like to express my special appreciation and thanks to my supervisors, Prof. Dr. Mariona Sodupe and Dr. Xavier Solans, whose expertise was invaluable in the formulating of the research topic and methodology in particular. Further, thanks to Dr. Luis Rodriguez for the trust on me along the teaching requirements that we have shared together and rewarding research discussions along this period and to Dr. Albert Rimola also for the discussion and support.

Besides my supervisors, I would like to thank Prof. Dr. Christophe Copéret, Dr. Aleix Comas and Dr. Dmitry Lebedev for the nice and fruitful collaboration and to give me the opportunity to join their team at the (ETH-Hönggerberg, Zürich). In particular, I would like to express my gratitude to Dr. Aleix Comas and his family for their warm welcome and help during my stay in Switzerland. I will always remember those coffees at *Bistro* after lunch, the *Crazy-Tuesdays* and all the dinners that we enjoyed together. Finally, I express my sincere thanks to Dr. Jose Aleman and Dr. Ruben Mas from the Universidad Autónoma de Madrid and Dr. Miquel Pruneda and Dr. Ramon Cuadrado from ICN2 for the collaborations carried out during this period.

The following step is mentioning my colleagues from my and the other groups, whom I thank for the daily knowledge sharing, but also for the coffees and the lunchtimes always enjoyed together. Beyond the academic scope, I will remember my good friends Sergi, Giuseppe, Jose, Joan, Danilo, Stefano and Sonia for the Rick's Dinner and colombian food in Cerdanyola and for the time spent after work, by means of beers and laughs in the Plaça Cívica.

Continuing with my colleagues, I have to thank Anna Cebrián and Pablo for their help in organizing together the unity Christmas dinners, Gantulga for the laughs during the lunchtimes, to our *sysadmin* Sergi for the fast solutions to the technical problems and for the conversations about political matters and to Giuseppe for the work marathons during holidays and for the *criminal script* that we build to send hundreds of calculations in one shot.

A mention to our recent arrivals: Dídac, Stefano, Estefania and Iker to whom I wish an easy ride through the doctoral journey. Likewise, I want to mention those that have passed by the physical-chemistry unity anyhow, during the time I was here: Javi Navarro, Andrea, Mireia, Egil, Francesca, Lur, Jaime and Bart who have contributed to this journey with also lots of conversations, coffees, laughs and friendship.

I want to express my sincere thanks to all my TFG students and, in particular to Yeray, whose give me the opportunity to show them how nice research can be and for all the dedication and interest in their projects.

Last but not least, I would like to thank my parents for all the love, dedication, effort and for always showing me how proud they are of me. For similar reasons, I want to thank all my childhood friends who they are my most valuable treasure. I can't imagine my life without all of you.

Curriculum Vitae

Education

2016 - 2019 Ph.D., Theoretical Chemistry (UAB)

2014 - 2015 Msc., Industrial Chemistry and Introduction to Chemical Research (UAB)

2009 - 2014 Bsc., Chemistry Degree (Mention in Materials Science) (UAB)

Recent Publications

(273)   Heras-Domingo, J.; Sodupe, M.; Solans-Monfort, X. *The Journal of Physical Chemistry C* **2018**, *123*, 7786–7798.

(274)   Gonzalez, D.; Heras-Domingo, J.; Pantaleone, S.; Rimola, A.; Rodriguez-Santiago, L.; Solans-Monfort, X.; Sodupe, M. *ACS Omega* **2019**, *4*, 2989–2999.

Other Collaborations

(275)   Luis-Barrera, J.; Monserrat, R. C.; Heras-Domingo, J.; Perez-Carvajal, J.; Imaz, I.; Solans-Monfort, X.; Maspoch, D.; Aleman, J.; Balleste, R. M., et al. *Catalysis Science & Technology* **2019**.

Workshops and Training

- *Vienna Ab Initio Simulation Package* (VASP) - ICAMM Workshop 2016 (Rennes, France)
- Introduction to Statistical Computing in Python - (Servei de Genomica I Bioinformatica)
- Machine Learning for Material Science Workshop - (Aalto University, Helsinki)

Teaching

- General Chemistry Subject (Nanotechnology and Biotechnology Degrees)
- Anàlisi i Determinació de Propietats Lab. (Chemistry Degree)
- Thermochemistry Lab (Chemistry and Biochemistry Degrees)
- Spectrocopy Theoretical Lab (Chemistry Degree)

Outreach Activities

- Química Interactiva - (Theoretical Sessions)